Title

Spatially Confined Reactions: Stochastic Effects in Signaling Reactions at the Membrane

Author

Lee, Albert Alexander

Publication Date

2022

Peer reviewed|Thesis/dissertation

Spatially Confined Reactions:
Stochastic Effects in Signaling Reactions at the Membrane

By

Albert Alexander Lee

A dissertation submitted in partial satisfaction of the

requirements for the degree of

Doctor of Philosophy

in

Molecular and Cell Biology

in the

Graduate Division

of the

University of California, Berkeley

Committee in charge:

Professor Jay T. Groves, Co-Chair

Professor John Kuriyan, Co-Chair

Professor David G. Drubin

Professor Daniel A. Fletcher

Summer 2022

Spatially Confined Reactions:

Stochastic Effects in Signaling Reactions at the Membrane

by

Albert Alexander Lee

Abstract

Spatially Confined Reactions:

Stochastic Effects in Signaling Reactions at the Membrane

by

Albert Alexander Lee

Doctor of Philosophy in Molecular and Cell Biology

University of California, Berkeley

Professor Jay T. Groves, Co-Chair

Professor John Kuriyan, Co-Chair

Signaling reactions often originate at the membrane, where competing membrane reactions decide if and how the signal will be passed on to downstream signaling cascades. In some cases, membrane reactions can even lead to polarization of signaling molecules that convey spatial information to downstream pathways. Due to the microscopic size of cellular structures, reactions at the membrane are confined and limited to low molecular copy numbers. Signaling decisions are therefore subject to strong stochastic effects. Understanding how membrane reactions can be influenced by stochastic effects is an imperative step toward deciphering the molecular logic of cellular signaling. However, the space of possibilities remains sparsely mapped. In this dissertation, I aim to expand our understanding of this topic by studying two-dimensional confinement effects on phosphatidylinositol signaling and small GTPase signaling reactions, both of which are ubiquitous membrane signaling mediators. Reducing the size of the membrane can lead to two distinct types of stochastic effects: size-dependent reaction speed and stochastic bistability. The underlying physical mechanism is intrinsically stochastic and cannot be predicted by classical deterministic kinetics. The biochemical requirements and potential cellular regulation of these stochastic effects are further discussed. In membranes with asymmetric shapes, the difference in local stochastic effects that the reaction experiences could emerge as stochastic polarization. This stochastic polarization has no analog in continuum reaction-diffusion systems and exhibits a striking ability to polarize in a consistent direction when constrained to cellular shapes. The requirements of size-dependent reaction speed, stochastic bistability, and stochastic polarization are very basic, and largely met in cellular environments, such that many membrane signaling reactions may be subject to these effects. Overall, the discussions here provide a basis to understand how the size and shape of the membrane can be a regulating factor of biochemical reactions and further influence living phenomena.

Table of Contents

Acknowledgements

The journey of getting a PhD is a long and hard process. At the same time, graduate school is the time to do fun and exciting science, not worry about anything else. I am exceptionally fortunate to have the supports I have from my mentors, colleagues, friends, and family. It is because of these supports I have been able to make my PhD journey possible and enjoyable.

First, I would like to thank my advisor, Prof. Jay Groves. I am thankful for him to agree to be my advisor at the time I left my previous lab and was feeling lost. I am especially grateful for the academic freedom he gave me that allowed me to truly enjoy and be excited about science. He constantly challenges me intellectually and does not hesitate to call me out when I am wrong. Yet at the same time he always sees positives things and encourages me when I am down. I would not have grown as much as a scientist without his mentorship.

I am fortuitous to have the opportunity to be surrounded by incredibly talented scientists. Dr. Scott Hansen mentored me in my earliest days as a graduate student and has set me well for success in graduate school. He is always open to discussions and truly cares about my development as a scientist. Dr. Scott Hansen also initiated the stochastic geometry sensing research in the Groves lab and my projects would not exist without him. Dr. Hyuneil Kim and I have been working together closely since I joined the lab. Dr. Hyuneil Kim has taught me a lot about how to work as a team. He always has a positive attitude toward things and that is what kept our project going. Dr. William Huang is truly brilliant and always comes up with great ideas, and I owe all my training in stochastic kinetics and simulation to him. Dr. Steven Alvarez taught me to do Ras related experiments and is always willing to help, share ideas and share reagents. I want to thank Joey DeGrandchamp and Nugent Lew for their generosity in reagent sharing. Also extra thanks to Joey DeGrandchamp for help proofreading my dissertation. I want to thank He Ren for heling me with my experiments, and her can-do attitude and all-out effort really inspired me. While I never had the pleasure to work directly with Dr. Jean Chung, Dr. Young Kwang lee, Dr. Shalini Low-Nam, Dr. Chun-Wei Lin, Dr. Darren McAffee, Dr. Laura Nocka, Dr. Zhongwen Chen, Dr. Simou Sun, Dr. Mark O'Dair, I am grateful for all the great discussions I had with them. I would also like to thank all past and present Groves lab members for making the Groves lab an enjoyable place to do science.

I am grateful to have the opportunity to interact and collaborate with Prof. John Kuriyan, Prof. Orion Weiner, Prof. Dimitrios Stamou, and Dr. Yasushi Kondo. I want to thank them for the insightful and fruitful conversations. I would also like to thank my thesis committee members, Prof. John Kuriyan, Prof. David Drubin, and Prof. Daniel Fletcher for their feedback on my research and guidance in my career development.

I am blessed to have a very supportive family. From a young age, my parents have always encouraged me to just follow my heart. My family has allowed me to pursue my passion without worrying, and they

have made tremendous sacrifices to make that possible. It is because of them so I can be where I am today.

Finally, I would like to thank my wife, Tammy Chen, for always bringing me joy, encouraging me when I am down, and enriching my life. Tolerating me to spend a lot of time on research, sometimes even all weekend or all night. Thank you.

Chapter 1
INTRODUCTION

Lipid bilayer membranes are the barrier between living and non-living systems(*1*). In addition, eukaryotic membrane structures also segregate complex biochemical reactions with diverse roles into specialized compartments(*1*). As such, the membrane is the communication interface and many signaling reactions are thus initiated at the membrane(*1*, *2*). Here, signals can undergo initial processing and be further distinguished to determine if the signal will continue on to elicit downstream responses. To understand how cells make logical decisions corresponding to received stimuli, it is imperative to study how signals are processed at the membrane interface. Fundamentally, the signal processing logic at the membrane is encoded by a network of biochemical reactions, often with competing activity. Nucleotide exchange and nucleotide hydrolysis in GTPase signaling(*3*), phosphorylation and dephosphorylation of tyrosines in EGFR signaling(*4*), and interconversion of phosphatidylinositol lipids(*5*) are all examples. According to each stimulus, the properties of these reactions can be fine-tuned to yield signaling molecules for appropriate decisions. In some cases, the reactions at the membrane can even establish patterns of signaling molecules that locate the signaling activity spatially.

Although traditionally considered a passive reaction platform, the physical features of the membrane play a critical role in regulating signaling. For example, membrane curvature, membrane thickness and membrane tension can all alter signaling activity at the membrane. A more basic physical parameter of the membrane is its surface area. The stochasticity of the reaction is inevitably coupled with membrane size. It used to be thought that stochastic effects provided only fluctuations and modest refinements to the behaviors predicted by deterministic kinetics. Recently however, it was reported that the surface area of the membrane can completely change the reaction outcome in a model lipid kinase-phosphatase competition reaction(*6*). In cells, membrane reactions span a range of spatial dimensions, from the plasma membrane with a scale in microns to vesicles on the nanometer scale(*1*). Moreover, the cytoskeleton, membrane proteins, and membrane topographical features can all create dynamic physical barriers that can locally confine reactions on cellular membranes(*7*–*9*). To understand how cellular signaling is regulated in different subcellular compartments, it is necessary to study the effect of membrane size on the signaling reactions at the membrane.

In this dissertation, I focus on discussing how stochastic effects originating from spatially confined membrane reactions can influence the signaling outcome. All conclusions are based on empirical results from *in vitro* reconstitution experiments. At the same time, an emphasis is made on rigorously validating the underlying physical mechanism using stochastic modeling. In Chapter 2, I will begin by describing a molecular mechanism, based on the discrete nature of low molecular copy reactions, that causes the average enzymatic catalytic rate at the membrane to exhibit reaction size dependency. The mechanism is universal across many types of enzymes, including kinases, phosphatases, and guanine nucleotide exchange factors.

Subsequently, I will discuss the potential signaling consequence of such an effect, where the final signaling product in competitive enzymatic reaction cycles can depend on the size of the reaction system. In Chapter 3, I will describe another type of molecular mechanism that allows a competitive enzymatic reaction to exhibit switch-like responses only when the reaction is confined to a microscopic scale. This is commonly described as stochastic bistability in signaling(*10*, *11*). However, to this date stochastic bistability in signaling remains primarily a theoretical concept that has little experimental evidence to support it(*12*). Here in, I show clear experimental results demonstrating stochastic bistability in Ras signaling reactions at the membrane. A stochastic model was used to further reveal the physical mechanism behind the stochastic bistability. At the end of the chapter, I detail examples of how this stochastic switch-like response in Ras signaling can be regulated by the cell. Finally, Chapter 4 describes how the stochastic effects identified in Chapter 2 and Chapter 3 can lead to polarization in membrane reactions. The mechanisms are rooted in stochasticity and are different from the well-known Turing pattern(*13*). A distinct feature of these stochastic polarization activities is that the direction of the polarization can be determined by the shape of the membrane. Together, this dissertation aims to provide a physical understanding of membrane signaling logic in a stochastic environment and firmly establish membrane size as a non-negligible factor in cellular signaling.

Chapter 2

STOCHASTICITY AND POSITIVE FEEDBACK ENABLE ENZYME KINETICS AT THE MEMBRANE TO SENSE REACTION SIZE

(This Chapter is adapted with permission from A. A. Lee, W. Y. C. Huang, S. D. Hansen, N. H. Kim, S. Alvarez, J. T. Groves, Stochasticity and positive feedback enable enzyme kinetics at the membrane to sense reaction size. Proc. Natl. Acad. Sci. 118, e2103626118 (2021).)

Here we present detailed kinetic analyses of a panel of soluble lipid kinases and phosphatases, as well as Ras activating proteins, acting on their respective membrane surface substrates. The results reveal that the mean catalytic rate of such interfacial enzymes can exhibit a strong dependence on the size of the reaction system—in this case membrane area. Experimental measurements and kinetic modeling reveal how stochastic effects stemming from low molecular copy numbers of the enzymes alter reaction kinetics based on mechanistic characteristics of the enzyme, such as positive feedback. For the competitive enzymatic cycles studied here, the final product—consisting of a specific lipid composition or Ras activity state—depends on the size of the reaction system. Furthermore, we demonstrate how these reaction size dependencies can be controlled by engineering feedback mechanisms into the enzymes.

2.1 Introduction

Enzyme kinetic reactions are commonly described in terms of deterministic rate equations. Within this type of mathematical analysis, reactant and product concentrations are treated as continuous variables and the state of a system at any point in time is a deterministic function of the starting conditions. Even complex behaviors including bistability(*14*), sensitive dependence on initial conditions (e.g. chaos)(*15*), and spatiotemporal pattern formation (e.g. Turing instabilities)(*16*) can all be described with deterministic rate equations. It is computationally efficient to simulate deterministic chemical kinetics and this method is widely used in biological sciences. For example, more than 100 papers have been published in the last five years analyzing Ras activation using deterministic chemical rate equations, with many of these making predictions about disease mechanisms and therapeutic approaches(*17*, *18*). These mathematical methods, however, smooth over the fact that molecules and molecular reactions are intrinsically discrete. Moreover, the small size of cellular structures often limits physiological biochemical reactions to low molecular copy numbers, where the effects of discreteness and stochasticity become prominent.

How spatial confinement and low molecular copy numbers within cells and organelles might affect biochemical reactions has attracted significant interest over the years(*19–23*). However, the space of possibilities remains sparsely mapped and surprising results continue to emerge. For example, stochastic fluctuations can increase sensitivity in cellular signaling reactions(*24*) and they play an essential role in the bacterial chemotaxis molecular logic circuit(*25*). They can also induce (stochastic) bistability in systems that lack this property according to continuous kinetic rate equations(*26*). Recent experimental observations of a system of competing lipid kinases and phosphatases, driving interconversion between PI(4)P and PI(4,5)P_2 in a lipid membrane, have revealed other types of macroscopic divergence from continuum kinetic predictions(*6*). Specifically, this system was observed to deterministically reach a PI(4)P dominated state in large reaction systems. Under spatial confinement, however, the same system could exhibit stochastic bistability or even deterministically reach a PI(4,5)P_2 dominated state, depending only on the size of the reaction environment. Stochastic effects led to a deterministic alteration in the average behavior, not just an increase in variation. Although stochastic kinetic modeling was able to reproduce this basic behavior, the underlying physical mechanism remains obscure. This stochastic geometry sensing mechanism also produces more elaborate pattern formations, including polarization, under different types of spatial confinement that exhibit marked similarity with living biological systems.

A distinctive feature of the competing lipid kinase-phosphatase system is that the soluble enzymes act on substrates restricted to the membrane surface. This basic reaction configuration is shared by broad classes of signal transduction enzymes in biology, including numerous protein or lipid kinases and phosphatases as well as GTPase-activating proteins (GAPs) and Guanine nucleotide exchange factors (GEFs)(*3*, *27–29*). For these systems, the enzyme must first contact the membrane, then find the substrate and catalyze a two-dimensional reaction at the membrane interface. This additional step offers many mechanisms for regulatory control of signaling reactions(*30–32*). For example, positive feedback can be easily installed on enzymes by incorporating a product binding site, which localizes the enzyme on the membrane, without the need for structural allosteric mechanisms. Other physical properties such as curvature and membrane tension can alter the enzyme activity by changing the partitioning of enzymes from the solution to the reaction surface(*33*, *34*). Additionally, the cellular cytoskeleton and membrane topographical features can create dynamic physical barriers and confinement zones on cellular membranes(*7–9*). While these membrane structures are all exposed to the same cytosolic solution, the differing sizes of their effective reaction environments offer another regulatory mechanism if signaling reactions exhibit scale sensitivity.

Here we examine a panel of soluble lipid kinases and phosphatases, as well as Ras activating proteins, acting on their respective membrane surface substrates. Using micropatterned supported lipid membranes, liposomes, and membrane-coated microbeads, we perform detailed kinetic analyses of these enzymes as a function of reaction system size. Results reveal that the mean catalytic rate of such interfacial enzymes can exhibit a strong dependence on the physical area of the membrane, which sets the copy number of enzymes within an interactive system. We find that the size-dependence of the reaction rate is caused by positive feedback in the enzymatic mechanism. Furthermore, we demonstrate that size-dependency can be deleted from or engineered into enzymes by deleting or adding specific lipid-binding domains. A simple analytical model, as well as more detailed stochastic kinetic simulations, reveal how size-dependency of the reaction rate emerges from a coupling between positive feedback, nonequilibrium aspects of the enzymatic reaction cycle, and intrinsic stochasticity.

These basic features that lead to the size-dependency of the enzymatic reaction rate are extremely common among native biological signaling enzymes. We report here that Phosphatase and Tensin Homolog (PTEN), Phosphatidylinositol-4-Phosphate 5-Kinase (PIP5K), as well as the Ras activator Son of Sevenless (SOS)

all exhibit size-dependent reaction rates. Furthermore, when coupled in a competitive enzymatic cycle, subtle differences in size sensitivity of the competing reactions can completely change the final output in a system size-dependent manner. While these experiments are done in reconstituted systems, we suggest that the underlying physical phenomenon of size-dependent enzymatic reaction rate is unavoidable in living cells.

2.2 PTEN exhibits reaction system size-dependent catalytic activity

Phosphatase and Tensin Homolog (PTEN) is a well-studied and important lipid-modifying enzyme(*35*, *36*) that catalyzes the dephosphorylation of $PI(3,4,5)P_3$ into $PI(4,5)P_2$ and inorganic phosphate. PTEN is a soluble enzyme, which must encounter the membrane for its catalytic reaction (Fig. 2-1A)(*37*). PTEN contains an N-terminal $PI(4,5)P_2$-binding domain (PBD), which creates a positive feedback loop in which PTEN catalyzed formation of $PI(4,5)P_2$ on the membrane drives the recruitment of more PTEN to the membrane(*36*). Membrane localization can also lead to processivity(*38*, *39*), in which multiple catalytic events occur during a single membrane binding dwell cycle.

We initially investigate PTEN catalytic activity on liposomes of different sizes. Liposomes consisting primarily of DOPC (1,2-dioleoyl-sn-glycero-3-phosphocholine) with 2% molar fraction of $PI(3,4,5)P_3$ were prepared by extrusion through polymer filter membranes of either 30 nm or 1000 nm pore size. While extrusion yields broadly dispersed liposome sizes, extrusion through 30 nm pores produces distinctly smaller liposomes than obtained from the 1000 nm pore size(*40*). For the liposome assays, PTEN catalytic activity was monitored by detecting released inorganic phosphates from the reaction using a phosphate binding protein labeled with the environmentally sensitive fluorescence probe MDCC (N-[2-(1-maleimidyl)ethyl]-7-(diethylamino)coumarin-3-carboxamide), which increases fluorescence yield upon binding to inorganic phosphate(*41*). Kinetic traces of PTEN activity reveal that the reaction is slower in 30 nm extruded liposomes compared to 1000 nm extruded liposomes (Fig. S2-1). By fixing both the PTEN solution concentration and the $PI(3,4,5)P_3$ surface concentration in the membrane, but varying the total amount of liposomes, the reaction velocity was mapped to overall substrate concentration (Fig. 2-1B). The apparent enzyme catalytic efficiency can be obtained by fitting the resultant reaction velocity traces to a Michealis-Menten kinetic analysis (see Materials and Methods). The catalytic efficiency (k_{cat}/K_M) of PTEN is increased by 50% when reacting on 1000 nm pore extruded liposomes compared with liposomes obtained from 30 nm pore extrusion. The same size-dependent effect was also evident on membrane-coated microbeads(*42*), where $PI(4,5)P_2$ production was monitored by imaging the binding of the fluorescently labeled PH domain of phospholipase C δ (PLCδ) to $PI(4,5)P_2$ using confocal microscopy, normalized by the fluorescence from a lipid-linked Texas Red fluorophore (Texas Red 1,2-Dihexadecanoyl-sn-Glycero-3-Phosphoethanolamine) present in the membrane at a fixed density (0.5%) (Fig. 2-1C). Under these experimental conditions (both here on microbeads and in the supported membrane corral arrays described below), generally less than 0.1% of $PI(4,5)P_2$ lipids are bound by the fluorescent probe at any given time(*6*). After PTEN is added, $PI(4,5)P_2$ is produced at faster rates in membrane-coated microbeads with a larger diameter (Fig. 2-1D and 2-1E). The time to 95% completeness of reaction is 80% longer in 2.34 μm beads compared to 6.89 μm beads.

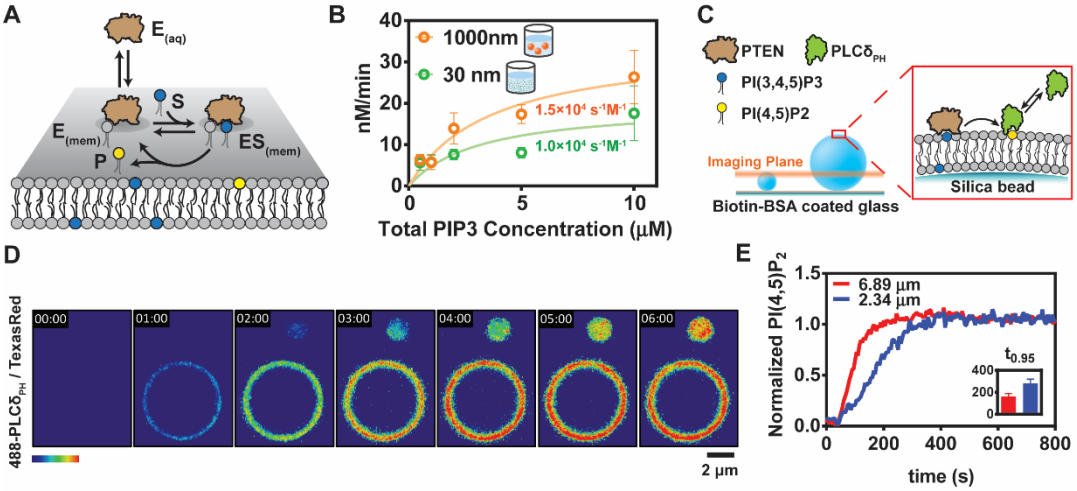

Figure 2-1. *in vitro* PTEN Phosphatase Reaction in Different Sizes of Membrane. (A) Kinetic scheme of a lipid-modifying enzyme performing reaction on the membrane surface. The enzyme can dynamically bind and unbind to the membrane surface. Once bound to the membrane, the enzyme can access the substrate at the membrane and catalyze product formation following the Michaelis–Menten kinetics. (B) Turnover of $PI(3,4,5)P_3$ to $PI(4,5)P_2$ by 10 nM PTEN was measured in various total solution concentrations of $PI(3,4,5)P_3$ at a fixed 2% surface concentrations of $PI(3,4,5)P_3$ on either 30 nm or 1000 nm diameter liposomes. Fitting the data to the Michaelis–Menten equation reveals k_{cat}/K_M values shown on the graph. (C) Schematic of the membrane-coated microbeads experiment setup. Microbeads coated with supported lipid bilayer with 96.5% of DOPC, 2% $PI(3,4,5)P_3$, 1% Biotin-PE, and 0.5% TR-DHPE were tethered to glass surface functionalized with Biotin-BSA using neutravidin. PTEN catalyzes the conversion of $PI(3,4,5)P_3$ to $PI(4,5)P_2$. Production of $PI(4,5)P_2$ is monitored with Alexa488-PLCδ_{PH}. (D) Time sequence of images tracking 200 nM PTEN reaction on 6.89 μm beads and 2.34 μm beads. (E) Average kinetic traces of normalized $PI(3,4,5)P_3$ to $PI(4,5)P_2$ conversion by 200 nM PTEN plotted against time (n=6). The inset shows time to 95% completeness of the reactions in 6.89 μm beads and 2.34 μm beads.

Changing the diameter of liposomes or microbeads not only changes membrane surface area, but also curvature. Since membrane curvature can significantly change the reaction rate of some enzymes(21), we implemented the PTEN activity assays in a planar micropatterned supported lipid bilayer (SLB) format (Fig. 2-2A)(*43*). Grids of chromium metal lines, prefabricated onto glass coverslips, create barriers to supported membrane formation and effectively confine the membrane into two-dimensional corrals with micrometer-scale dimensions(*39*, *44*). Lipids and membrane-associated proteins diffuse freely within each confined corral but cannot cross the barriers. However, all corrals are in contact with the same bulk solution and the low vertical height of the metal lines (~9 nm in these experiments) has essentially no effect on the diffusion and flow of molecules in the bulk solution phase. The SLB experimental system provides superior sub-second time resolution and control of reaction size homogeneity compared to the liposome and bead assays(*6*). Moreover, the system is completely planar, leaving the surface area and shape to be the only geometrical variables.

The catalytic activity of PTEN was observed in the unrestricted free lipid bilayer, with a scale on the order of millimeters, and in 5 μm × 5 μm corralled membrane arrays. Confinement grids were patterned side-by-side with the unrestricted regions, enabling simultaneous monitoring in both regions under identical reaction conditions (Fig. 2-2B). PTEN and the lipid sensor were introduced into the system from the solution flowed into the flow cell. All regions of the supported membrane are in contact with the exact same solution above. Under these conditions, restricting the membrane surface reaction size from the free lipid bilayer to 5 μm × 5 μm corrals significantly slows down the mean reaction rate. This is evident in the fluorescence intensity plots — mapping $PI(4,5)P_2$ membrane concentration—illustrated in Fig. 2-2B. At 4

min into the reaction, the bulk membrane area is nearly completely converted to $PI(4,5)P_2$ while each of the corralled membrane regions lags significantly. This kinetic experiment is quantified in Fig. 2-2C where the mean normalized $PI(4,5)P_2$ density is plotted vs. time for corralled and free membrane regions (replicates shown in Fig. S2-2A). The maximum difference in normalized reaction progress (Δx) across the reaction period can reach more than 0.2. Since all membrane regions in this experiment are entirely flat, membrane curvature is ruled out as a cause of the differential enzyme efficiency. Membrane surface area alone is sufficient to cause the difference in reaction speed. As will be discussed in further detail later, this size-dependent enzymatic reaction speed is fundamentally the result of stochastic effects in enzyme copy number on the membrane surface. However, it is important to note that observed reaction rates do not vary substantially from corral to corral in the 5 μm x 5 μm array. Each corral confined reaction is consistently slower than the unrestricted membrane (Fig. S2-2A).

Size-dependent reaction speed is a property of the enzyme and is not universal. Similar experiments on another lipid phosphatase, phosphatidylinositol 5'-phosphatase domain of Lowe Oculocerebrorenal Syndrome Protein ($OCRL_{PD}$), do not exhibit reaction size-dependent effects. Kinetic traces of $OCRL_{PD}$ catalyzed reactions on the bulk membrane and in 5 μm x 5 μm corral arrays are essentially identical, exhibiting Δx values below 0.05 throughout the reaction (Fig. 2-2D, 2-2E and S2-2B).

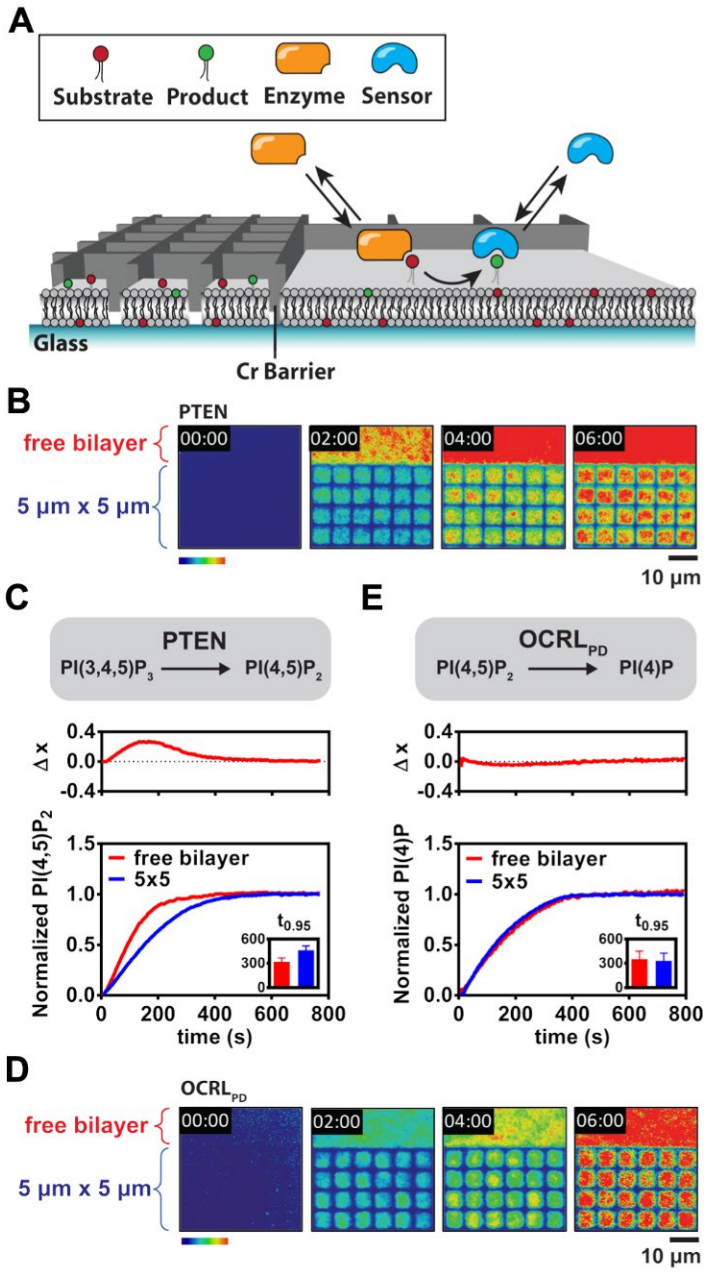

Figure 2-2. Kinetics of Enzymes on Confined Planar Lipid Bilayer. (A) Scheme of the supported lipid bilayer experimental setup. Nanofabricated chromium barriers partition a supported bilayer into micrometer-scale corrals, each containing identical composition. When the enzyme converts substrates to products at the membrane, the products can be monitored with a fluorescently labeled lipid binding domain that binds to the product. **(B)** Time sequence of images of 100 nM PTEN reaction on membrane containing 2% $PI(3,4,5)P_3$ monitored by 20nM Alexa488-$PLC\delta_{PH}$. Reactions in 5μm x 5μm membrane corrals were imaged alongside with reaction in free bilayer in the same experiment. **(C)** Dephosphorylation reaction of $PI(3,4,5)P_3$ to $PI(4,5)P_2$ by 100 nM PTEN in 5μm × 5μm of membrane corrals and free bilayer plotted together. Top graph: The difference between the reaction trajectory in the free bilayer and 5μm × 5μm membrane corrals, Δx, at each time point. The inset shows time to 95% completeness of the reactions in free bilayer and 5μm × 5μm membrane corrals. **(D)** Time sequence of images of 50 nM $OCRL_{PD}$ reaction in membrane containing 4% $PI(4,5)P_2$ monitored by 20nM Cy3-DrrA. **(E)** Dephosphorylation reaction of $PI(4,5)P_2$ to PI(4)P by 50 nM $OCRL_{PD}$ in 5μm × 5μm membrane corrals and free bilayer.

2.3 Positive feedback enables size-dependent catalytic activity

We characterize the mechanistic origin of PTEN reaction size sensitivity by first removing its positive feedback. In the PTEN domain structure, the PBD domain is followed by phosphatase, C2, and C-terminal domains(*35*). We truncate the PBD domain to construct the $PTEN_{\Delta PBD}$ variant, which lacks the $PI(4,5)P_2$ membrane binding-mediated positive feedback loop (Fig. 2-3A). The activity of $PTEN_{\Delta PBD}$ is significantly compromised and no activity was observable on 2% $PI(3,4,5)P_3$ lipid membranes (Fig. S2-3). Increasing the overall membrane negative charge by adding 5% PS, in addition to the 2% $PI(3,4,5)P_3$, facilitated the reaction and revealed that $PTEN_{\Delta PBD}$ does not exhibit size dependency (Fig. 2-3A and S2-2C). Control experiments including PS with full-length PTEN exhibit the same size-dependency observed on 2% $PI(3,4,5)P_3$ membranes, confirming that PS is not responsible for inhibiting reaction size sensitivity (Fig. S2-4). The PTEN PBD domain is essential for its reaction size-dependent catalytic activity.

The apparent primary function of the PTEN PBD domain is to mediate membrane recruitment by binding $PI(4,5)P_2$, providing a positive feedback loop. However, it remains unclear if the inability of $PTEN_{\Delta PBD}$ to exhibit size-dependent activity is solely caused by loss of positive feedback or other unknown functions of the PBD. To investigate this, we constructed a reaction system with native PTEN, but in which the $PI(4,5)P_2$ positive feedback loop is eliminated. PTEN phosphatase activity is promiscuous and it readily catalyzes 3'-dephosphorylation of not only $PI(3,4,5)P_3$, but also other phosphatidylinositols containing 3'-phosphate, such as $PI(3,4)P_2$ to PI(4)P(*45*). PBD binding, however, is quite specific and only $PI(4,5)P_2$ strongly activates PTEN while other phosphatidylinositols, including $PI(3,4)P_2$, either do not activate or only weekly activate PTEN(*45*, *46*). Therefore, without any $PI(4,5)P_2$-mediated activation, PTEN catalyzed 3'-dephosphorylation of $PI(3,4)P_2$ to PI(4)P cannot exhibit strong positive feedback. As anticipated, kinetic analysis of PTEN catalyzed $PI(3,4)P_2$ to PI(4)P reactions in the bulk membrane and in 5 μm x 5 μm corral arrays also do not exhibit any detectable size-dependent catalytic activity (Fig. 2-3B and S2-2D).

By engineering a PI(4)P binding domain into PTEN, we construct a new variant with positive feedback in the $PI(3,4)P_2$ to PI(4)P reaction. DrrA is a GEF of Rab1 that contains a PI4P binding domain (DrrA 544–647)(*47*). We refer to this fragment as DrrA hereafter. Kinetic traces from the PTEN-DrrA reaction on 2% $PI(3,4)P_2$ membrane follow a strongly sigmoidal shape, indicating the reaction has positive feedback. Starkly contrasting PTEN, PTEN-DrrA shows strong reaction size-dependent catalytic activity in the 3'-dephosphorylation of $PI(3,4)P_2$ (Fig. 2-3C and S2-2E). Using a similar strategy, the $OCRL_{PD}$ catalyzed $PI(4,5)P_2$ to PI(4)P dephosphorylation reaction, which intrinsically lacks feedback, can be augmented with positive feedback by fusing $OCRL_{PD}$ with a DrrA domain. Kinetic traces of DrrA-$OCRL_{PD}$ shows both positive feedback and size-dependent reaction speed (Fig. 2-3D and S2-2F). Overall, these data illuminate a clear and causal relationship between membrane-binding mediated positive feedback and reaction size-dependency of catalytic activity.

Across the wide variety of chemical reactions catalyzed by interfacial enzymes, positive feedback through product binding is a common feature among many of them. In addition to lipid phosphatases such as PTEN, lipid kinases such as PIP5K and GEFs such as SOS have all been reported to natively possess such a mechanism(*6*, *48*). We therefore posited that these enzymes all could exhibit reaction size-dependency in their catalytic activity and tested this with the kinase domain of PIP5K ($PIP5K_{KD}$) and the catalytic N-terminal fragment of SOS (SOS_{HDPC}). $PIP5K_{KD}$ catalyzes PI(4)P to $PI(4,5)P_2$ reaction at the expense of an ATP, and separately binds $PI(4,5)P_2$. SOS_{HDPC} catalyzes nucleotide exchange, converting Ras-GDP to Ras-GTP, and can bind Ras-GTP with a stronger affinity at an allosteric site(36). Both PIP5K and SOS showed

size-dependent catalytic activity (Fig. 2-3E, 2-3F, S2-2G and S2-2H). Notably, while the catalytic domain of SOS, SOS_{cat}, contains the allosteric Ras-GTP (product) binding site and showed clear positive feedback in its catalytic activity, it is not size-sensitive under the conditions in our experiment (Fig. S2-5). As will be clarified in the following sections, this can be attributed to the fact that SOS_{cat} is distinctively less processive than either SOS_{HDPC} or native full-length SOS(*44*, *49*, *50*). While strong processivity is neither a requirement nor sufficient for reaction size sensitivity, it is an amplifier of these effects.

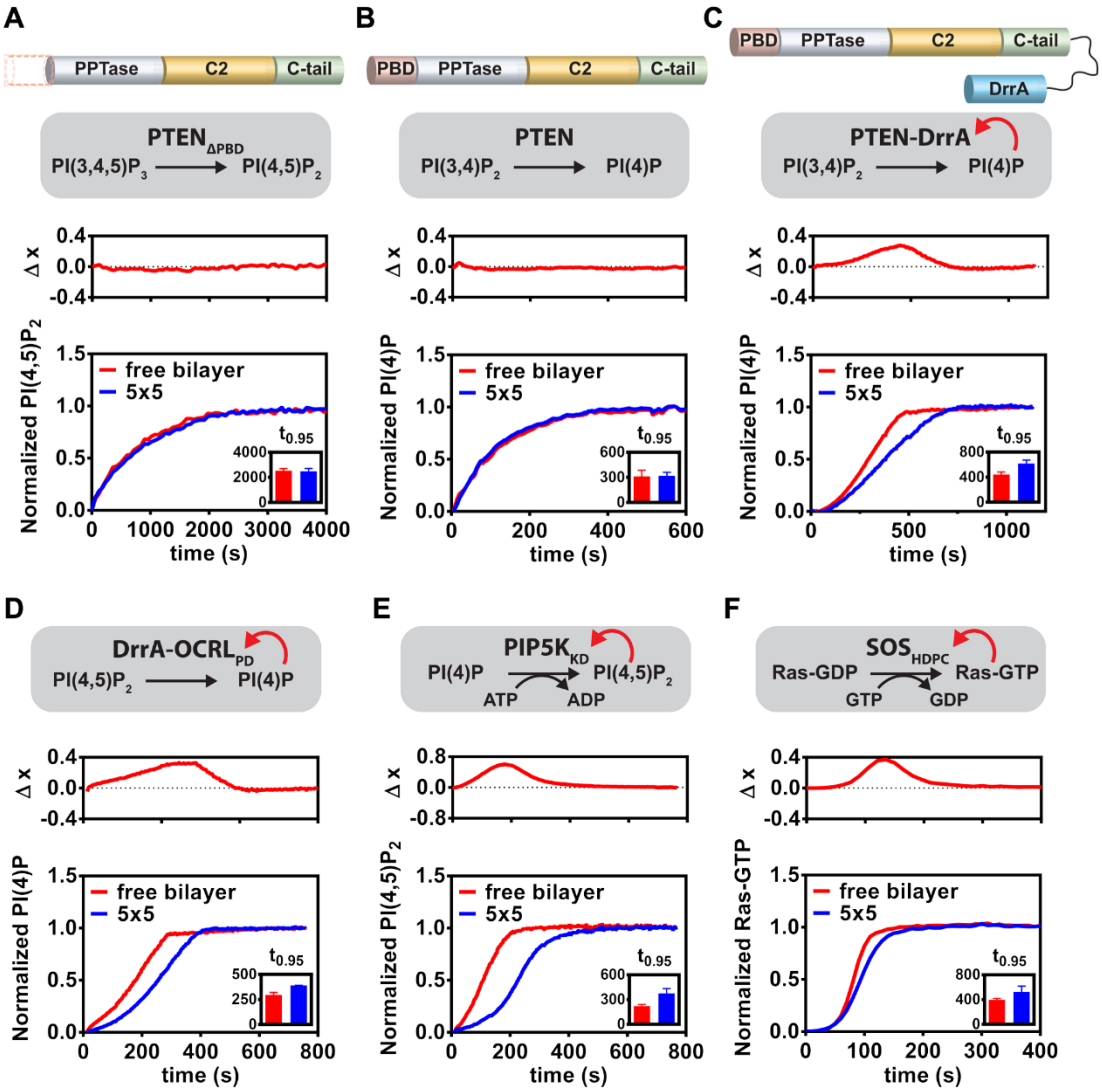

Figure 2-3. Biochemically engineering size-dependent reaction speed. (A) Dephosphorylation reaction of $PI(3,4,5)P_3$ to $PI(4,5)P_2$ by 23 μM $PTEN_{\Delta PBD}$ in 5μm x 5μm membrane corrals and free bilayer. PBD: PIP2-binding domain; PPTase: Phosphatase domain. C-tail: C-terminal tail. **(B)** Dephosphorylation reaction of $PI(3,4)P_2$ to PI(4)P by 3 μM PTEN in 5μm x 5μm membrane corrals and free bilayer. **(C)** Dephosphorylation reaction of $PI(3,4)P_2$ to PI(4)P by 170 nM PTEN-DrrA in 5μm × 5μm membrane corrals and free bilayer. **(D)** Dephosphorylation reaction of $PI(4,5)P_2$ to PI(4)P by 100 pM $DrrA\text{-}OCRL_{PD}$ in 5μm × 5μm membrane corrals and free bilayer. **(E)** Phosphorylation reaction of PI(4)P to $PI(4,5)P_2$ by 2 nM $PIP5K_{KD}$ in 5μm × 5μm membrane corrals and free bilayer plotted together. **(F)** Nucleotide exchange reaction of Ras-GDP to Ras-GTP catalyzed by 20 nM SOS_{HDPC} in 5μm × 5μm membrane corrals and free bilayer plotted together. The reaction is monitored by binding of a fluorescently labeled Ras-binding domain.

2.4 Competitive enzymatic cycles amplify effects of reaction size dependency

Native forms of all of the enzymes studied here operate in competitive reaction cycles under physiological conditions. Kinases are opposed by phosphatases, Ras GEFs are opposed by GAPs, and this is a common theme across many biological signaling systems. In such competitive reactions, small differences in reaction rate can determine what the final outcome is, and this can amplify the consequences of even small reaction size-dependencies among the competing enzymes. As an example of this, we here study the competitive reaction between PIP5K and OCRL. This system drives interconversion between PI(4)P and $PI(4,5)P_2$, and is one of several similar competitive lipid kinase-phosphatase systems we have recently found to exhibit complex reaction size sensitivity and pattern forming tendencies(*6*).

A time sequence of images following a reaction trajectory for the PIP5K:OCRL system on SLB corral arrays of various sizes is illustrated in Fig. 2-4A. For these experiments, the supported membrane has an initial composition of 2% PI(4)P and 2% $PI(4,5)P_2$ (in a DOPC background) and lipid sensors for PI(4)P (DrrA), in blue, and $PI(4,5)P_2$ (PLCδ) in yellow track the composition over time, by TIRF imaging. The reaction is initiated by injecting a solution of both enzymes, ATP, and lipid sensors into the imaging flow cell. As can be seen in the image sequence, the larger area of the membrane is smoothly driven to a $PI(4,5)P_2$-dominated state, indicating that the average balance between kinase and phosphatase in this particular experiment favors the kinase. However, under the identical enzyme mixture in the solution, the system exhibits bistability in 5 μm x 5 μm corral arrays and is uniformly driven to a PI(4)P-dominated state in 2 μm x 2 μm corral arrays. In this case, the net reaction outcome—a PI(4)P- or $PI(4,5)P_2$-dominated state—depends on the size of the membrane reaction system. This effect can drive reaction outcome with near certainty; note that there are no visible 2 μm x 2 μm corrals ending in the $PI(4,5)P_2$-dominated state even though this is the kinetically favored state in the bulk average.

The complete inversion in the outcome of the PIP5K:OCRL system, as a function of reaction size, is achieved based on differences in the size-dependency of the individual enzymatic reactions. In this case, PIP5K has positive feedback and exhibits size-dependent reaction rates whereas OCRL does not. The effect of reaction size on the balance between these two reactions is illustrated schematically in Fig. 2-4B. For a given enzyme concentration in solution, the reaction rate for PIP5K increases with reaction size while that of OCRL is constant. As such, it is possible to achieve a situation in which positive feedback in PIP5K provides it with a kinetic advantage in large systems, while OCRL can still dominate in sufficiently small systems. We note that in our previous study of a similar system with PIP5K, many of the experiments utilized variants of OCRL with engineered positive feedback(*6*). In those experiments, both enzymes exhibit positive feedback and size sensitivity. The particular balance between size sensitivity of the competing enzymes led to exactly the opposite size preference seen here: PIP5K selectively dominated in small corrals. These contrasting results underscore how controllable the size-dependency of enzymatic reaction rates can be.

Activation of membrane signaling in physiological systems often involves increasing the activity of a kinase to overcome the suppressing activity of phosphatases. Effects of reaction size confinement on this balance for the PIP5K:OCRL system are illustrated through a set of PIP5K titration experiments shown in Fig. 2-4C. The competitive reaction is run on a series of membrane corral arrays, spanning a factor of 100 in surface area (2 μm x 2 μm to 20 μm x 20 μm), at fixed OCRL concentration (1μM) and a series of PIP5K

concentrations ranging from 2 – 10 nM. Although in all cases, the competitive reaction exhibits two well-defined possible outcome states, the PIP5K concentration at which switching between these states occurs exhibits a sharp dependence on reaction size (Fig. 2-4D). The size range we tested here resembles the length scale of larger geometrical features in cellular systems, such as filopodia, lamellipodia, and polarization in the plasma membrane. The concentration range of PIP5K also falls within physiological expression levels(*51*).

The competitive reaction between Ras activation by SOS and deactivation by the p120 Ras GAP exhibits a similar size-dependency of reaction outcome (Fig. S2-6). This effect is observed for SOS_{HDPC} but not SOS_{cat} (Fig. S2-7), and follows consistently with our observation that SOS_{HDPC} exhibits substantially greater size-dependent activity than SOS_{cat}. Both of these SOS constructs have positive feedback, but their difference lies in the degree of processivity. The lipid-binding properties of SOS_{HDPC} enable it to linger at the membrane for longer dwell times than SOS_{cat} in these experiments. As such, stochastic variation in enzymatic reaction rate resulting from enzyme binding and desorbing from the membrane is amplified for SOS_{HDPC} relative to SOS_{cat}, and these stochastic fluctuations are key to the strength of reaction size-dependency. Note that SOS_{cat} and SOS_{HDPC} are truncated forms of SOS and that the native full-length SOS protein is extremely processive (*44*, *49*, *50*).

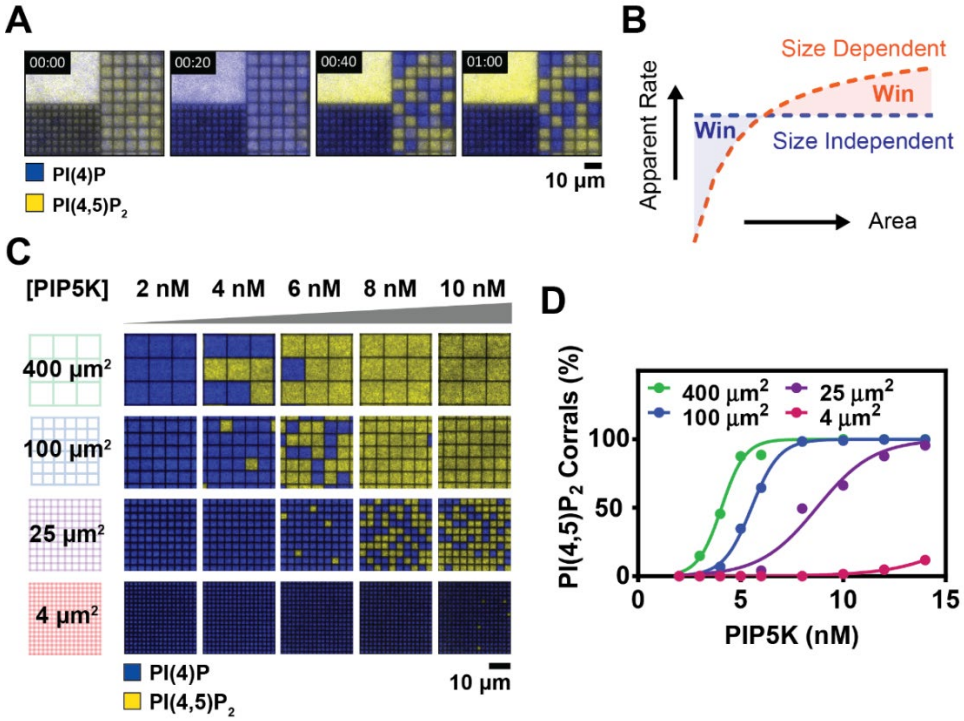

Figure 2-4. Size-dependent reaction speed controls the reaction outcome in a competition reaction. (A) Time sequence of the competition reaction of 10 nM PIP5K and 700 nM OCRL monitored by 20 nM Alexa488-PLCδ_{PH} and 20 nM Cy3-DrrA in 2μm × 2μm corrals, 5μm × 5μm corrals, as well as the unrestricted free bilayer. **(B)** Size-dependent reaction speed in a competition reaction can lead to a change of reaction outcome based on size. **(C)** Images of the final steady-state outcome for a series of 4% PI(4)P membrane with surface areas ranging from 400 μm^2 to 4 μm^2 when exposed to various concentrations of PIP5K and a fixed 1 μM OCRL. **(D)** The probability of the $PI(4,5)P_2$ enriched reaction outcome for a series of 4% PI(4)P membrane with different dimensions at 1 μM OCRL and various concentrations of PIP5K. The data is fitted with a general sigmoidal equation.

2.5 Size-dependency of reaction rate arises from a stochastic mechanism

We investigate the underlying mechanism of reaction size-dependence of catalytic activity with stochastic kinetic modeling of the basic Michaelis-Menten enzymatic process. The reaction scheme for the interfacial enzymes considered here is depicted in Fig. 2-5A. The enzyme in solution (E_0) is recruited to and desorbs from a membrane-bound state (E_1) via overall kinetic rate parameters (k_{on} and k_{off}), which are not necessarily constants since they may depend on membrane composition (e.g. concentration of the enzymatic product). On the membrane, the enzyme interacts with the substrate (S), forming an enzyme-substrate complex (E_1:S) with overall kinetic rates (k_f and k_r), from which the product is formed with a catalytic rate constant (k_{cat}). We perform stochastic kinetic modeling of this reaction scheme using a Gillespie algorithm(*52*), describing the state vector for the system in terms of discrete copy numbers of each species on the membrane (E_1, S, E_1:S, P). The concentration of the solution species, E_0, is fixed, reflecting the experimental condition where there is a large reservoir of enzymes in solution. Transitions between states are described with transition probabilities, corresponding with each of the kinetic rates, some of which are functions of the state of the system (full detail in Materials and Methods). This modeling is spatially homogeneous (matching experimental conditions), and the system size in spatial dimensions maps to different overall molecular copy numbers in the simulations.

Stochastic kinetic modeling readily reproduces the experimental observation of reaction size-dependent catalytic activity, while deterministic rate equations fail to predict such effects. Sets of reaction trajectories for the same enzymatic system in differently sized membrane corral arrays are shown in Fig. 2-5B. As expected, stochastic variation clearly becomes more pronounced in the smaller corrals. More importantly, the mean catalytic activity also differs. Mean reaction trajectories from these simulations on 1 μm^2 and 0.25 μm^2 arrays are plotted in Fig. 2-5C in the same format used for the presentation of experimental data in Fig. 2-2, illustrating the substantial agreement between modeling and experiment results (see supporting information for discussion). If membrane binding of the enzyme is decoupled from product density, effectively removing the positive feedback, size-dependency of the reaction rate is lost (Fig. 2-5D and S2-8).

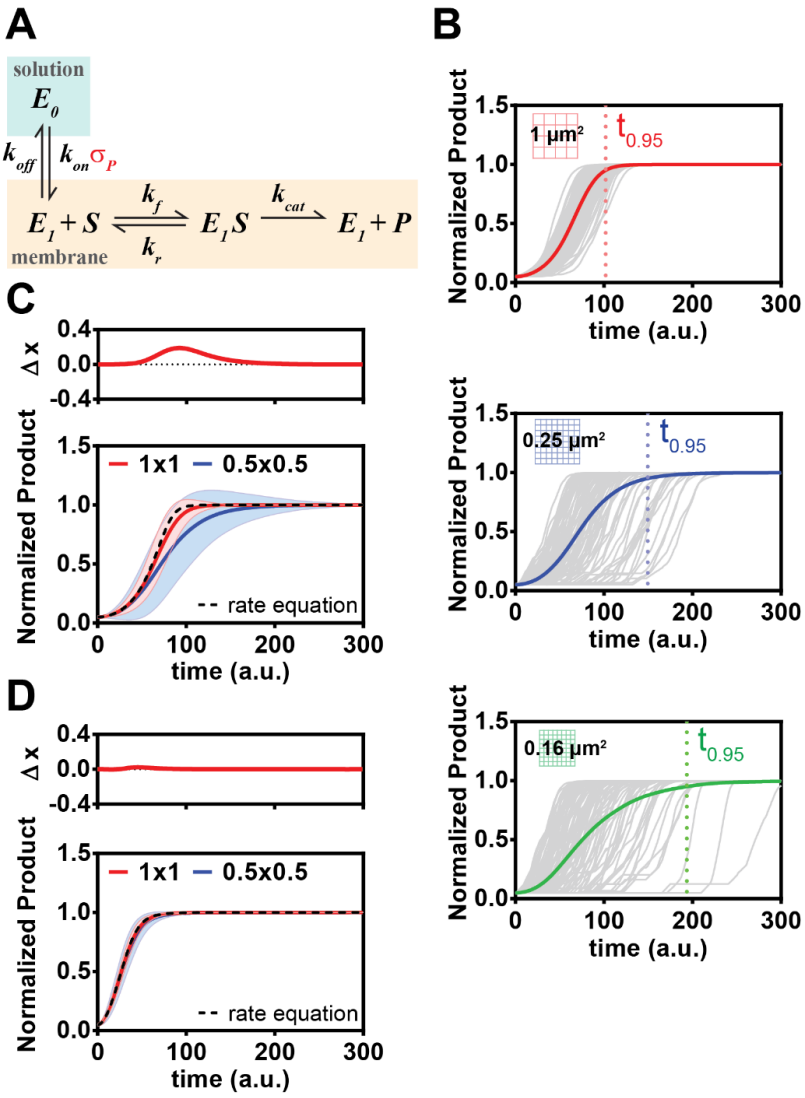

Figure 2-5. Size-dependent reaction speed modulated by reaction discreetness and enzyme processivity. (A) Kinetic scheme for stochastic kinetic modeling. The interfacial enzyme binds to a membrane from the solution and catalyzes a surface Michaelis-Menten reaction at the membrane. Positive feedback is included by having the enzyme on rate dependent on σ_P (density of product on the membrane). **(B)** Kinetic traces from 1000 stochastic simulations plotted with their mean (colored lines) using the reaction mechanism described in panel A. Top: Simulation in 1 μm^2 membrane. Middle: Simulation in 0.25 μm^2 membrane. Bottom: Simulation in 0.16 μm^2 membrane. $t_{0.95}$ marks the time for the average to reach 95% completeness of reaction. **(C)** Average of kinetic traces from stochastic simulations in 1 μm × 1 μm (1 μm^2) membrane and 0.5 μm × 0.5 μm (0.25 μm^2) membrane plotted together. Simulation with deterministic rate equation was plotted in dashed line. The shaded area shows the standard deviation. The top graph shows the difference between the reaction trajectory in 1 μm^2 and 0.25 μm^2 arrays, Δx, at each time point. The difference of normalized product at max Δx is significant at p-value < 0.01. **(D)** Simulation with no positive feedback (on rate independent of σ_P).

To conceptually illustrate the underlying physical mechanism of size-dependency in reaction rate, we construct a highly simplified stochastic system that still exhibits the basic effect. In this example, consider a molecule that binds to a surface in a one-way process with a kinetic rate that depends on the surface concentration of already bound molecules (positive feedback) (Fig. 2-6A). We can examine the overall reaction rate by looking at the mean first passage time (MFPT) for the system to double the density of adsorbed molecules (σ). Fig. 2-6A depicts the density doubling process (copy number n molecules goes to $2n$) for several different sized systems, starting from n = 1, 2, or 3 adsorbed molecules, at equivalent starting surface density. The number of individual molecular binding events required for density doubling goes as n and the probability distribution for doubling time, τ_D, is given by successive convolution of the individual transition time distributions for each of the n transitions: $p(\tau_D) = p_1(\tau_1) \otimes p_2(\tau_2) \otimes p_3(\tau_3) \cdots \otimes p_n(\tau_n)$. For this one-way adsorption process, the MFPT for doubling is simply the average doubling time, $\langle \tau_D \rangle$, and since this is a Markov process, $\langle \tau_D \rangle = \sum_{i=1}^{n} \langle \tau_i \rangle$.

For the case of simple binding, with no feedback, the overall rate of binding to a surface with area, A, is independent of the number of already adsorbed molecules and given by kA. With this constant rate of binding, the delay time between each of the individual binding events follows an identical Poisson interval distribution, $p(\tau) = kAe^{-kA\tau}$ and $p(\tau_D)$ is the corresponding gamma distribution: $p(\tau_D) = (kA)^{(n+1)} {\tau_D}^n e^{-kA\tau}/n!$. In this case with zero-order feedback, the MFPT for doubling is independent of system size and identical to the value calculated from a continuum approach with deterministic rate equations (Fig. 2-6B; also see Materials and Methods).

When there is positive feedback (of order m) affecting the adsorption process, the MFPT for density doubling is calculated as above, except now the intermediate transitions no longer occur with an identical rate. For a system starting with n molecules, the i^{th}transition has rate $k\sigma^m A$, where $\sigma = (n + i - 1)/A$ is the momentary density of adsorbed molecules while waiting for the i^{th} transition event. The rate of each successive step now depends on σ and correspondingly increases, reflecting the positive feedback as a function of already adsorbed molecules. Plots of doubling MFPT *vs*. system size for feedback of order m = 1, 2, and 3 are shown in Fig. 2-6B. With the positive feedback, a system size dependence of the overall reaction rate is evident with the reactions going more slowly in smaller systems. At larger system sizes, the stochastic analysis converges on the same result (dashed lines) obtained from continuum deterministic rate equations.

Fundamentally, stochastic effects originating from the discrete binding of molecules to the surface reduce the efficiency of the positive feedback. In the extreme case of beginning with a single molecule, the MFPT for doubling essentially never experiences any effects of feedback since the process is finished with the first transition. As systems get progressively larger, and more individual steps are taken throughout the reaction trajectory to achieve the same density doubling, each successive step occurs faster as the system is able to respond to the now gradually increasing density (Fig. 6C). Effects of feedback are maximized in large systems, where the surface density of adsorbed molecules essentially varies continuously.

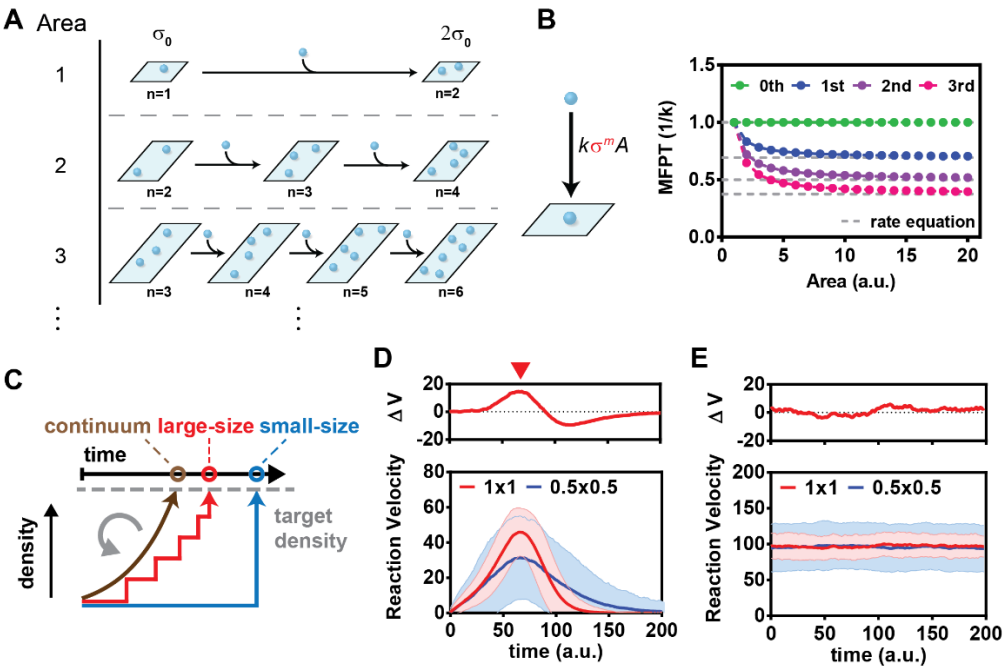

Figure 2-6. Size-dependent reaction speed based on positive feedback through recruitment. (A) A kinetic model of a surface binding process. Surfaces with different areas start with the same density σ_0 and can bind molecules with a defined kinetic rate to evolve to density state $2\sigma_0$. (B) Left: The kinetic scheme for direct positive feedback binding. $k\sigma^m A$ is the binding rate. m is the order of positive feedback. In the case of m=0 there is constant membrane binding with no positive feedback. Right: The MFPT for different surface areas to reach σ=2 with direct positive feedback binding kinetics. (C) Membrane size alters the continuity of positive feedback. Discontinuity becomes more prominent in smaller system sizes. Deviation from continuous positive feedback leads to a weaker positive feedback and slower overall reaction. (D) Figure 5C plotted in reaction velocity vs. time. The shaded area shows the standard deviation. Top graph shows the reaction velocity difference (ΔV) between 1 μm^2 and 0.25 μm^2 arrays. The red arrow indicates the time point where ΔV is at maximum. (E) Stochastic simulations at a fixed substrate and product densities plotted in reaction velocity vs. time. The condition corresponds to the membrane composition at the red arrow in Fig. 2-6D.

2.6 Size-dependency of reaction rate is a non-equilibrium effect

In addition to the stochastic element, the mechanism of reaction size dependency is also intrinsically rooted in the fact that the system is changing. This is clearly demonstrated by examining reaction velocities under steady-state conditions (e.g. as might be done in some classic Michaelis-Menten analyses). Fig. 2-6D illustrates a plot of mean reaction velocity vs. reaction progress for the 1 μm^2 and 0.25 μm^2 corral arrays for the system computationally analyzed in Fig. 2-5B & 2-5C. Marked on the plot is the system composition (substrate and product densities) at which the maximum difference in mean reaction velocity between the two corral sizes was observed. Results from stochastic simulations on the two corral sizes at this composition, but now under steady-state conditions (with substrate and product densities fixed) are plotted in Fig. 2-6E. As expected, reaction velocity variation is substantially larger in the smaller corrals. However, under these steady-state conditions, there is no longer any size-dependency of the mean reaction rate.

The reaction size-dependency effect stems from the enzyme-membrane binding reaction being out of equilibrium, and the way in which this binding reaction stochastically follows the changing membrane composition. This can be shown by running stochastic simulations for the system depicted in Fig. 2-5C in which the positive feedback is preserved, but the individual kinetic rate constants for membrane binding

are allowed to be very fast compared to the catalytic rate (increasing both k_{on} and k_{off} or reducing k_f and k_{cat}). In these situations, the enzyme-membrane binding reaction is always near equilibrium (or quasi steady-state), and the reaction size-dependency correspondingly vanishes (Fig. S2-9). In sufficiently small systems, where individual catalytic steps can appreciably change the system product density, non-equilibrium behavior is essentially assured since the enzyme-membrane binding reaction cannot synchronously follow the stochastic steps of the catalytic reaction. However, we also observe reaction size sensitivity in systems with relatively high substrate density (e.g. Fig. 2-5C). In these cases the enzymes are significantly processive, driving more than 100 catalytic cycles per binding event at the early stages of the reaction. This dramatically amplifies stochastic variation in the overall reaction velocity, and correspondingly amplifies size sensitivity. We note that positive feedback and a nonequilibrium reaction cycle are the necessary and sufficient conditions for reaction size sensitivity. Enzymatic processivity is an amplifier of these effects, but is not required. Reaction size sensitivity can be readily detected without any processivity at sufficiently low total substrate density (Fig. S2-10).

2.7 Discussion

The impacts of size and geometry of cellular structures on intracellular biochemical reactions and signaling processes have previously been considered in a variety of different contexts. For example, cell shape has been shown to direct stronger cyclic adenosine monophosphate (cAMP) signaling in the dendrites of neuronal cells through the interplay between reaction-diffusion and changes in surface to volume ratios(*53*). In an analogous mechanism, mitogen-activated protein kinase (MAPK) phosphorylation level upon EGF stimulation can be enhanced in elliptic cells compared to circular cells(*54*). In these examples, where the reaction occurs at the membrane but the effector diffuses through solution, effective changes in local surface area to volume ratios caused by membrane bending and cell shape can establish zones of higher reactivity or depletion of the effectors and consequently alter local or global reaction outcome(*19*, *53–55*). Size sensing behavior has also been reported in the depolymerization of microtubules(*56*) and actin filaments(*57*). In these cases, the size-dependent effects originate from a lower dimensional version of the surface area to volume ratio—the length to end-point ratio. Elongating filament length increases the number of available binding sites per filament and recruits more enzymes. Processive movement of the enzyme toward the end of the filament then leads to concentrated activity at the end of the filament that is proportionate with its length. The size sensitivity in mean catalytic rate that we report here, however, is quite distinct from these other processes. It is not dependent on an interdimensional ratio, such as surface area to volume, nor are there any requirements on diffusion or enzymatic processivity. Also, unlike the examples mentioned above, and the beautiful spiraling Turing patterns exhibited by the Min system(*58*), the size sensitivity we describe is not predictable by continuum mathematical descriptions of reaction kinetics: this size sensitivity is intrinsically stochastic.

The patterned supported membrane experimental platform provides a unique way to isolate the effects of system size from other geometrical features, such as membrane curvature. For the lipid kinase-phophatase reactions studied here, this resolving capacity confirms that it is size, not curvature, that led to the observed differential kinetic rates. However, membrane curvature is a major aspect of physiological membrane systems and there is significant interest in curvature driven effects. Studies on the regulation of lipase and phospholipase activity by curvature are notable examples. Classical as well as modern research performed on this topic mainly utilizes liposomes of different sizes to represent different curvatures, leading to discoveries of diverse curvature sensing mechanisms(*33*, *34*). Depending on feedback characteristics of the enzymes(*59*), such experimental observations may also be influenced by size-dependent reaction effects as

described here. Planar supported membrane microarrays could be useful in control experiments to distinguish these mechanistic details.

We have demonstrated that even the extremely minimal system consisting of an ensemble of identical soluble enzymes acting on a membrane substrate can exhibit reaction size-dependent mean catalytic rate. For a pair of such enzymes in a competitive reaction, this effect can lead to complete reaction inversion, in which the final product depends on the system size. Although these effects arise through a stochastic mechanism, the results are not random and can be achieved with almost complete certainty. Reaction size-dependency of an interfacial enzymatic reaction emerges when two conditions are met: *i*) the enzyme exhibits feedback, and *ii*) the intermediate binding interaction between enzyme and membrane is not well equilibrated with the changing membrane composition. Feedback is a genetically encodable (and engineerable) property of the enzyme while the non-equilibrium characteristic is a property of the reaction system. These requirements are so basic, and simply met, that we suggest it is unavoidable that they occur within cells and possibly govern some biological functions. In addition to the enzymatic reactions studied here, many important signaling events that involve the activation of membrane substrate by soluble enzymes, such as activation of Cdc42(*60*, *61*), RhoA((*62*), Rab-5(*63*), Arf-1 and Arf-6(*64*) have been shown to exhibit positive feedback. Vesicle budding and fusion processes(*65*), protrusion and retraction of membrane structures such as filopodia and lamellipodia(*66*), as well as the formation of receptor signaling domains and protein condensates at the membrane(*67*) all represent dramatic changes in spatial confinement coupled with membrane signaling activity. All of these situations, and many others in cells, present viable opportunities for size-dependent reaction rates to be utilized in a regulatory mode.

2.8 Supplemental text

2.8.1 Hill equation fit

An estimate of feedback strength can be obtained by fitting the kinetic data to a Hill equation. For the PTEN reaction data in Fig. 2-2C, fitting to a general sigmoidal function (Hill equation) reveals the Hill slope is higher for the mean reaction trace in a free lipid bilayer compared to that for the mean reaction trace in 5 μm × 5 μm corrals (Fig. S2-11). This suggests that the reaction exhibits stronger feedback in the larger size reaction. When fitting the maximum reaction velocity versus PTEN concentration plot to a Hill equation, a higher Hill slope is observed in a free lipid bilayer compared to 5 μm × 5 μm corrals as well (Fig. S2-12).

2.8.2 Additional discussions on stochastic kinetic modeling

The stochastic simulation model (Fig. 2-5) is a minimal model that can still capture the size sensing behavior experimentally observed. It is not, however, a literal attempt to model the data and some differences are noted. Specifically, the simulations exhibit a noticeable spread in delay time before each trace starts to react, while in the experiment this is not observed. This results because, in the simple model, enzyme recruitment to the membrane is strictly through binding to its product at the membrane (see Material and Methods for further detail). In this case, the initial enzyme recruitment is limited by the low number of product molecules on the membrane, and will abruptly start the

reaction once the first enzyme binds. In the experimental conditions, however, enzymes can slowly catalyze the reaction directly from the solution by random collisions, without being strongly anchored to the membrane. This provides a steady slow reaction rate before the first enzyme binds and smooth out the delay. This is demonstrated in simulations that incorporate an additional catalytic mechanism for the enzyme directly from the solution (see Material and Methods for further detail). These simulation results exhibit a delay time spread more reminiscent of the experimental data (Fig. S2-13). The artificially wide spread in start times in the simple model, however, averages to essentially the same mean when a large number of statistics are collected (1000 traces) and has no effect on the overall results. Moreover, the observed size dependency in mean reaction speed in the minimal model (Fig. 2-5) is not caused by the larger spread of reaction traces in small sizes (Fig. S2-14).

2.9 Supplemental figures

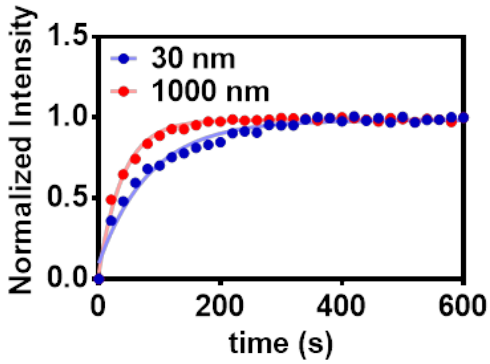

Fig. S2-1. Kinetic traces of PTEN catalyzed PI(3,4,5)P_3 reaction on 30 nm and 1000 nm liposomes. The reaction of 200 nM PTEN converting 10 μM of PI(3,4,5)P_3 to PI(4,5)P_2 monitored by phosphate release. Apparent rate constant k is obtained by fitting to 1-exp(-kx). 30 nm: k = 0.012; 1000 nm: k = 0.025

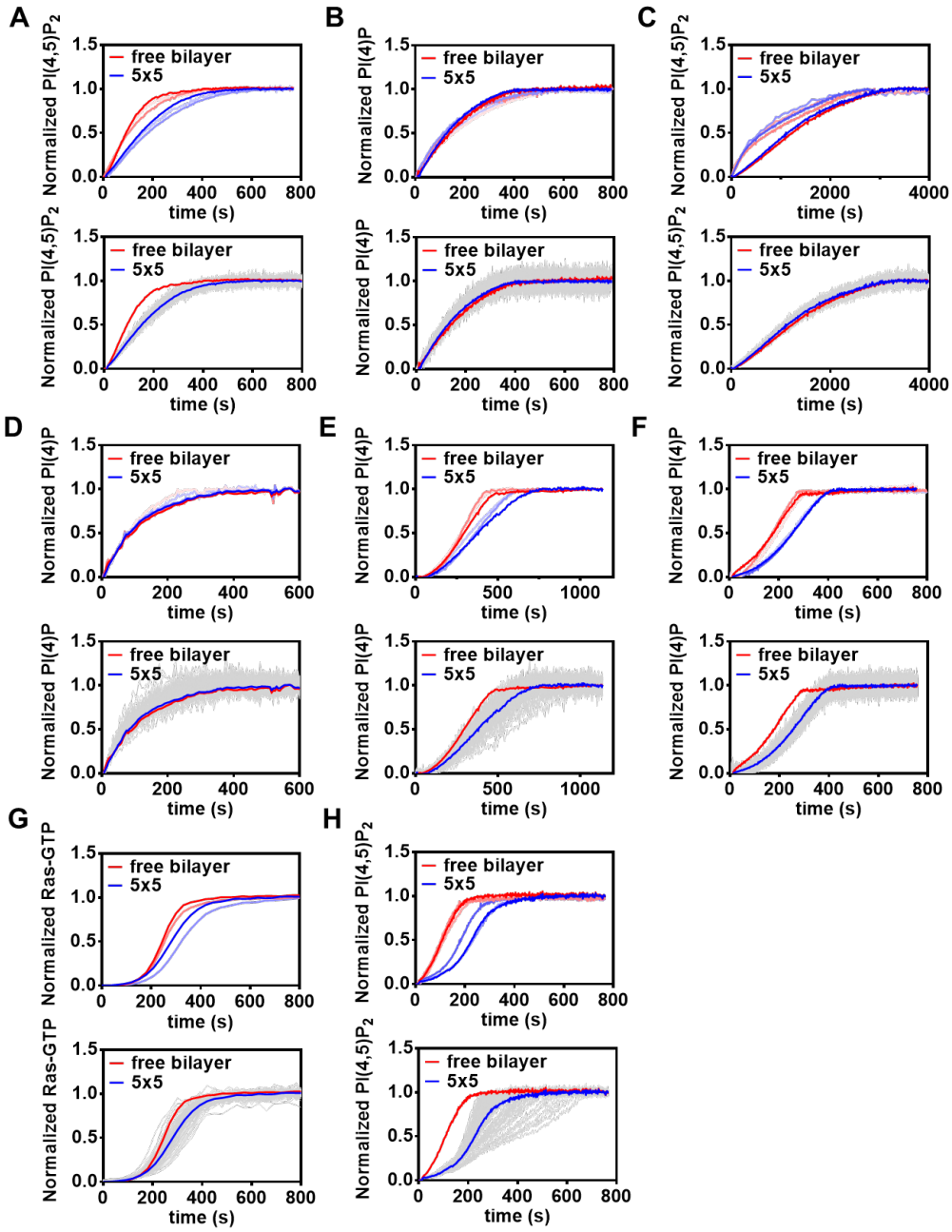

Fig. S2-2. Replicates and individual kinetic traces of corral assay. Top: Replicates of the corral assay. Bottom: Individual kinetic traces from a corral assay plotted with the mean. 100 individual traces in 5μm × 5μm corrals are plotted in grey. **(A)** $PI(3,4,5)P_3$ to $PI(4,5)P_2$ reaction catalyzed by 100 nM PTEN. **(B)** $PI(4,5)P_2$ to PI(4)P reaction catalyzed by 50 nM $OCRL_{PD}$. **(C)** $PI(3,4,5)P_3$ to $PI(4,5)P_2$ reaction catalyzed by 23 μM $PTEN_{\Delta PBD}$. **(D)** $PI(3,4)P_2$ to PI(4)P reaction catalyzed by 3 μM PTEN. **(E)** $PI(3,4)P_2$ to PI(4)P catalyzed by 170 nM PTEN-DrrA. **(F)** $PI(4,5)P_2$ to PI(4)P reaction catalyzed by 100 pM DrrA-$OCRL_{PD}$. **(G)** Ras-GDP to Ras-GTP reaction catalyzed by 20 nM SOS_{HDPC}. **(H)** PI(4)P to $PI(4,5)P_2$ catalyzed by 2 nM $PIP5K_{KD}$.

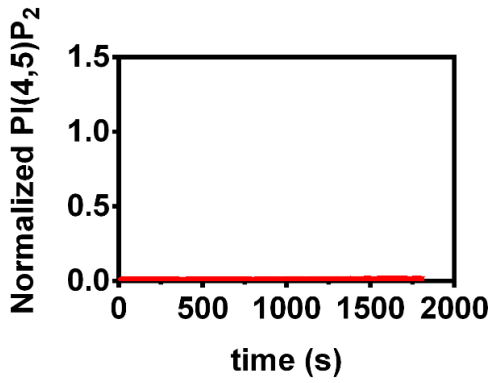

Fig S2-3. Reaction trace of $PTEN_{\Delta PBD}$ in the absence of PS. $PI(3,4,5)P_3$ to $PI(4,5)P_2$ reaction catalyzed by 20 μM $PTEN_{\Delta PBD}$ on free bilayer. Membrane composition is 98% DOPC. 2% $PI(3,4,5)P_3$.

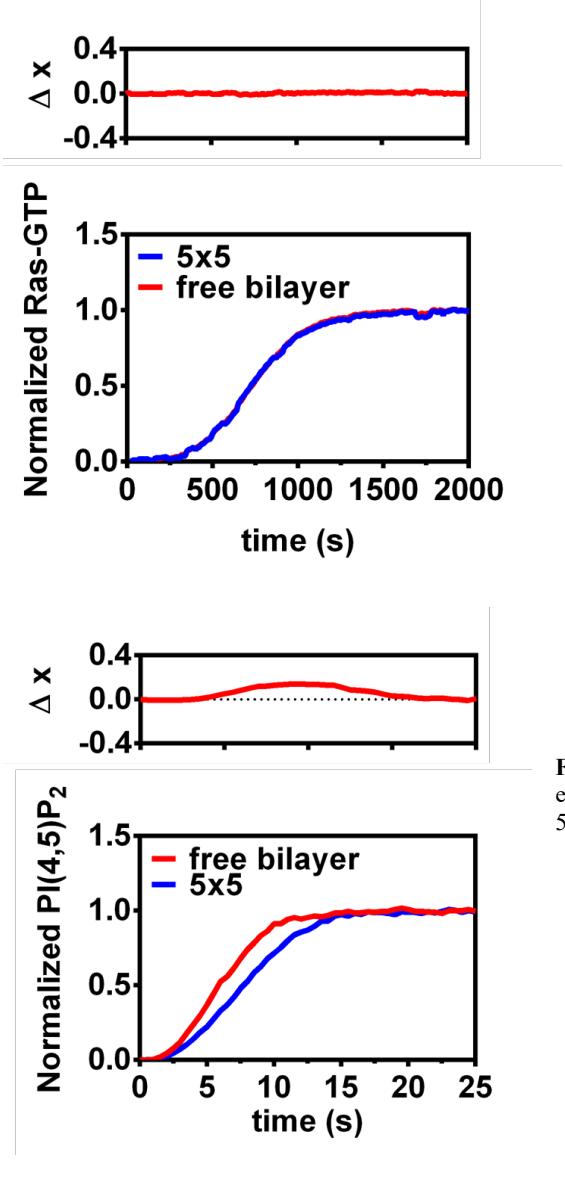

Fig S2-4. Reaction traces of PTEN in the presence of PS. Dephosphorylation reaction of $PI(3,4,5)P_3$ to $PI(4,5)P_2$ by 23 μM PTEN in 5μm x 5μm of membrane corrals and free bilayer. Membrane composition is 93% DOPC. 2% $PI(3,4,5)P_3$, and 5% PS.

Fig S2-5. SOS_{cat} catalyzed Ras-GDP to Ras-GTP reaction. Nucleotide exchange reaction of Ras-GDP to Ras-GTP catalyzed by 2 nM SOS_{cat} in 5μm × 5μm membrane corrals and free bilayer.

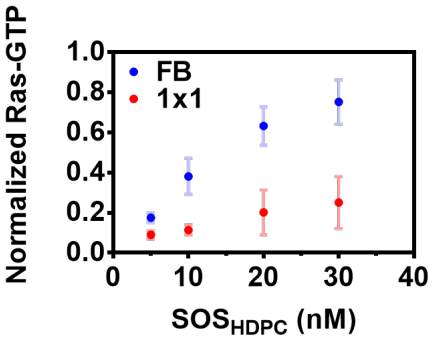

Fig S2-6. The steady-state level of Ras-GTP in SOS$_{HDPC}$ and p120GAP competition reaction. SOS$_{HDPC}$ competition with 200 nM p120GAP in1 μm × 1 μm membrane and free bilayer. Smaller reaction size leads to lower Ras-GTP steady state in the competition reaction.

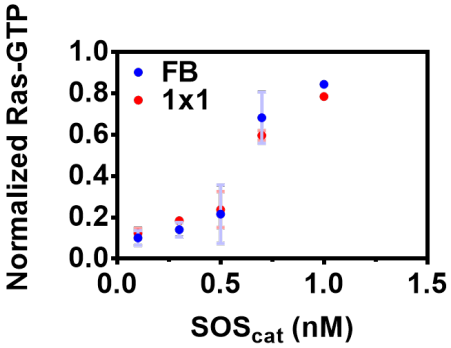

Fig S2-7. The steady-state level of Ras-GTP in SOS$_{cat}$ and p120GAP competition reaction. SOS$_{cat}$ competition with 200 nM p120GAP in 1 μm × 1 μm membrane and free bilayer. The Ras-GTP steady state of the competition reaction is independent of reaction size.

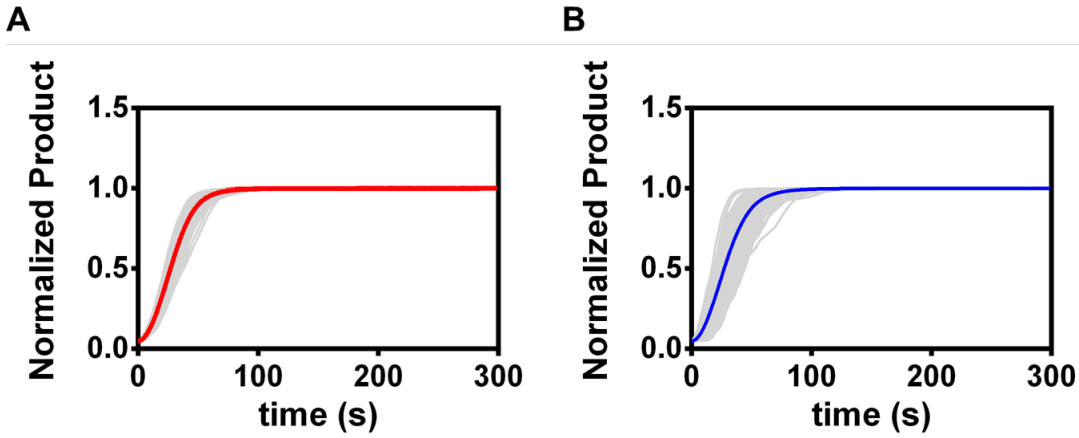

Fig S2-8. Individual kinetic traces from Fig. 2-5D (reaction with no positive feedback). (A) Kinetic traces from 1000 stochastic simulations in 1 μm^2 membrane plotted with their average. (B) Kinetic traces from 1000 stochastic simulations in 0.25 μm^2 membrane plotted with their average.

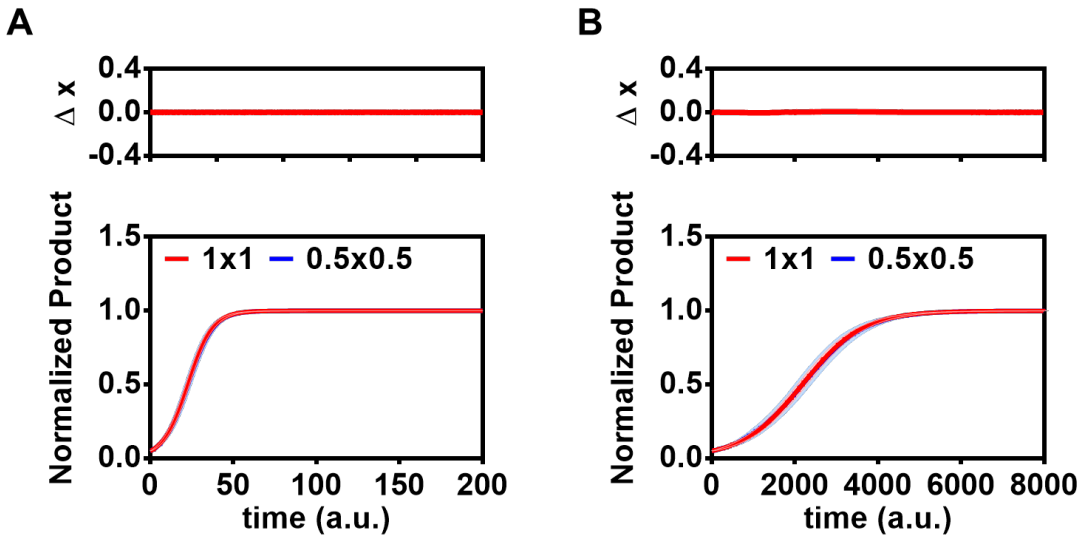

Fig S2-9. Stochastic simulation with near-equilibrium enzyme binding (non-processive enzyme catalysis) at high substrate density. (A) k_{on} and k_{off} were increased by 100 times, leading to a fast enzyme binding response to membrane composition change. **(B)** k_f and k_{off} were decreased by 50 times. Total substrate density is 28000/ μm^2.

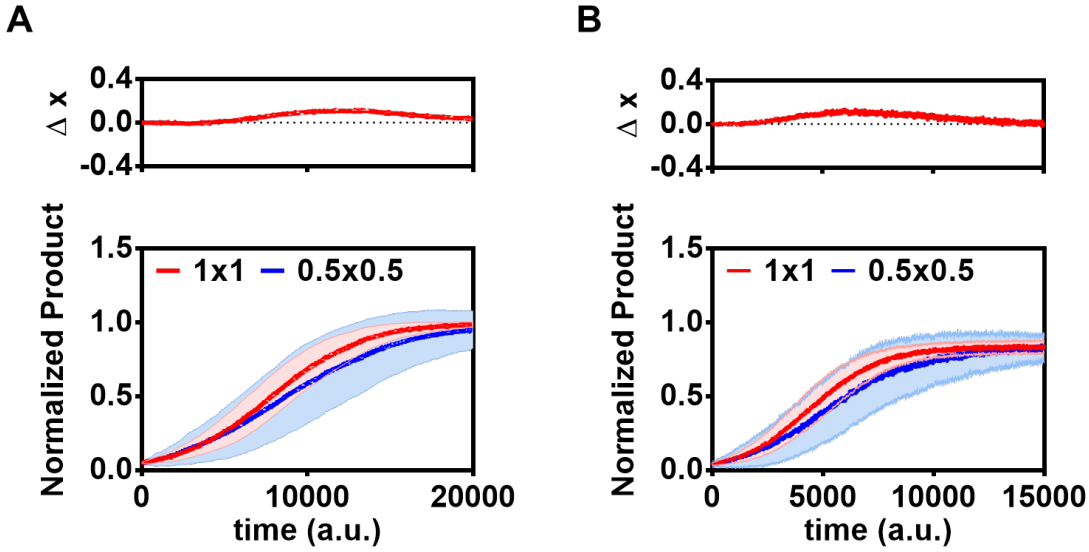

Fig S2-10. Stochastic simulation with near-equilibrium enzyme binding (non-processive enzyme catalysis) at low substrate density. (A) k_{on} and k_{off} were the same in Fig. S10A. **(B)** k_f and k_{off} were the same in Fig. S10B. Total substrate density is 80/

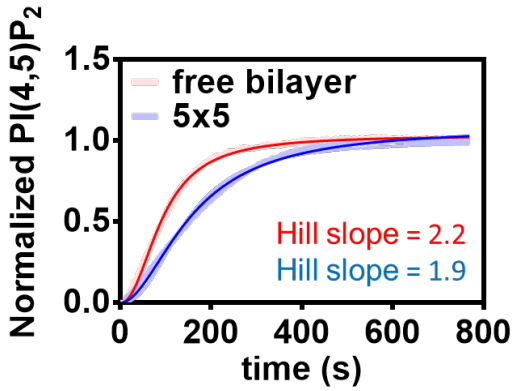

Fig S2-11. Analysis of the kinetic traces of PTEN reaction in Fig. 2C. The maximum velocity is 208/um^2/s in free lipid bilayer and 160/um^2/s in 5μm × 5μm corrals. Hill slope is 2.2 for the reaction in free lipid bilayer and 1.9 for the reaction in 5μm × 5μm corrals.

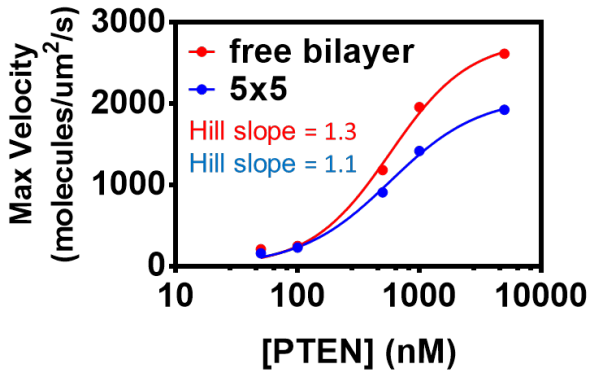

Fig S2-12. Maximum velocity versus PTEN concentration. Hill slope is 1.3 for the reaction in free lipid bilayer and 1.1 for the reaction in 5μm × 5μm corrals.

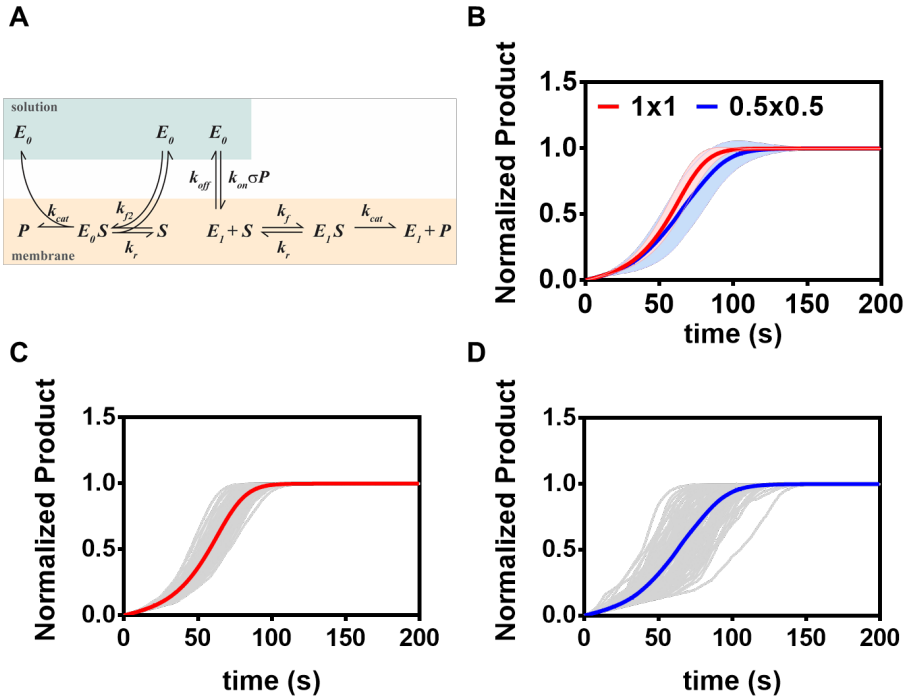

Fig S2-13. Stochastic simulation with the incorporation of additional catalysis mechanism from the enzyme, where the enzyme in the solution can randomly perform reaction without binding anchored to the product at the allosteric site. (A) Kinetic scheme for the stochastic kinetic modeling. In addition to the reactions described in Figure 5A, we have included the enzyme catalysis directly from the solution from random collision (see methods for details). (B) Average of kinetic traces from stochastic simulations using the reaction mechanism described in panel A in 1 μm × 1 μm (1 μm^2) membrane and 0.5 μm × 0.5 μm (0.25 μm^2) membrane. The shaded area shows the standard deviation. (C) Individual kinetic traces from 1000 stochastic simulations in 1 μm^2 membrane plotted with their average. (D) Individual kinetic traces from 1000 stochastic simulations in 0.25 μm^2 membrane plotted with their average.

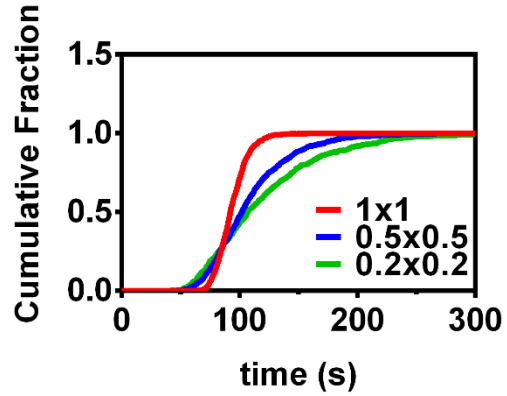

Fig S2-14. Cumulative distribution of time for simulated reactions in Fig. 5B to reach 95% reaction completeness. The median is at 0.5 cumulative fraction. Median: 92.1 a.u. for 1 μm^2; 101.9 a.u. for 0.25 μm^2; 107.2 a.u. for 0.16 μm^2.

Chapter 3

BIMODALITY IN RAS SIGNALING ORIGINATES FROM PROCESSIVITY OF THE RAS ACTIVATOR SOS WITHOUT CLASSIC KINETIC BISTABILITY

Ras is a small GTPase that is central to important functional decisions in diverse cell types. In lymphocytes, Ras is activated in a bistable manner that enables decisive cellular responses. Such signaling behavior is controlled by competing activation-deactivation of Ras by guanine nucleotide exchange factors (GEFs) and GTPase activating proteins (GAPs), and the Ras activator Son-of-Sevenless (SOS) is critical for mediating the bistable Ras activation. Here, we describe the total reconstitution of receptor-mediated Ras activation-deactivation cycle catalyzed by SOS and p120-RasGAP on micropatterned supported lipid bilayers. Combining both experimental and in silico studies, we have revealed that the bistable response in Ras activation is originated from stochasticity. Such stochastic bistability is caused by the ability of SOS to enter a uniquely long-dwelling, highly processive state. Moreover, we demonstrated that the bistable response is dependent on the signaling environment, such as the density of Ras and LAT (linker for activation of T cells) at the membrane. These observations reveal a previously unanticipated mechanism of bimodal response in Ras signaling, and a possible explanation of how clustering of signaling molecules, such as forming LAT clusters or Ras clusters, can govern the response of Ras signaling in cells.

3.1 Introduction

The small GTPase Ras functions as a molecular switch, toggled between GTP- and GDP-bound states, where only the GTP bound state is able to interact with and activate downstream effector molecules(*68*). Ras activates a variety of signaling pathways, such as MAPK and PI3K, that affect cellular proliferation, survival, and differentiation(*69*, *70*). The activation-deactivation cycle of Ras is dependent on regulatory enzymes that control Ras signaling according to upstream signals(*3*, *71*). GEFs, such as SOS, promote the exchange of GDP for GTP to activate Ras (*72*, *73*) while hydrolysis of GTP to GDP is promoted by GAPs(*74*). Under physiological conditions, Ras activation and deactivation reactions are in constant competition and must be tightly regulated; mis-regulation of Ras is a major cause of cancer(*75*). Decades of focused studies on the Ras signaling mechanism have revealed many detailed biochemical insights(*76*), such as its interaction with various effectors (*70*, *73*, *74*), conformational dynamics(*77*, *78*), and its potential to dimerize and form clusters(*79–84*). Despite this continuously improving understanding, the Ras signaling mechanism remains enigmatic and difficult to pharmacologically control(*76*, *85*, *86*).

An important feature of physiological Ras-MAPK signaling is its apparent ability to signal in a bimodal manner(*87–94*). This has the effect of converting a continuously variable input to the signal pathway (e.g. the number of activated receptors) into a binary output response, and is of extremely general importance in biological information processing(*95–97*). In lymphocytes, this bimodal signaling behavior has been ascribed to the feedback kinetics of SOS(*89*, *90*, *98*, *99*) —specifically a RasGTP-driven positive feedback loop. However, this conjecture is based exclusively on computational modeling and indirect measurements in cellular systems: experimental observation of bimodality in the isolated Ras activation response has not previously been reported(*100*). One contributing factor to the challenges presented by Ras is the surprising complexity that can emerge from competitive enzymatic reaction cycles, especially when a membrane is involved (*6*, *101–103*).

SOS is a ubiquitously expressed Ras GEF that resides in the cytosol and is recruited to the membrane to initiate Ras activation. SOS is structurally organized with an N-terminal histone-fold (HF), pleckstrin homology (PH) and Dbl homology (DH) domains, a catalytic core that has a Ras exchanger motif (REM) and a Cdc25 domain, followed by a C-terminal proline rich (PR) domain(*72*). SOS is subjected to complex regulation, including autoinhibition(*104*), and allosteric activation by Ras(*48*). RasGTP-driven positive feedback in SOS activity has been observed in bulk experiments, and attributed to nucleotide selective allosteric activation of SOS by RasGTP(*48*). In earlier modeling studies, SOS was typically assumed to have conventional allosteric activation with different catalytic rates depending on whether RasGDP or RasGTP was bound to its allosteric site (*39*, *89*, *105*, *106*). When coupled with a competing reaction, this type of positive feedback can lead to kinetic bistability, in which two stable steady states of Ras activity level may exist(*95*, *107*). Such a classic kinetic bistability in the activation of Ras by SOS has been presumed to underlie the bimodal signaling response observed at the cellular level in lymphocytes(*89*, *90*, *98*, *99*). The first direct single molecule studies of SOS activity on membranes, however, complicated the story by revealing essentially identical average catalytic rates of SOS with either RasGDP or RasGTP in the allosteric binding site—thus eliminating the possibility of a simple positive feedback mechanism based on allosteric enhancement of catalytic activity(*39*). Further single molecule studies with the full-length SOS protein have gone on to resolve a complex autoinhibition release mechanism (*50*), which is coupled to the LAT(*44*) (or EGFR(*108*)) protein condensation phase transitions. Once activated, SOS is highly processive and can activate hundreds of Ras molecules during a single membrane binding event(*39*, *44*, *50*). Collectively, these more recent experimental studies reveal an entirely different activation process in the SOS-Ras system and motivate a comprehensive reevaluation of the mechanistic origins of its bimodal signaling response.

Here, we employ a total reconstitution approach to study dynamics of Ras activity on a membrane. The experimental system includes the native machinery of receptor-mediated Ras activation by SOS in T cells, consisting of the phosphorylated LAT (pLAT) protein, PIP_2 lipids, and Ras in a supported membrane along with Grb2, full-length SOS (SOS^{FL}) or truncated constructs, p120Gap, and GTP in solution. This system captures the Grb2-mediated recruitment of SOS^{FL} to activated receptor scaffold (pLAT in this case), the membrane-mediated process of SOS autoinhibition release (including PIP_2 and allosteric Ras binding), SOS-catalyzed nucleotide exchange in Ras, and the dynamic competition with GAP-mediated Ras deactivation. The Ras activity state is read in real-time through binding of a fluorescently labeled Ras binding domain (RBD) of the downstream effector, Raf(*44*). Experiments are run on supported membrane microarrays, enabling simultaneous measurement of thousands of Ras activation-deactivation reactions at the membrane, all exposed to the same signaling environment from the solution. The microarray strategy also enables observation of stochastic effects in reaction systems of controlled, physiological sizes.

The experimental results reveal a distinctive scale-dependent bimodality in Ras activity state with SOS^{FL}. The bimodal response is only observed in small corralled reaction systems, indicating that this effect does not originate from classic kinetic bistability(*6*). The system becomes monostable at larger sizes, even while all other parameters are maintained identical. We further observe that the truncated catalytic core of SOS (SOS^{Cat}) is incapable of driving a bimodal Ras activity response under any experimentally accessible conditions. SOS^{Cat} includes both the catalytic and allosteric Ras binding sites and exhibits Ras-GTP driven positive feedback, which nonetheless proved insufficient to establish kinetic bistability and is not the primary driver of the observed bimodal Ras signaling response. Through a combination of studies using other SOS truncations, along with stochastic kinetic modeling, we establish that it is the extreme processivity of SOS that enables the bimodal signaling response through a stochastic mechanism. Individual molecular SOS activation events drive bursts of Ras activation, which locally overcome RasGAP activity even under strongly deactivating conditions. This behavior contrasts that of bimodality driven by positive feedback, in which Ras activation is much more distributed. Processivity-driven stochastic bimodality is markedly insensitive to SOS inhibition, suggesting it could present challenges to the development of effective therapeutics to inhibit Ras activation by targeting SOS(*76*, *109–112*). We also observe that bimodal Ras activity is dependent on system size as well as local density of Ras or LAT, thus offering more degrees of control than would be available if it were rooted in a classic kinetic bistability. More broadly, these studies reveal how stochastic variation from single molecular SOS activation events can be amplified by the extreme processivity of SOS to drive a full cellular level bimodal Ras signaling response.

3.2 Reconstitution of Ras activation-deactivation competition reaction

The activity state of Ras is controlled by competing GEFs and GAPs that primarily interact with Ras on the cell membrane(*71*, *113*). Many commonly used Ras biochemical assays utilize solubilized versions of Ras and are carried out as solution assays(*48*, *114*). While such assay formats can be convenient, they also eliminate many important regulatory mechanisms(*39*, *44*, *115*). For example, the ubiquitous Ras GEF, SOS, in its full length form, is strongly autoinhibited and shows almost no activity from solution (*44*, *50*). SOS truncations with impaired autoinhibition must generally be used for observable activity in solution assays. Additionally, once activated, SOS is highly processive and can activate hundreds of Ras molecules during a single membrane binding event(*39*, *44*, *50*). This processivity is only possible on membranes and furthermore requires an extended membrane format; conventional vesicles (typically around 100 nm in diameter) can be artificially limiting by allowing SOS to completely activate all available Ras molecules(*116*). Here we seek to reconstitute the entire receptor-mediated recruitment and activation of SOS in a planar membrane format that includes receptor-mediated SOS recruitment via Grb2, lipid- and Ras-dependent autoinhibition release in SOS, as well as inclusion of competing GAP-driven Ras deactivation.

We reconstituted Ras activation-deactivation competition reaction on a supported lipid bilayer (SLB) containing 92% DOPC (1,2-dioleoyl-sn-glycero-3-phosphocholine), 2% PIP_2, 2% MCC-DOPE (1,2-dioleoyl-sn-glycero-3-phosphoethanolamine-N-(4-(p-maleimidomethyl)cyclohexane-carboxamide)), and 4% Ni–NTA-DOGS (1,2-dioleoyl-sn-glycero-3-[(N-(5-amino-1-carboxypentyl)iminodiacetic acid)succinyl] (nickel salt)). H-Ras(C118S, 1-181) (hereafter referred to as “Ras”) is linked to the SLB by coupling the Cys181 to the MCC-DOPE lipids through thiol-maleimide reaction, mimicking the native lipid-modification of Ras(*115*, *117*). The resulting membrane-linked Ras is stably bound and fully

functional(*39*, *44*, *115*, *117*). The cytoplasmic region of LAT, expressed along with an N-terminal His6 tag, is linked to the SLB through binding between its His tag and Ni-NTA lipid. (*118–120*). LAT is phosphorylated by a Src-family kinase protein, Hck, which is also tethered to the SLB. Although LAT is not the native substrate of Hck, Hck can fully phosphorylate LAT given sufficient time(*121*). The tethered proteins are laterally mobile, and their surface density on the membrane can be precisely measured by fluorescence correlation spectroscopy (FCS) (see Materials and Methods for detail). Typical densities used in the experiments described here are ~1500/μm^2 for Ras and ~500/μm^2 for LAT, both of which are comparable to physiological densities found in cells(*122–124*).

Time evolution of the Ras activation state (here defined as the fraction of activated Ras: RasGTP/(total Ras)) can be measured by quantitative fluorescence imaging of the binding of a Ras binding domain (RBD) sensor to RasGTP using total internal reflection fluorescence (TIRF) microscopy (*44*). Upon addition of SOS, Grb2, and GTP from the solution, robust Ras activation can be detected (Figure S3-1A). Kinetic traces of Ras activation by SOS^{Cat} exhibit sigmoidal shapes, confirming that the catalytic core of SOS exhibits a RasGTP-driven positive feedback as reported previously(*48*, *103*, *108*). In order to examine steady-state Ras activation under competitive activating and deactivating reactions, we introduce the catalytic domain of p120RasGAP (hereafter referred to as "RasGAP") from solution. RasGAP drives a simple, essentially bimolecular Ras deactivation reaction, with no evidence of feedback (Figure S3-1B). The combination of SOS and RasGAP establishes a continuously cycling Ras activation-deactivation competitive reaction (Figure S3-1C), which is drawn schematically in Figure 3-1.

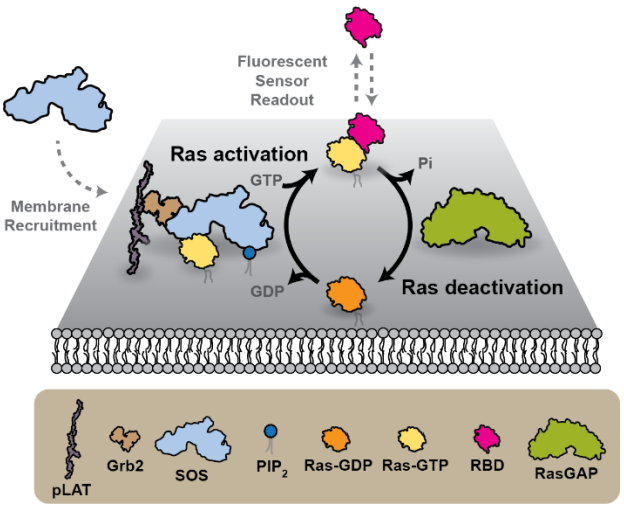

Fig. 3-1. Schematic of the reconstitution of a Ras activation-deactivation reaction. SOS can be recruited to the membrane by Grb2 mediated binding to pLAT and activate Ras. GAP from the solution can directly deactivate Ras. Ras activation can be detected by the binding of fluorescently labeled RBD.

3.3 Ras activity exhibits large fluctuations in microscopically confined reaction systems

Ras signaling reactions under cellular conditions are intrinsically confined on microscopic length scales by the physiological geometry of the cell. Additionally, SOS is estimated to be expressed at only 2000-7000 molecules per cell(*125*). In many cases, such as in T cell activation, signaling reactions are confined to localized signaling clusters on the membrane, further reducing the copy numbers of participating molecules(*126*, *127*). Spatial confinement and low molecular copy numbers lead to substantial stochastic variation that effectively changes the laws of chemistry within the cell(*128*), sometimes enhancing sensitivity(*24*, *107*), inducing bistability(*10*, *11*, *98*), or even changing the outcome of a competitive signaling reaction(*6*, *103*).

Here we adopt an experimental approach in which system size is a directly controllable parameter by using supported membrane microarrays(*39*, *43*, *44*) (Figure 3-2A). In this strategy, a supported membrane is formed on glass substrates prefabricated with arrays of metal lines. Lipids and membrane-bound components, such as Ras, diffuse freely within each confined corral but cannot cross the metal barriers, segregating each corral of membrane into an independent reaction system. Each corral, however, is in contact with an identical bulk solution phase and the metal barriers (only ~10 nm in height) have no interference with diffusion and flow within the solution phase(*129*). Prior to any reaction process, the initial state of the membrane components exhibits minimal variability across corrals (Figure S3-2). With the membrane microarray, we are able to simultaneously track thousands of competitive Ras activity reactions, all of which experience essentially identical reaction conditions, with spatial resolution down to ~1 μm and temporal resolution to 100 ms (Figure 3-2B).

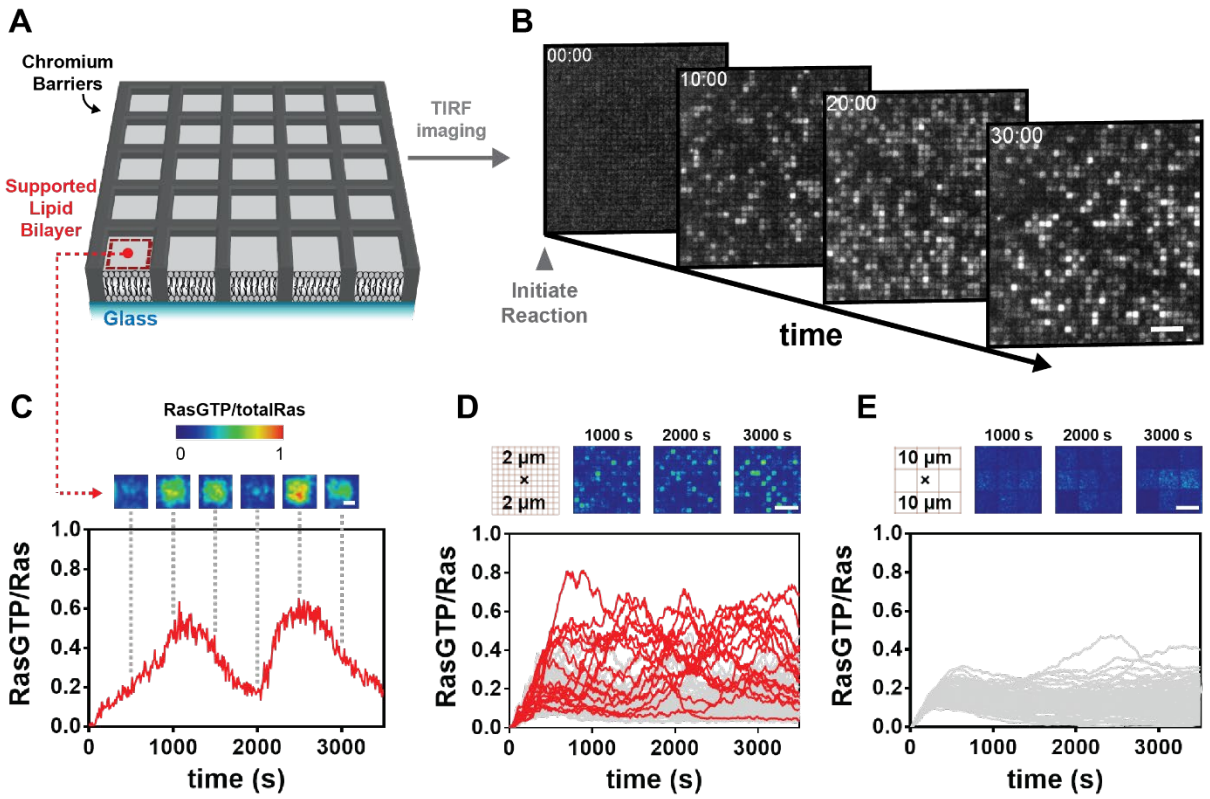

Fig. 3-2. Ras activation-deactivation reaction in membrane microarrays. (**A**) Schematic of the membrane microarray. (**B**) Time course images of Ras activation-deactivation reactions in membrane microarrays. Scale bar 10 μm. (**C**) Ras activation-deactivation reaction in a 2 μm × 2 μm corral. Scale bar 1 μm. (**D**) Reaction trajectories in 2 μm × 2 μm corrals (n = 400). Trajectories exceeded 0.5 RasGTP/Ras are labeled red. Scale bar 10 μm. (**E**) Reaction trajectories in 10 μm × 10 μm corrals (n = 100). Scale bar 10 μm.

Within smaller corral sizes (e.g. 2 μm × 2 μm), robust stochastic pulses of Ras activitation can be observed within individual corrals under steady-state conditions in the competitive activation reaction (Figure 3-2C). Such fluctuations can drive the Ras activation state far away from the mean and occur on the time scale of hundreds of seconds. An ensemble of 400 steady-state reaction traces from a 2 μm × 2 μm corral array is plotted in Figure 3-2D. Although the mean Ras activity (RasGTP/(total Ras)) is 0.079, many reaction traces (highlighted in red) cross the threshold of having more Ras-GTP than Ras-GDP (Ras activity = 0.50). This magnitude of stochastic variation cannot result from intrinsic stochasticity of individual Ras activation reactions. With thousands of Ras molecules in each corral, such intrinsic variation (which goes as $\sqrt{\text{number of molecules}}$) would be limited to a few percent(*130*). Instead, it is caused by individual SOS molecules entering the highly processive state, where the high catalytic output from a single SOS molecule can locally overwhelm the opposing GAP-catalyzed Ras deactivation reaction. This effect can be directly observed when simultaneously monitoring SOS binding to the membrane (with fluorescently labeled SOS constructs) and local Ras activation (Figure S3-3). We suggest such temporal spikes in Ras activity in the competitive reaction, here observed to last for hundreds of seconds, could trigger downstream signaling activity even while the average Ras activation level may be insufficient. In larger corrals, different behavior is observed. Reaction traces from an ensemble of 100 10μm x 10μm corrals are plotted in Figure 3-2E. Whereas the mean Ras activity (0.13) is similar to that observed in the 2μm x 2μm corrals, we now observe that none of the reaction traces exceed the Ras activity = 0.5 threshold at any point. In these larger sized corrals, the concentrated activity from individual SOS molecules is effectively diluted out and the individual reaction traces track much closer to the mean.

3.4 Ras activation-deactivation reaction exhibits a size-dependent bimodal response

Evidence for bimodal signaling behavior through Ras-MAPK pathway has been observed in a number of cellular systems(*87–94*). It has been proposed that RasGTP-driven positive feedback in SOS could lead to kinetic bistability in a competitive Ras activation-deactivation reaction system, and that this is the origin of cellular bimodal signaling behavior(*89*). However, bimodal Ras signaling in reconstituted sytems has not previously been reported. Here we test this hypothesis by directly examining the steady-state Ras activity behavior in competitive SOS-RasGAP reactions under a wide range of conditions and reaction system sizes. Unique features in these experiments that enable complex Ras activity behavior include: ***i***) Grb2-mediated recruitment of SOS^{FL} to activated receptor scaffold (pLAT); ***ii***) fluid movement of SOS on the membrane surface to processively activate many Ras molecules; and ***iii***) control of reaction size with the micropatterned supported membrane system.

We first performed Ras activation-deactivation reactions in SLB microarrays ranging from 1 μm × 1 μm up to 10 μm × 10 μm. The reaction systems were allowed to reach an apparent steady-state (after ~2 hr), at which point we examine the spectrum of corral-to-corral variability of the Ras activity state (Figure 3-3A). These reactions are run under conditions where the average Ras activity in macroscopic reactions is roughly 0.5 (upper images in Figure 3-3A). Probability distributions for the Ras activity state, derived from histograms of the observed activity on the corral arrays, are plotted below each image in Figure 3-3A. We observe the steady-state Ras activity to be bimodally distributed in the 1 μm × 1 μm and 2 μm × 2 μm corral arrays while becoming unimodal in larger size arrays. This scale dependence of the observed bimodality is not consistent with classic kinetic bistability. If there were a stable kinetic bistability underlying the bimodal signaling behavior, this would still be observed in the larger size corrals—appearing as spontaneously separating domains of Ras activity state (see, for example, the PIP_1/PIP_2 lipid patterns generated from kinetic bistability described in(*6*)). Instead, the observation of robust bimodality in small corrals and unimodality in larger corrals indicates a stochastic origin to the bimodal behavior in a system that is intrinsically monostable(*6*, *103*).

We next examine the robustness of the bimodal Ras activity response over a range of SOS concentrations, focuing on the 1 μm × 1 μm corral size. At the lowest solution concentration of SOS we examined (0.5 nM), the majority of the reaction corrals have essentially no Ras activation but a rare subset with distinctly high Ras activation states are clearly resolved (Figure 3-3B). As the SOS solution concentration is titrated from 0.5 nM up to 10 nM, we observed a change in the ratio of low and high Ras activity states (Figure 3-3B). The data for this titration of SOS against a fixed RasGAP concentration in a competitive reaction at steady state are summarized in Figure 3-3C. The system exhibits a bimodal response over the entire range of SOS concentrations. The high Ras activity state is at essentially the same activity level in all conditions, but is observed with higher frequency at higher SOS levels. The lower Ras activity state shifts to higher activity levels (but still firmly resolved from the high activity state) and lower frequency with increasing SOS concentration.

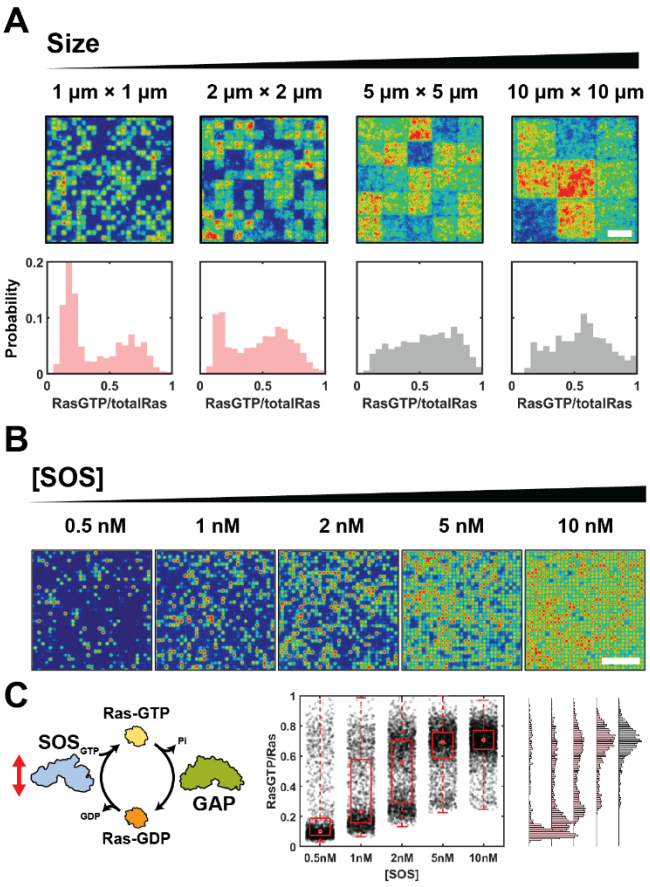

Fig. 3-3. Bimodal Ras activation in the Ras activation-deactivation reaction. (**A**) Distribution of Ras activation states in the Ras activation-deactivation reaction in corrals (n > 216). Conditions that are bimodal (based on the Hartigans' dip test ($p < 0.01$)) are plotted in red. Scale bar 5 μm. (**B**) Images of the Ras activation-deactivation reaction in 1 μm × 1 μm corral with varying SOS concentration. Scale bar 10 μm. (**C**) Distribution of Ras activation states in Figure 3B. Each dot represents a single corral. Right: Histogram of the Ras activation state distribution. Conditions that are bimodal are plotted in red.

3.5 The processivity of SOS is central to the bimodal response

We hypothesize that the observed bimodality in Ras activity state is driven by the extreme processivity of SOS. This hypothesis is partly motivated by the fact that bimodality is only observed in smaller reaction systems, which is suggestive of an underlying stochastic mechanism(*6*, *103*). SOS processivity is an intrinsic amplifier of stochasticity as it translates single molecular SOS activation events into bursts of hundreds of activated Ras molecules. We test this hypothesis by examining three truncated SOS constructs (Figure 3-4A): (i) SOS^{Cat}, only the catalytic domains with both the N- and C-terminal regulatory domains truncated, (ii) SOS^{catPR}, with the N-terminal regulatory domains truncated. and (iii) SOS^{HDPC}, with the C-terminal regulatory domains truncated (Figure 3-4A). All constructs, including SOS^{Cat}, have both allosteric and catalytic Ras binding sites and can exhibit RasGTP-driven positive feedback. The inclusion of the PR (SOS^{CatPR}) or the N-terminal regulatory domains (SOS^{HDPC}) domains adds autoinhibition as well as additional membrane binding interactions, which enhance SOS processivity. The C-terminal PR domain allows SOS^{CatPR} to bind to the membrane through Grb2 and phosphorylated LAT. The N-terminal HF, PH, and DH domains allow SOS^{HDPC} to bind to the membrane through lipids such as PIP_2.

The SOS constructs exhibit different levels of processive activity due to the different types of membrane association, with SOS^{FL} exhibiting the highest processivity(*49*, *50*). The truncated SOS constructs can also activate Ras in a non-processive manner, through transient collisions with the membrane. This activity is most prominent in SOS^{Cat}, which lacks all autoinhibition, and is progressively lower for both SOS^{CatPR} and SOS^{HDPC}, each of which have some autoinhibition. Transient activity is essentially unmeasurable in SOS^{FL}, due to its thorough autoinhibition. These different activity profiles for the SOS constructs can be resolved in an assay where SOS is allowed to catalyze Ras activation, in a one-way reaction without competing RasGAP, for a limited time (20 minutes) in SLB microarrays (Figure 3-4B). Results comparing initial and final Ras activity states for the four SOS constructs in 1μm x 1μm microarrays are illustrated in Figures 3-4C-F. The distribution of the Ras activation states sampled from thousands of corrals are plotted to the right of each representative image of the corral array. In the case of SOS^{Cat} (Figure 3-4C) , the Ras activity levels exhibit a Guassian distribution centered around a well-defined mean after 20 minutes of activation. There are no outlier high Ras activity corrals for SOS^{Cat}. This behavior corresponds with primarily transient activity, which uniformly distributes the Ras activation events among the corrals. For SOS^{CatPR} (Figure 3-4D) and SOS^{HDPC} (Figure 3-4E), there is a primarily Guassian peak around a moderate Ras activity level (from transient activity) with a number of high Ras activity corrals far outside this distribution, which correspond to occasional SOS molecules entering the processive state. SOS^{FL} exhibits the most extreme behavior, with a Gaussian peak after 20 minutes centered at essentially zero Ras activity and a number of highly activated corrals from processive SOS molecules (Figure 3-4F). These data confirm that the processive state is the only active state in native, SOS^{FL}(*44*, *50*, *131*).

In competitive reactions, we observe the processive activity of SOS is instrumental in overcoming the deactivating pressure from RasGAP to achieve high Ras activity states. Titrating SOS^{Cat} solution concentration in the presence of RasGAP on 1μm x 1μm corral arrays (as done previously with SOS^{FL}, see Figure 3-3) reveals a continuously shifting Ras activity level, with no evidence of bimodality at any SOS^{Cat} concentration (Figure 3-4G). Similar titrations with SOS^{CatPR} and SOS^{HDPC} reveal weak bimodality in some conditions (Figure 3-4H and 3-4I). Only SOS^{FL}, which exclusively activates Ras through the processive state, exhibits clear bimodality over the entire range of concentrations sampled (see Figure 3-3C).

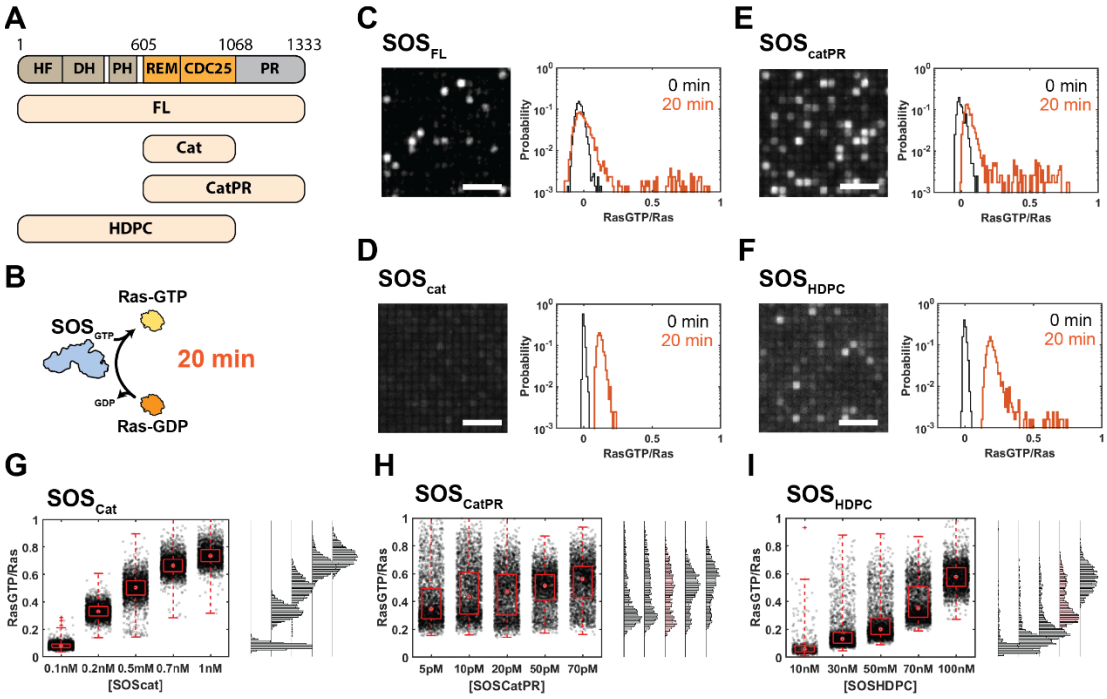

Figure 3-4 Reactions of truncations of SOS with varying processivity. (A) Domain organization of SOS. REM and CDC25 domain form the catalytic core. The catalytic core is flanked by N- and C-terminus regulatory domains. (B) Schematic of the time limited one-way reaction by SOS in 3-3C~3-3F. (C) SOS_{FL} reaction. Left: Image of the reaction at 20 min. Right: Distribution of Ras activation states. The black histogram is the distribution at 0 min. The orange histogram is the distribution at 20 min. Scale bar 5 µm. (D) SOS_{cat} reaction. (E) SOS_{catPR} reaction. (F) SOS_{HDPC} reaction. (G) Distribution of Ras activation states in SOS_{cat}-p120GAP competition reaction. (G) Distribution of Ras activation states in SOS_{catPR}-p120GAP competition reaction. (G) Distribution of Ras activation states in SOS_{HDPC}-p120GAP competition reaction. Conditions that are bimodal based on the Hartigans' dip test ($p < 0.01$) are labeled red.

3.6 Stochastic simulations confirm bimodality results from processivity

To further examine the connections between processivity and bimodality in Ras activation by SOS, we conducted a series of stochastic simulations. We used a simplified model that includes only the common processes among all SOS constructs. In this model (Figure 3-5A), SOS in solution (SOS_{sol}) can reversibly bind to either RasGDP or RasGTP through its allosteric site to become localized at the membrane; these membrane-associated species are labeled SOS:RasGDP and SOS:RasGTP, respectively. The binding affinity to the SOS allosteric site of RasGTP is stronger than RasGDP (16, 43) and this is reflected in the model. SOS:RasGDP or SOS:RasGTP catalyze the conversion of RasGDP to RasGTP with the same apparent rate constant, $k_{cat}^{(1)}$, which has been experimentally measured in single molecule membrane array experiments(*39*). Although $k_{cat}^{(1)}$ is independent of allosteric Ras nucleotide state, and therefore can make no contribution to positive feedback, this model still exhibits RasGTP-driven positive feedback through the differential binding of RasGTP vs. RasGDP at the SOS allosteric site. RasGAP catalyzes RasGTP to RasGDP reaction with simple bimolecular kinetics at a constant rate $k_{cat}^{(2)}$, experimentally determined from data shown in Figure S1B. Simulations were conducted using the Gillespie algorithm(44), and kinetic rate constants used in the simulation were derived from experimentally determined values (see Material and

Methods for detail). We first performed the stochastic simulation with slow $k_{off}^{(1)}$ and $k_{off}^{(2)}$, reflecting the experimental measurements, and which lead to processive Ras activation by SOS. Under this condition, the stochastic simulation is clearly reflective of the experimental results (Figure 3-5B), in which the Ras activation state is bimodally distributed only in small reaction systems. By contrast, when the same kinetic parameters and reaction scheme are modeled with deterministic rate equations and concentrations treated as continuous variables, the system has one unique steady-state solution—kinetic bistability is not achieved. Similarly, when the size of the reaction increases in the stochastic simulation, the Ras activation states become unimodally distributed around the deterministic solution.

We can use the stochastic simulation to isolate the effect of SOS processivity by increasing both k_{off} and k_{on} for Ras binding to the allosteric site, while preserving their ratio (K_D). Under these conditions, SOS dwells at the membrane so briefly that on average less than one Ras molecule is activated during an individual membrane binding event (no processivity). However, by preserving K_D , the total amount of membrane recruited SOS and overall rate of Ras activation is maintained. Modeling the system with deterministic rate equations yields identical results, irrespective of the degree of processivity of SOS. However, stochastic simulations yield drastically different behaviors. With processive SOS, the Ras activation state distribution responds to an increase in SOS concentration in a bimodal manner (Figure 3-5C). Conversely, when SOS is non-processive, the Ras activation state distribution responds to an increase in SOS concentration in a unimodal and graded manner that centers around the deterministic solution (Figure 3-5D). The non-processive SOS behavior closely matches the experimental results for SOS^{Cat} (Figure 3-3B).

Overall, these simulation results confirm SOS processivity is a key driver of the observed bimodal signaling response and that the system does not exhibit classic kinetic bistability. Broadly speaking, this type of behavior has been termed stochastic bistability(*10*, *11*, *107*), referring to the fact that bimodal behavior can emerge as a result of stochastic effects in systems that lack intrinsic kinetic bistability according to deterministic rate equations. There are different mechanisms by which stochastic effects can lead to bimodality. One well-known stochastic bistability mechanism is driven by positive feedback(*11*). In this scenario, one of the states will be close to 0 while the other state is near the deterministic steady-state solution. This can be readily reproduced by simulating the reaction in Figure 3-5A with strong positive feedback and weak processivity (K_D for RasGDP $>$ K_D for RasGTP, $k_{off} > k_{cat}$. See Material and Methods for detail) (Figure 3-5E). Compared with the deterministic solution, positive feedback-based stochastic bistability will stochastically deactivate the reaction, populating the 0 state.

Another type of stochastic bistability is driven by processivity (equivalent to burst amplitude in gene expression) (*132*). In the case of processivity-based stochastic bistability (simulating with K_D for RasGDP $= K_D$ for RasGTP, $k_{off} < k_{cat}$. See Material and Methods for detail) the deterministic solution lies between the two modes (Figure 3-5F). Our experimental observations that Ras activation state in small reaction sizes bifurcates into two modes with one higher and one lower than the Ras activation state in large reaction sizes is consistent with this later mechanism of stochastic bistability, driven by enzymatic processivity.

The subtle differences between these two mechanisms of stochastic bistability can become paramount in a signaling context. Inhibiting SOS has been an important topic in treatment of Ras signaling related

diseases(*76*, *109–112*). We simulated the effect of SOS inhibition on Ras signaling with the Ras signaling reaction exhibiting either a positive feedback-based or a processivity-based stochastic bistability (matching conditions in figure 3-5E and 3-5F with the addition of reversible inhibition of SOS catalysis, see Material and Methods for detail). Since in positive feedback-based stochastic bistability, both modes are equal or lower than the deterministic solution, the Ras activity of the overall population becomes inhibited relatively easily as predicted by the deterministic solution (Figure S3-4A). However, in processivity-based stochastic bistability, even at a drug concentration where deterministic kinetics predict successful lowering of Ras activation, Ras can still be stochastically activated in sufficient small reaction systems (Figure S3-4B). Overtime, essentially every Ras reaction will experience activation well above the activation threshold, even while the overall mean of the population is highly inhibited. This may provide a hint as to why effective SOS inhibition strategies to control Ras activity have been challenging to develop(*76*, *112*).

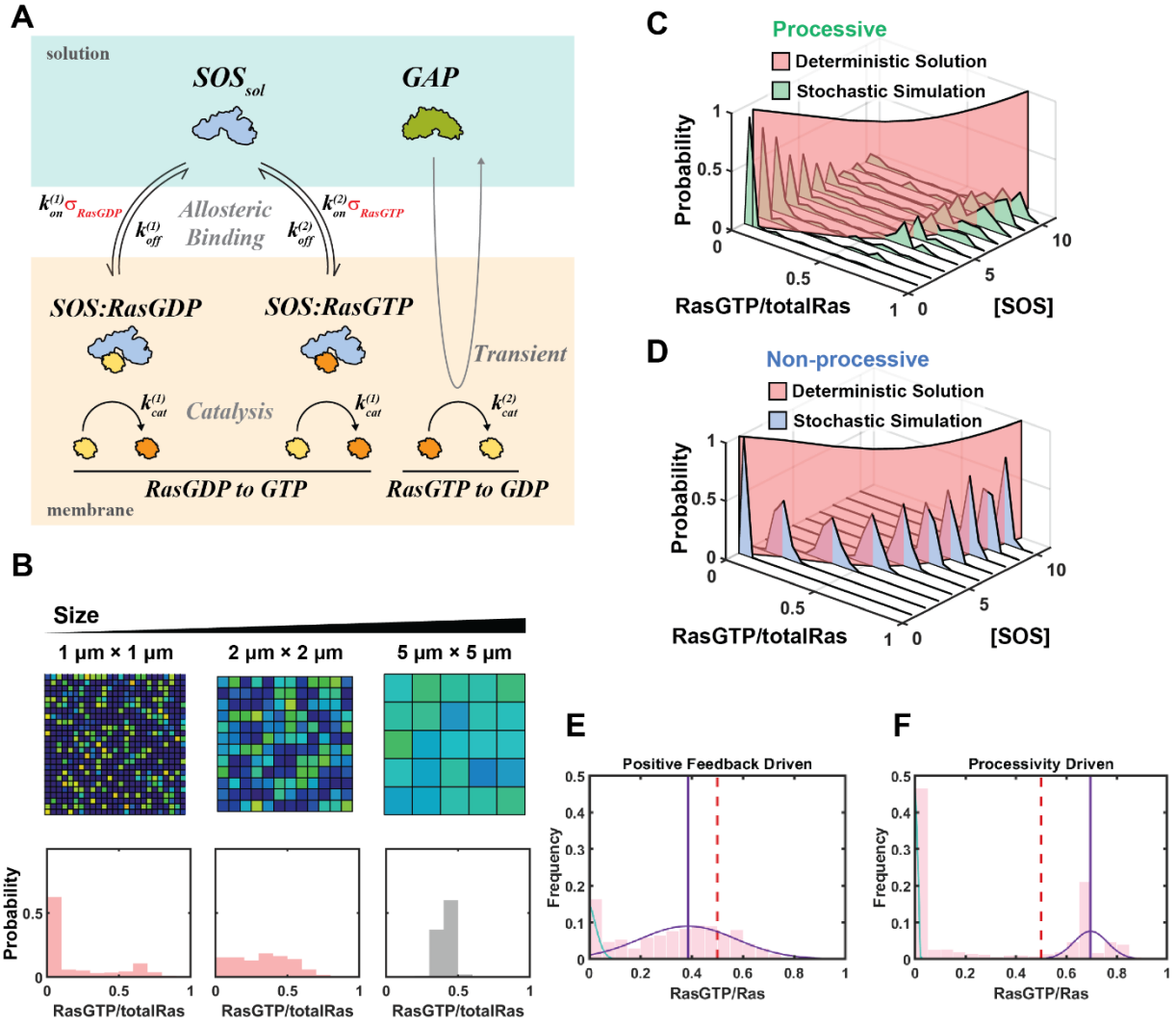

Fig. 5. Stochastic simulations of Ras activation-deactivation reactions. (**A**) Kinetic scheme for the stochastic kinetic modeling. (**B**) Simulated result of Ras activation-deactivation reaction in corrals (n>500). Conditions that are bimodal are plotted in red. (**C**) Simulated result of Ras activation-deactivation reaction with varying concentration of processive SOS and (**D**) non-processive SOS in 1 μm × 1 μm corrals. The red plane corresponds to the deterministic steady-state solution. (**E**) Simulation of Ras activation-deactivation reaction with weakly processive SOS that has strong positive feedback and (**F**) with processive SOS that has no positive feedback. The histogram is fitted to two gaussian distribution. The purple line shows the peak of the high mode. The red dashed line shows the deterministic steady-state solution

3.7 Control points for bimodal Ras activation

The bimodal Ras activation response is dependent on Ras density (Figure 3-6A). The observations of bimodal Ras activity responses described throughout this study were observed at relatively high Ras densities 1500~2000/μm^2. Such high densities of Ras have been reportedly observed in Ras clusters in cells (*122*, *123*), but are distinctly higher than the average Ras density in the plasma membrane (~400 molecules/μm^2)(*89*). At a Ras density 400 molecules/μm^2, we observe the steady-state Ras activity under a competitive SOS^{FL}-RasGAP reaction is no longer bimodal, and exhibits a graded response with changing SOS^{FL} solution concentration (Figure 3-6B). When the density of Ras is increased to ~1800 molecules/μm^2, the bimodal response is restored. These data indicate that increasing the local Ras density can alter the Ras signaling behavior from graded to switch-like. We speculate that this is due to the elevated encounter rate of SOS and Ras at high Ras density, which effectively speeds up the kinetic transition to processive activity (Figure 3-6A).

Bimodality in Ras activation is also controlled by LAT density (Figure 3-6A). The scaffold protein LAT forms a two-dimensional protein condensate with Grb2 and SOS on the membrane surface under the control of T cell receptor activation(*44*, *119*, *126*, *133*). A similar condensate has recently been reported with EGFR(*108*). Both the LAT and EGFR condensates control the ability of SOS to activate Ras, through a kinetic proofreading mechanism that taps into the slow autoinhibition release process in SOS. LAT (or EGFR) are effectively clustered in the condensed state and this facilitates multivalent engagement of SOS, which retains SOS at the membrane longer and facilitates autoinhibition release(*44*). We examined the effects of LAT clustering on membranes with low Ras density (~400 molecules/μm2), such that the reaction does not show bimodality under lower LAT density (~500 molecules/μm2) (Figure 3-6C). However, at a higher LAT density (~2500 molecules/μm2, comparable to the density of LAT in the LAT-Grb2-SOS protein condensate(*119*)) , the Ras activity state exhibits a bimodal response, despite the low Ras density. In this case, we speculate that the increased activation of SOS into its processive state by the high density of LAT is responsible for the observed bimodality.

Collectively, these results reveal that molecular clustering of LAT or Ras at the membrane can activate the switch-like response from bimodal Ras signaling. We note that this is only possible since the bimodality of Ras activity originates from a stochastic mechanism. If instead it had originated from classic kinetic bistability, the bimodality and switch-like activity would be robust and not sensitive to such subtle perturbations (Figure S5).

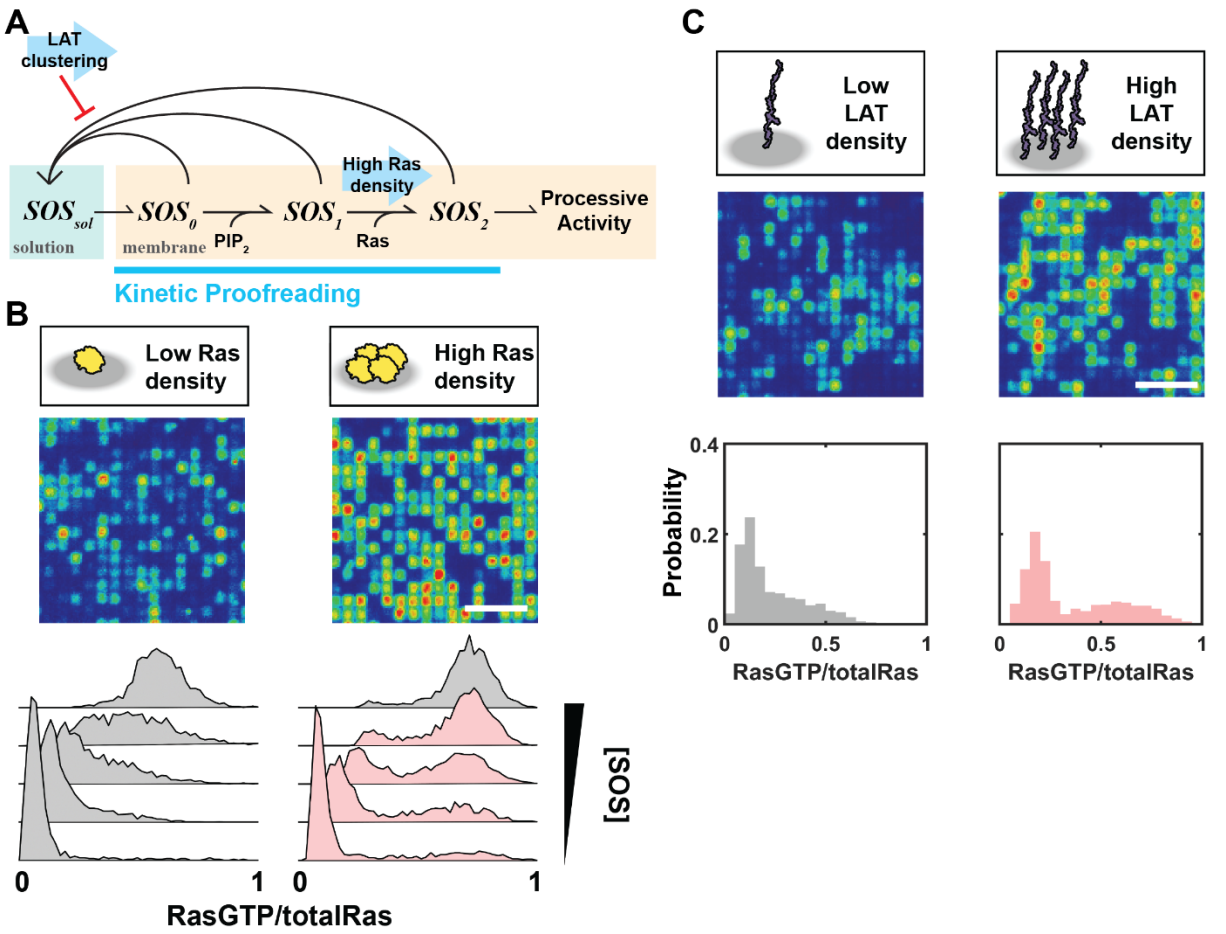

Fig. 3-6. Control points for bimodal Ras activation (**A**) Kinetic model for SOS activation. SOS needs to bind to the membrane, release autoinhibition, then bind to Ras at its allosteric site before it can become fully activated. These processes are competed by unbinding of SOS from the membrane. (**B**) Ras activation-deactivation reaction with low (~400 μm^2) and high (~2000 μm^2) Ras density. Scale bar 5 μm.(**C**) Ras activation-deactivation reaction with low (~500 μm^2) and high (~2500 μm^2) LAT density. Scale bar 5 μm.

3.8 Discussion

We have identified a stochastic mechanism that allows Ras signaling at the membrane to respond in a bimodal, switch-like manner. This is dependent on highly processive activity of SOS and is not the result of RasGTP-driven positive feedback and kinetic bistability. Given the low copy number of SOS(*125*), and the microscopic reaction scale in cells, a stochastic bimodal response should be readily achievable in Ras signaling in cells. Stochastic bistability can achieve similar behavior as kinetic bistability, but through a different physical mechanism.

A unique feature of the stochastic bistability mechanism is that this allows additional avenues for the switch-like response of Ras signaling to be regulated. We have demonstrated both Ras clustering and LAT clustering, as well as overall reaction size, can serve as control points to engage or disengage the bimodal signaling response. This is distinct from classic kinetic bistability, with two stable steady states, where the

switch-like response will always be present. While deterministic kinetic bistability is more robust over a wide range of conditions, stochastic bistability may be more accessible to regulatory control.

A deeper examination of the origin of stochastic bistability mechanisms clarifies the difference between two types of driving forces: positive feedback and processivity. Stochastic bistability driven by positive feedback will stochastically deactivate compared to a macroscopic reaction. On the other hand, in SOS mediated Ras signaling, the stochastic bistability is driven by processivity and can stochastically activate Ras signaling compared to the macroscopic reaction. This feature may allow Ras signaling to be activated even under a globally inhibiting background of high GAP activity. However, by the same logic, this mechanism may also result in resistance to attempts to inhibit Ras with drugs.

Despite numerous simulation and theoretical studies on stochastic bistability(*10*, *11*, *107*, *134*, *135*), there have been very few experimental reports that describe stochastic bistability in real biological signaling systems(*132*, *136*). . In part, this is due to the difficulties in analyzing biological reactions in a controlled microscopic environment. The present study describes a systematic approach to studying stochastic effects in membrane signaling reactions. Many signaling proteins exhibit complex regulation at the membrane, including phospholipase C-γ(*137*), phosphoinositide 3-kinases(*138*), N-WASP(*139*), and Vav(*140*). We speculate that many of the complex molecular features of these signaling proteins could induce bimodal responses in a cellular reaction environment even when classic kinetic bistability can be ruled out.

3.9 Supplemental figures

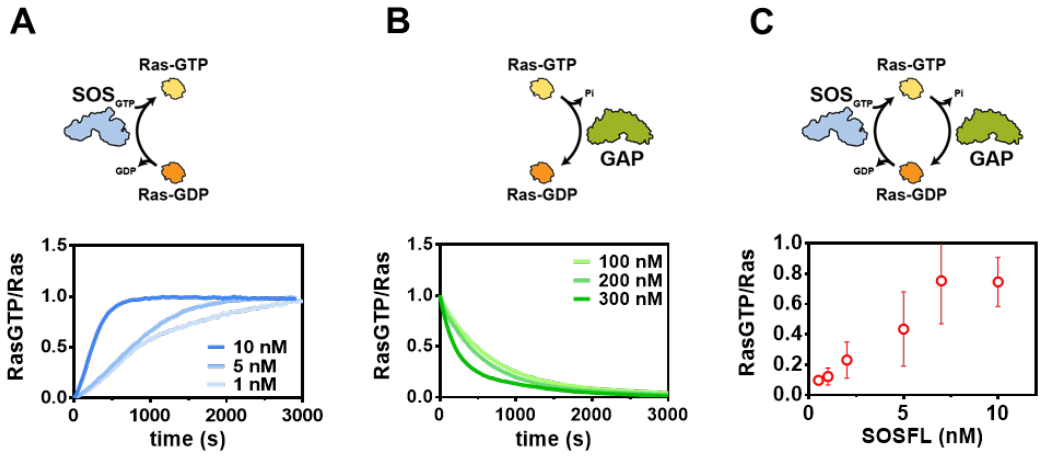

Fig S3-1. Reconstituted Ras activation and deactivation reaction. (A) Ras-GDP to Ras-GTP nucleotide reaction catalyzed by SOS (B) Ras-GDP to Ras-GTP nucleotide reaction catalyzed by RasGAP. (C) Steady state response of Ras activation-deactivation reaction with 200 nM RasGAP and varying concentration of SOS.

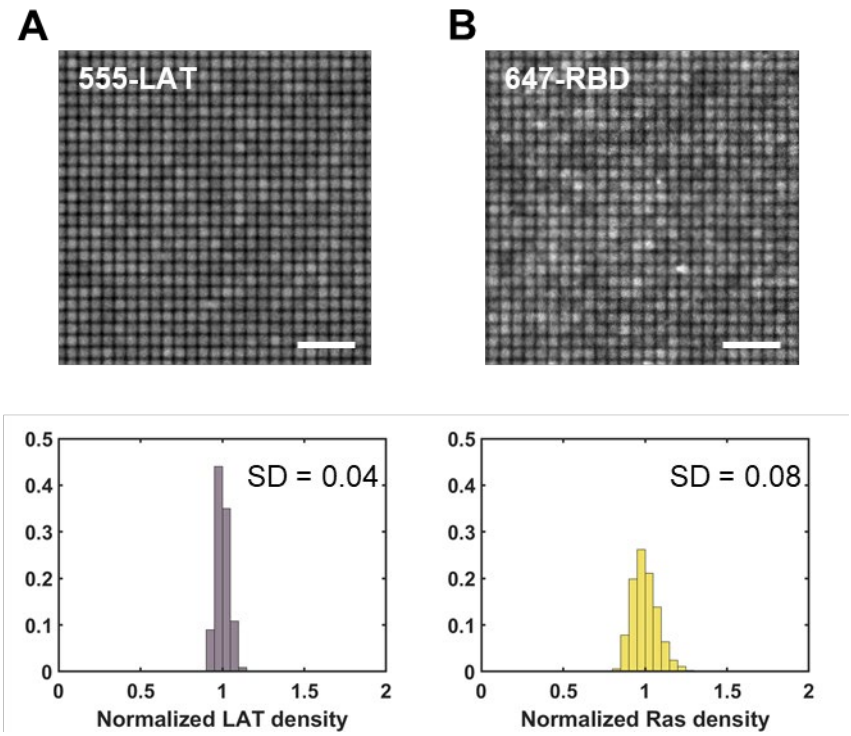

Fig S3-2. Density variation analysis in the micropatterned supported lipid bilayer. (A) Intensity distribution of 555-LAT across corrals (n>1000). Scale bar 5 μm. (B) Intensity distribution of Ras (measured by 647-RBD after Ras was fully activated by SOS to Ras-GTP) across corrals (n>1000). Scale bar 5 μm.

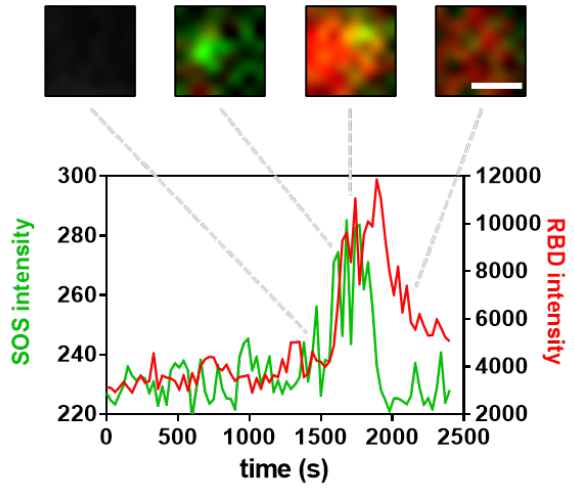

Fig S3-3 Representative example of a burst in Ras activation caused by a single molecule SOS.. The images and plot are from a single 1 μm × 1 μm corral in a Ras activation-deactivation reaction performed with Alexa-555 labeled SOS. The step increase in the SOS intensity indicates the recruitment of a single SOS molecule to the membrane, as shown in the images above. This is followed by a rapid increase in RBD intensity, indicative of a burst in Ras activation. After SOS detached form the membrane, the Ras activation slowly decreases from the RasGAP activity.

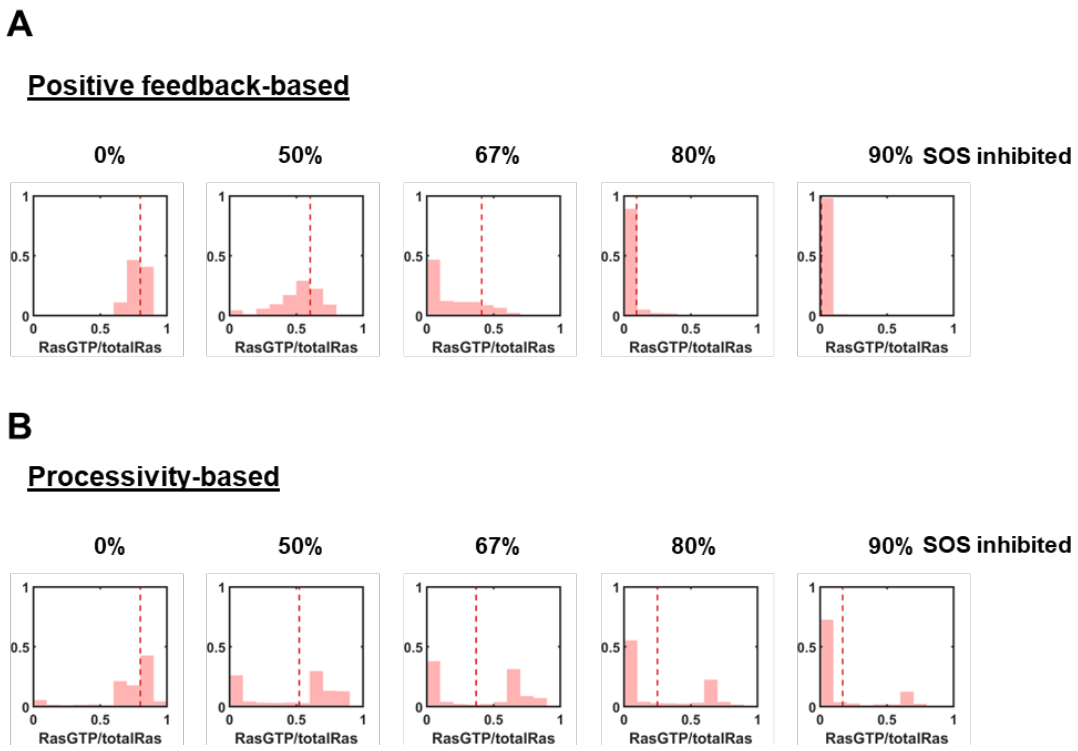

Fig S3-4 Simulation of SOS inhibition. (A) Positive feedback-based stochastic bistability scenario with SOS inhibition. Distribution of Ras activation state with varying amount of SOS inhibitor in the stochastic simulation (red histogram) plotted with the deterministic steady state solution (dotted red line). At no inhibitor (0% SOS inhibited), Ras activation is 0.7 according to the deterministic steady state solution. At 90% SOS inhibited, both the stochastic simulation and deterministic steady state solution indicates successful inhibition of Ras activation. (B) Processivity-based stochastic bistability scenario with SOS inhibition. Distribution of Ras activation state with varying amount of SOS inhibitor in the stochastic simulation (red histogram) plotted with the deterministic steady state solution (dotted red line). At no inhibitor (0% SOS inhibited), Ras activation is 0.7 according to the deterministic steady state solution. At 90% SOS inhibited, while the deterministic steady state solution suggested successful inhibition (Ras activation lowered to 0.169) the stochastic simulation showed a fraction of the reactions still exhibits strong activation way above the mean.

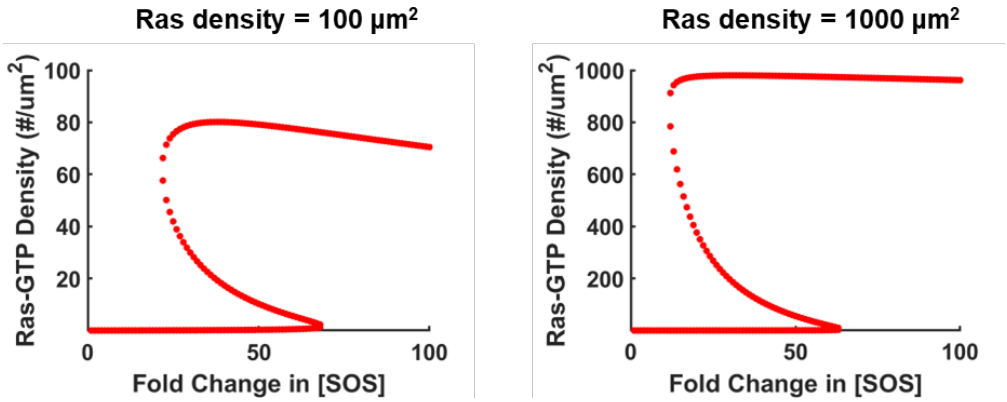

Fig S5 Ras activation reaction with kinetic bistability at varying Ras densities. Using kinetic parameters that leads to kinetic bistability, the deterministic steady state solution can be solved at reaction conditions with either high or low Ras densities. Left: Ras density at 100 μm2. Right: Ras density at 1000 μm2. The bistable response is robust across different Ras densities.

Chapter 4

SHAPE-RESPONSIVE ENZYMATIC REACTION ESTABLISHES POLARITY ON THE CELLULAR MEMBRANE

Polarization, by asymmetric distribution of signaling molecules on the membrane, is a fundamental aspect of essentially all cellular life. Pattern-forming instabilities in reaction-diffusion systems are conventionally used to provide a conceptual framework for understanding such phenomena. However, the physical requirements to establish stable pattern formations in continuum reaction-diffusion systems are highly restrictive, drawing into question the extent to which such mechanisms actually control real-world systems. Here we demonstrate an intrinsically stochastic reaction mechanism that can drive polarization with near deterministic outcome by coupling to the shape of the cellular membrane. This alternative mechanism, which has no analog in continuum reaction-diffusion systems, has much less restrictive requirements to induce polarization. We experimentally realize spontaneous reaction polarization in two ubiquitous competitive enzymatic systems: phosphatidylinositol phosphate (PIP) lipid phosphorylation-dephosphorylation and Ras activation-deactivation cycles. The observed polarization in these systems is not *de novo*, but rather is the result of coupling between intrinsic stochastic reaction fluctuations and the shape of the confining cell membrane. As such, the arising polarity is consistently aligned with cellular shape features in ways that conventional continuum reaction-diffusion descriptions of biological pattern formation do not predict. Through a series of mesoscopic experiments in shape-confined membrane systems and corresponding stochastic kinetic reaction-diffusion modeling, we elucidate the underlying physical mechanism as well as key control parameters. From the results emerges a surprisingly simple-to-achieve mechanism that drives robustly consistent symmetry breaking and polarization behavior. Many known biological signaling systems achieve the minimum requirements we identified, suggesting this mechanism may be widespread in biology.

4.1 Introduction

The establishment of cell polarity is necessary for critical cellular functions, such as cell migration(*141–143*), division(*144*), transfer of information(*145*), and immune response(*146*). Such spontaneous emergence of spatial patterns of molecules in the liquid milieu of a living cell is a hallmark of life. By contrast, reconstituted biochemical reactions in a macroscopic test-tube format typically exhibit spatially homogeneous behavior, rigorously following the basic laws of chemical reaction-diffusion systems. In a landmark paper, Alan Turing pointed how a wide range of spontaneous patterns can emerge in the mathematical solutions to basic continuum reaction-diffusion equations when certain requirements are met(*13*). Now referred to as Turing instabilities, and resultant Turing patterns, this type of mathematical interpretation has formed the foundation for a vast array of largely theoretical studies on biological pattern forming processes. Natural systems like fish skin pigmentation(*147*), bird feather buds(*148*), mouse hair follicles(*149*), and digit patterning(*150*, *151*) all exhibit some characteristics that resemble Turing patterns, but we do not have *in vitro* experiments that can certify their mechanism. Experimentally, only a handful of (non-biological) chemical systems have been reconstituted that demonstrably meet the requirements for a Turing instability(*152–154*). Reconstitution of pattern-forming biological systems has proven almost unobtainable, with the spectacular Min oscillator offering a rare exception(*155*). Physical realization of the mathematical conditions for a Turing instability, such as the significant difference in molecular diffusivity between competing species, are hard to reach in reality. For these reasons, it is still not yet possible to conclude that cell polarity and other biological patterns are actually formed through the Turing pattern mechanism.

Theoretical studies of biological pattern formation have disproportionately emphasized a continuum description of reaction-diffusion processes. This continuum approach, in which concentration is treated as a continuously varying parameter, smooths over the fact that molecules are intrinsically discrete and cannot capture behaviors resulting from stochastic variation. Several theoretical works have shown how stochasticity can broaden the pattern-permitting parameter space(*156–159*) or even enhance the speed or accuracy of the predicted pattern formation(*160*, *161*). Recent experimental studies have also identified an intrinsically stochastic mechanism by which enzymatic reaction rates can become scale dependent(*103*). We posited that this stochastic scale-sensing mechanism might be an enabler of pattern forming behavior, in a reaction shape-responsive manner, under conditions where Turing patterns cannot form.

Here, we examine two biologically distinct competitive enzymatic reaction cycles operating on the membrane surface that meet the basic conditions for stochastic scale sensitivity. In both cases, a membrane substrate is toggled between two states by a pair of enzymes that reside in the solution phase. One system consists of a variety of lipid kinases and phosphatases driving interconversion of phosphatidylinositol phosphate (PIP) lipids between the mono- and di-phosphorylated states (PIP_1 and PIP_2)(*6*). The other system consists of the guanine nucleotide exchange factor (GEF) SOS driving nucleotide exchange to convert RasGDP to RasGTP working against the GTPase activating protein (GAP), which facilitates hydrolysis of RasGTP back to RasGDP. Both of these reaction systems are of central importance in many biological signaling mechanisms and they both also exhibit positive feedback in a manner that enables the stochastic scale sensing mechanism(*103*).

Experiments reveal that both systems spontaneously polarize in response to specific types of spatial confinement in a patterned supported membrane, while still exhibiting exclusively homogeneous behavior on unconfined membranes. Neither system achieves a Turing instability nor does either exhibit intrinsic

kinetic bistability. The observed behavior is dependent on spatial confinement of the reactions and the two-dimensional shape of the membrane confinement determines the polarity direction with near deterministic outcome—qualitatively differing from the behaviors of other known pattern-forming mechanisms(*13*, *16*). We further demonstrate that the direction of polarity can be switched by engineering positive feedback on the enzymes. Stochastic kinetic modeling of reaction-diffusion for minimal reaction mechanisms reveals how the stochastic binding and unbinding of enzymes to the membrane explicitly enables the observed behavior. Experiments are performed under geometrical confinement patterns resembling a variety of natural cellular shapes and molecular densities are also near physiological levels. Thus spontaneous polarization we observe is thus likely to exist under natural physiological conditions and may be a contributing factor in known biological pattern forming processes in living cells.

4.2 PIP Phosphatase and Kinase competition on shape-controlled supported membrane shows near-deterministic polarization

A previously reported lipid kinase-phosphatase competition system had briefly demonstrated that it could polarize on membranes in confinement, but the mechanism was not uncovered(*6*). Therefore, we decided to systematically study the system's polarization under membrane confinement and reveal its core principles (Fig. 1a). In the system, the catalytic domains of kinase phosphatidylinositol-4-phosphate 5-kinase (PIP5K) and the phosphatase Lowe oculocerebrorenal syndrome protein (OCRL) act on their substrate phosphatidylinositol phosphate (PIP) lipid on a supported lipid bilayer. OCRL and PIP5K oppose each other's reaction: OCRL converts phosphatidylinositol-4,5-phosphate ($PI(4,5)P_2$) to phosphatidylinositol-4- phosphate (PI4P), and PIP5K converts PI4P to $PI(4,5)P_2$.

PIP5K binds to the membrane via its $PI(4,5)P_2$-binding sites, which is independent of its catalytic site, whereas OCRL does not bind to the membrane. Thus, PIP5K converts PI4P to $PI(4,5)P_2$ mainly in its membrane-bound state, whereas OCRL converts $PI(4,5)P_2$ to PI4P with transient contact to the membrane from the solution. The dependence of PIP5K membrane binding on $PI(4,5)P_2$ results in positive feedback, a necessary feature for pattern-forming reactions(*162*).

In order to study the two-dimensional membrane shape's effect on polarization under the competition reaction, we created two-dimensional membranes of defined shapes and sizes by using a micro-patterned chromium layer on glass(*43*). Supported lipid bilayer (SLB) forms only on top of exposed glass laterally surrounded by the thin chromium. The metal's low (~9 nm) height does not affect the movement of molecules introduced to the system from the solution. Lipids and lipid-bound proteins freely diffuse inside the enclosed region, but the movement lies inside the boundary(*39*, *43*). Multiple membranes of different shapes interact with the shared bulk solution above, allowing us to observe an ensemble of reactions. We tracked the distribution of PI4P and $PI(4,5)P_2$ lipids by a total internal reflection fluorescence (TIRF) microscope using previously developed fluorescent sensors(*6*). Defects in Rab recruitment protein A (DrrA) labeled with Cy3 (DrrA-Cy3), and pleckstrin homology (PH) domain of phospholipase C δ (PLCδ) labeled with Alexa Fluor 488 (PLCδ-Alexa488) provide high time and spatial resolution in imaging the distribution of PIP lipids.

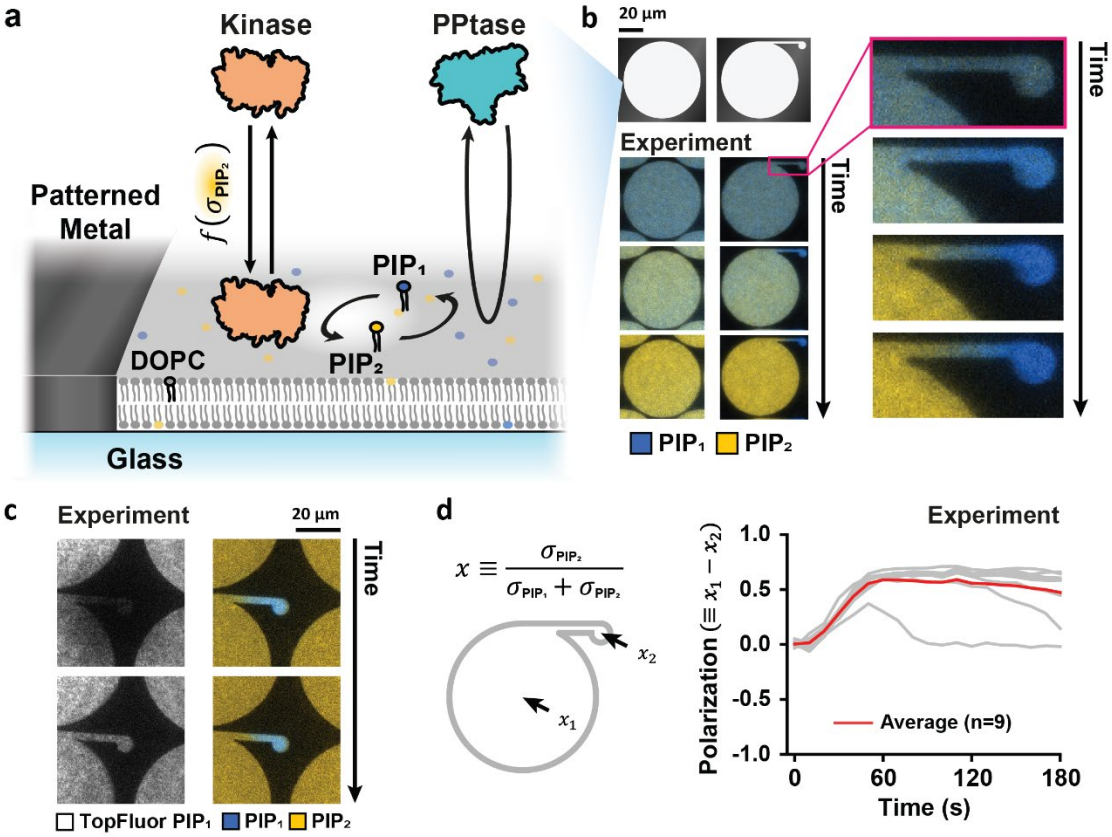

Figure 4-1 PIP kinase-phosphatase competition reaction polarizes on pattered supported lipid bilayer. (a) Schematic of the PIP kinase-phosphatase competition reaction reconstituted on a patterned supported lipid bilayer. Kinase bind to the membrane in a $PI(4,5)P_2$ dependent manner and can catalyze PI4P phosphorylation, while phosphatase catalyze $PI(4,5)P_2$ dephosphorylation directly from the solution. Patterned metal defines the shape of the supported lipid bilayer. (b) Time sequence images of PIP kinase-phosphatase competition reaction in a circular membrane or a circular membrane with protrusion. Top left: The shape of the membrane. Bottom left: Time sequence images with 30 sec intervals. Right: Enlarged view with 30 sec intervals. (c) FRAP experiment of TopFlour- PI4P. The label is on the lipid tail and represents all PIP lipids in the experiment. Time interval 40 sec. (d) Left: Definition of reaction coordinate and polarization. Right: Experimental polarization time trace of circular membrane with protrusion (n=9).

First, we focused on the effect of cell protrusion because it is a fundamental process in numerous cellular behaviors including cell migration and invasion(*163*). Two differently shaped membranes were constructed, one mimicking a cell without a protrusion and the other mimicking a cell with a protrusion (Fig. 2b). The composition of all the membranes were identical, 96 mol% 1,2-dioleoyl-sn-glycero-3-phosphocholine (DOPC), 2 mol% PI4P, and 2 mol% $PI(4,5)P_2$. The distribution of the PI4P and $PI(4,5)P_2$ are homogeneous initially (Fig. 2b). However, when we introduced phosphatase, kinase, and ATP, the lipid composition changed over time. Notably, by adjusting the concentration of the enzymes, contrasting behaviors were observed under the same bulk solution. In circular membranes (60 μm in diameter), both PI4P and $PI(4,5)P_2$ levels changed without detectable spatial inhomogeneity (Fig. 1b). However, in circles with a protrusion, the membranes polarized into PI4P-rich and $PI(4,5)P_2$-rich regions, creating distinct lipid composition between the protrusion tip and the main body (Fig. 1b). The polarization was not a result of lipid or protein phase separation, since fluorescence recovery after photobleaching (FRAP) experiment verified the fluidity of the lipids (Fig. 1c). The direction of the polarization axis was highly consistent, with the small protrusion in PI4P-dominant state and the larger circular body in $PI(4,5)P_2$-dominant state, and never observed in the

opposite direction. To quantify this, we defined the reaction coordinate, $x \equiv \sigma_{PI4P} / (\sigma_{PI4P} + \sigma_{PI(4,5)P_2})$, where σ_{PI4P} and $\sigma_{PI(4,5)P_2}$ represents the surface density of PI4P and $\sigma_{PI(4,5)P_2}$ represents the surface density of PI(4,5)P_2. Tracking the x-value at the center of the main body and the protrusion tip as x_1 and x_2, we defined the difference $x_1 - x_2$ as the polarization. The polarization was consistent among multiple membranes and lasts for minutes (Fig. 1d).

4.3 Stochasticity enables polarization

Stochasticity has been shown to have strong influence on the kinase-phosphates competition reaction(*6*, *103*). Therefore, we constructed a simplified two-dimensional reaction-diffusion model to test whether stochastic enzyme binding is important for the observed polarization in our experiments (Fig. 4-2a). In our model, the kinase stochastically binds to and unbinds from the membrane following the kinetic rates k_1^+ and k_{-1}^+, whereas membrane-bound kinases turn PI4P into PI(4,5)P_2 following Michaelis-Menten kinetics with kinetic parameters k_{cat}^+ and K_M^+. The phosphatase, without membrane-binding, turns PI(4,5)P_2 into PI4P with k_{cat}^- and K_M^- (Fig. 4-2a). Both the PIP lipids and membrane-bound enzymes diffuse on the membrane, with diffusion coefficients D_{pip} and D_{enz} (for details, see Materials and Methods). We first simulated the reaction on a circular membrane using simulation parameters that predict a single stable steady-state (Fig. 4-2b). The PIP composition was homogeneous throughout the simulation, which reached and maintained a steady-state. However, when simulating the membrane in a circle with a protrusion, the protrusion tip achieved a high level of PI4P, whereas the main body reached a high level of PI(4,5)P_2, similar to our experiment (Fig. 4-2c). The polarization was maintained against the homogenizing effect of lipid and protein's lateral diffusion. Tracking the time-dependent evolution of the reaction coordinate x at different position during the reaction showed that while x_1 reached the predicted steady-state, x_2 moved away from the steady-state and becomes PI4P enriched (Fig. 4-2d). The discrepancy in reaction kinetics between the main body and the protrusion originates from the difference in their effective area. Due to the larger area of the main body, the probability to recruit a kinase somewhere on its membrane is much higher. Thus recruited kinase increases the local PI(4,5)P_2 density, increasing the probability of subsequent kinase binding (positive feedback). Collectively the kinases overcomes the phosphatase activity, dominating the main body with PI(4,5)P_2. In contrast, the protrusion presents a much smaller area, and has a lower chance to recruit a kinase before the phosphatase dephosphorylates most of the PI(4,5)P_2 into PI4P and diminishes kinase recruitment probability. Stochasticity is crucial in the process and polarization disappeared when the simulation was run on the geometry that is ten times bigger (Fig. 4-2e).

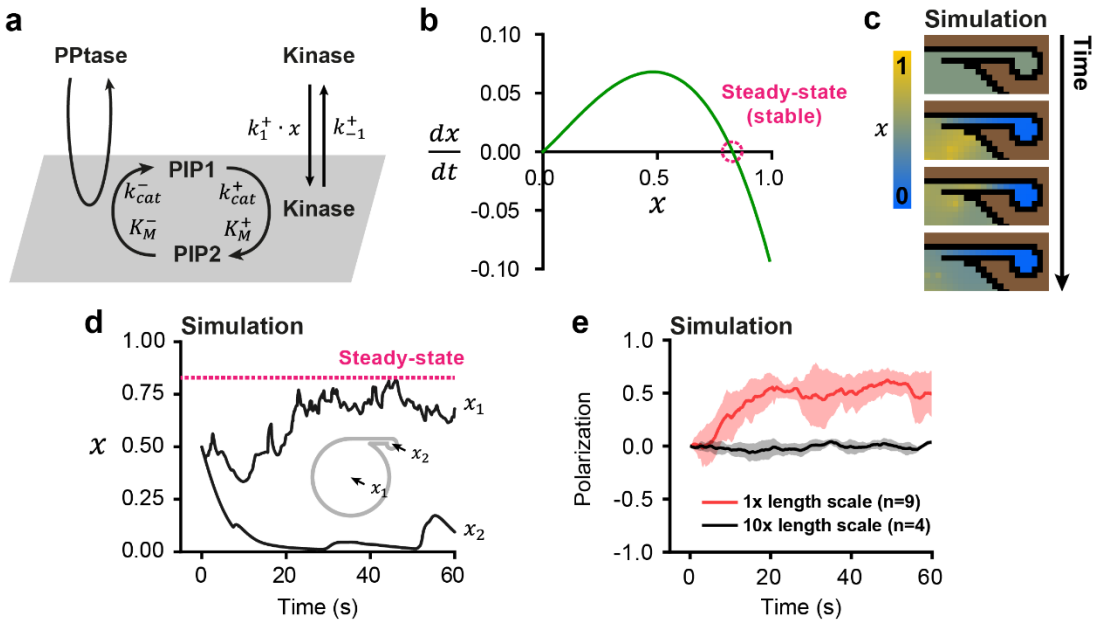

Figure 4-2 Stochastic simulation of PIP kinase-Phosphatase polarization reaction. (a) Schematic of the kinetic processes that are modeled in the two-dimensional reaction-diffusion stochastic simulation. (b) Reaction flux to reaction coordinate plot for the simulated parameters reveals a single stable steady-state. (c) Simulated PIP kinase-phosphatase polarization reaction in a circular membrane with protrusion. (d) Representative reaction coordinate time trace of the simulation. (e) Simulated polarization time trace of circular membrane with protrusion. Simulations in 1× length scale are plotted in red and simulations in 10 × length scale are plotted in black. The shaded area is the standard deviation.

4.4 Engineering enzyme kinetics reverses the polarization

Previously, it has been shown that engineering membrane enzymes with positive feedbacks would enable the enzymes to become size-sensing(*103*). The phosphatase OCRL can be fused with the PI4P binding domain (DrrA) to enable binding to the membrane via its product PI4P, establishing positive feedback. It has been shown that by engineering positive feedback to OCRL, the direction of size sensing in the PIP5K and DrrA-OCRL competition reaction can be reversed in relation to PIP5K and OCRL competition reaction(*6*, *103*). We thus hypothesized that by replacing OCRL with DrrA-OCRL in PIP competition reaction, the direction of polarization could be reversed. In PIP competition reaction using DrrA-OCRL, both the phosphatase and the kinase exhibits positive feedback and catalyze PIP lipids mostly in membrane-bound states with negligible contributions from direct catalysis from the solution (Fig. 4-3a).

Strikingly, DrrA-OCRL and PIP5K polarized the membrane in the direction opposite to OCRL and PIP5K pair (Fig. 4-3b). Our simulation reproduced this behavior when configuring both phosphatase and kinase to convert between their solution and membrane-bound states, adhering to the law of mass action. The phosphatase converts with the kinetic rates $\{k_1^-, k_{-1}^-\}$ and the kinase with $\{k_1^+, k_{-1}^+\}$. When simulated on the membrane ten times bigger, the membrane did not polarize (Fig. 4-3c).

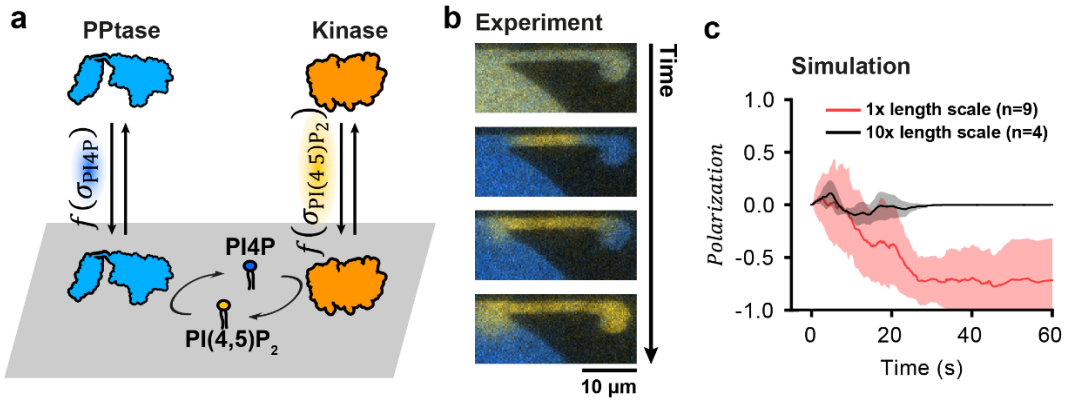

Figure 4-3 Stochastic simulation of PIP kinase-Phosphatase polarization reaction. (a) Schematic of the kinetic processes of the PIP5K and DrrA-OCRL competition reaction. (b) Enlarged time sequence images of PIP5K and DrrA-OCRL competition reaction in a circular membrane with protrusion with 30 sec intervals. (c) Simulated polarization time trace of PIP5K and DrrA-OCRL competition reaction in a circular membrane with protrusion. Simulations in 1× length scale are plotted in red and simulations in 10 × length scale are plotted in black. The shaded area is the standard deviation.

4.5 The effect of cellular geometries on the polarization

To further address the relevance of the observed phenomena in cellular contexts, we created supported membranes of cell-like shapes using microfabrication on glass. Shapes of an actual cell presenting a large number of filopodia, an actual brain cell, and a representation of a migrating cell were patterned (Fig. 4-4). Remarkably, all these two-dimensional shapes had dramatic effects on the membrane polarization under the competition reaction. For the filopodia-rich cell-shaped membranes, under OCRL and PIP5K competition, the main body enriched in $PI(4,5)P_2$, and the filopodia region enriched in PI4P. When DrrA-OCRL and PIP5K were introduced, the main body enriched in PI4P, and the filopodia region enriched in $PI(4,5)P_2$.

The brain cell-shaped membranes enriched the dendritic region in PI4P and the cell body in $PI(4,5)P_2$ under OCRL and PIP5K competition, but enriched the dendritic region in $PI(4,5)P_2$ and the cell body in PI4P under DrrA-OCRL and PIP5K. Lastly, the migrating cell-shaped membranes enriched the leading edge in $PI(4,5)P_2$ and the trailing edge in PI4P under OCRL and PIP5K competition, but enriched the leading edge in PI4P and the trailing edge in $PI(4,5)P_2$ under DrrA-OCRL and PIP5K (Fig. 4-4a and 4-4b). The experiments showed that the two-dimensional shape of the membrane mimicking commonly observed cell shapes is enough to produce dramatic polarizations under the kinase-phosphatase competition. The polarization patterns were reproduced by our simulations using the same kinetic parameters used to simulate the reactions on the membranes of previously simulated shapes (circle, and circle with a protrusion) (Fig. 4-4c and 4-4d).

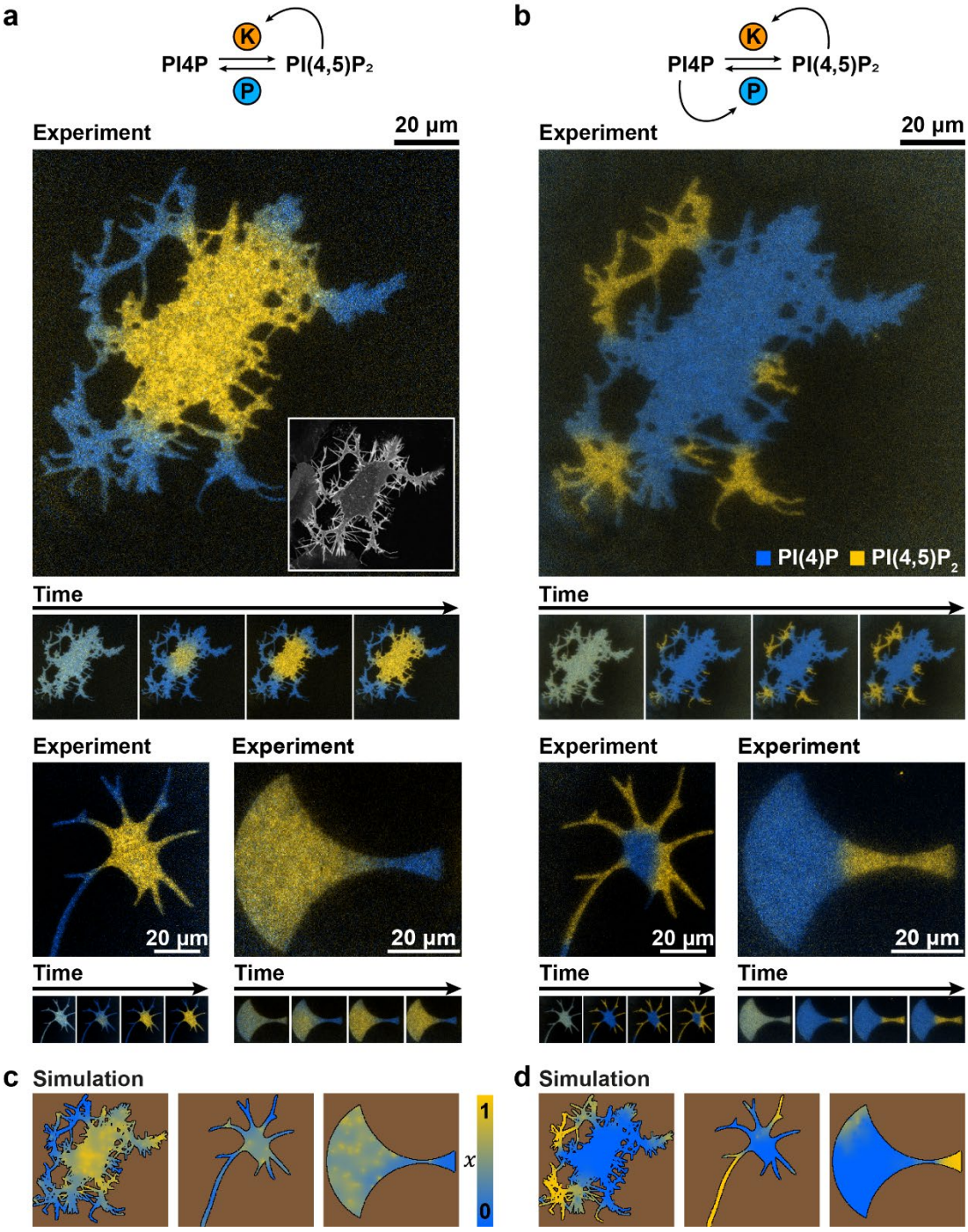

Figure 4-4 Polarization of PIP kinase-Phosphatase reaction in cell-like shapes. (a) Polarization of OCRL and PIP5K competition reaction in cell-like shapes. Time interval 40 sec. (b) Polarization of DrrA-OCRL and PIP5K competition reaction in cell-like shapes. Time interval 40 sec. (c) Simulation of OCRL and PIP5K competition reaction in cell-like shapes. (d) Simulation of DrrA-OCRL and PIP5K competition reaction in cell-like shapes.

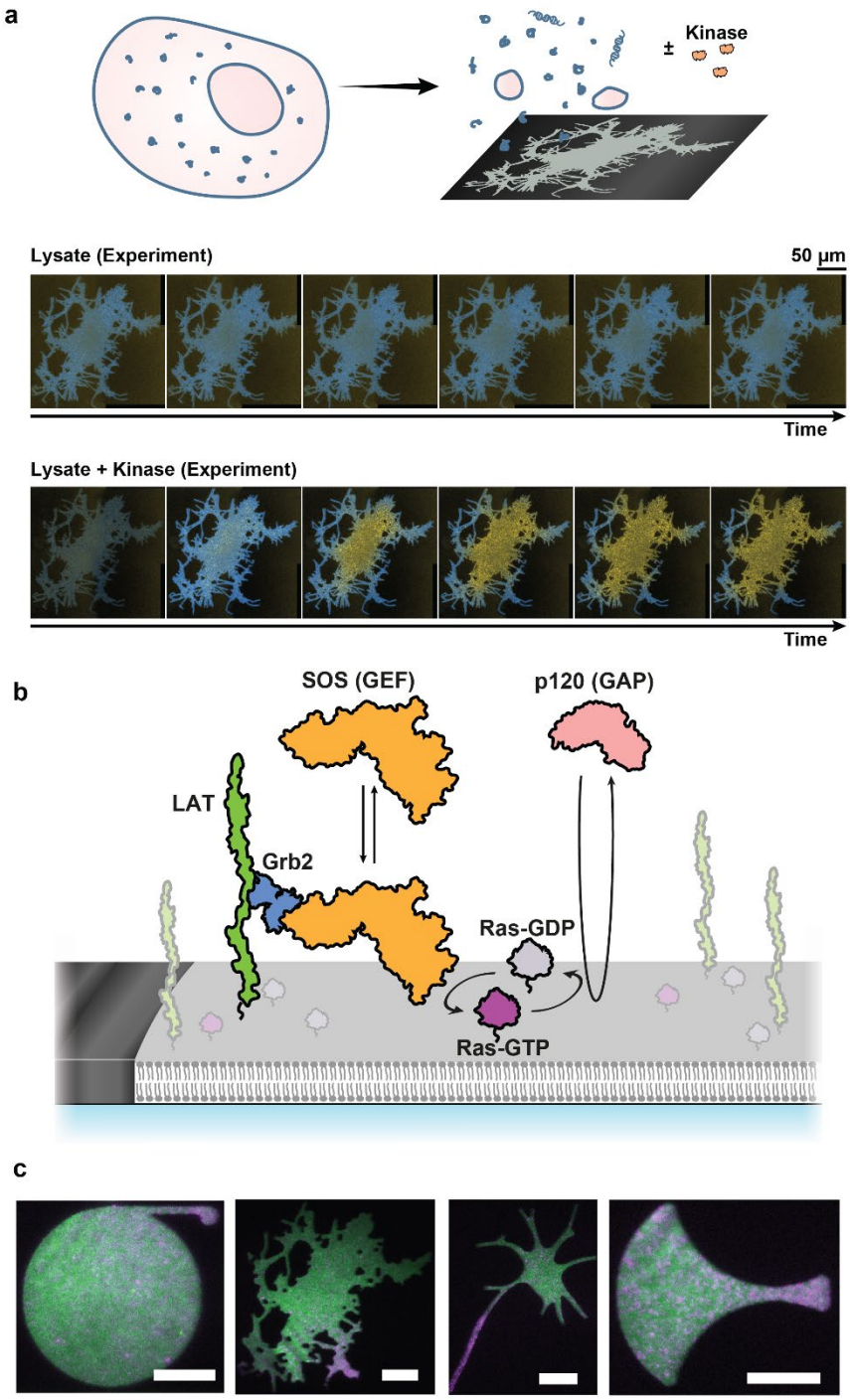

Figure 4-5 Hybrid Lysate experiment and SOS-p120GAP polarization. (a) Top: Schematic of the hybrid lysate experiment. Bottom: Time sequence images of the lysate and hybrid lysate competition reaction. (b) Schematic of the kinetic processes of the SOS-p120GAP competition reaction. (c) Examples of polarized SOS-p120GAP competition reaction in diverse geometries. Scale bar 20 μm.

4.6 Hybrid cellular extract polarizes the supported PIP membrane

Next, we asked whether natural contents inside a cell will also manifest a similar effect when exposed to the *in vitro* membrane. To test this, we prepared pig leukocyte lysate and introduced it to an unconfined supported membrane to examine its activity on PIP lipids. The membrane composition was identical to the previous setup, 96 mol% DOPC, 2 mol% PI4P, and 2 mol% PI(4,5)P_2. Treating the membrane with the lysate leads to an PI4P dominated state homogeneously across the membrane. This suggest that the lysate has a stronger phosphatase activity. To mimic the scenario of an upregulation of kinase activity in the cells, we added PIP5K to the lysate, creating a hybrid lysate. Introducing the hybrid lysate to filopodia-rich cell-shaped membranes initially failed to produce polarization. However, when increasing the size by a factor of two (increasing the longest axis approximately from 120 μm to 240 μm), we observed polarization that resembles the polarization produced by purified OCRL and PIP5K. This suggests that the hybrid cell lysate has a slightly different characteristic length scale of polarization. The observation demonstrates that when presented to a two-dimensional membrane shape, natural cellular constituents exhibit the ability to polarize in response to geometry.

4.7 SOS – p120GAP competition polarizes Ras functionalized membrane

The simulation results demonstrate that the requirement for stochastic polarization to emerge is very simple, and exists in many naturally occurring membrane competition reactions. The interconversion of Ras-GTP and Ras-GDP by guanine nucleotide exchange factor (GEF) and GTPase activating protein (GAP) is one example. Ras is switched-on when guanine nucleotide exchange factor (e.g., Son of Sevenless; SOS) exchanges the Ras-bound GDP to GTP and switched-off when GTPase activating proteins (e.g., p120GAP) facilitate Ras to hydrolyze the bound GTP to GDP. We purified the catalytic domain of p120GAP (hereafter referred as p120GAP), which acts on its substrate (Ras-GTP) directly from the solution without feedback. On the other hand, SOS gets recruited to the membrane via Grb2, which binds to the scaffolding linker for activation of T-cells (LAT). Membrane-recruited SOS can bind to Ras via its allosteric site and enter a highly processive state(*39*, *48*). The allosteric site has a higher affinity for Ras-GTP compared to Ras-GDP, leading to positive feedback in SOS reaction(*164*).

We functionalized both Ras and LAT molecules on the supported lipid bilayer, on which the LAT was fluorescently labeled (Alexa555-LAT) to monitor its distribution. Grb2 is included in the experiments to recruit SOS to LAT(*44*). We used the previously developed Ras-binding domain of Raf1 (Alexa647-RBD) to monitor the distribution of activated Ras(*44*). Before the competition reaction, LAT was distributed evenly on the membranes, and Ras existed entirely in its inactive form. When we introduced the competing pair SOS and p120GAP for the reaction, a small number of membranes showed locally activated Ras molecules. The localization was markedly biased towards the narrow peripheral features of the membrane geometry (Fig. 5b). It is clear from the homogeneous distribution of the LAT on the membrane that the polarization did not occur through altered distribution of LAT but through the underlying kinetics of GEF-GAP competition reaction. Therefore, this observation shows that the geometry-driven near-deterministic

polarizing influence is also present under the GEF-GAP competition, similar to the PIP kinase-phosphatase competition.

4.8 Discussion

Polarization of cellular signaling molecules is a well-observed, yet mechanistically poorly understood phenomenon. The interpretation of spontaneous polarization is largely dependent on Turing's theory. However, Turing's theory may not be applicable to all polarization phenomena since it requires kinetic conditions that may be difficult to satisfy(*13*). Here, we have shown that reactions on the membrane can polarize through intrinsically stochastic mechanisms with very simple kinetic requirements. Reconstitution experiments and stochastic simulations unequivocally demonstrated that the polarization occurs only in systems with high stochasticity. Despite the stochastic nature of polarization, once the system is polarized, it will polarize in a direction near-deterministically. in which deterministic kinetics cannot accurately predict polarization, let alone near-deterministic directionality. These features cannot be explained by conventional theories that rely on deterministic kinetics.

We observed two opposite directions of polarization in relation to the membrane binding property of the competing enzymes; In the small corners of the PIP competition reaction, the membrane-localizing PIP5K is weakened compared to OCRL. By contrast, in the Ras competition reaction, the membrane-localizing SOS dominated over GAP exclusively at the corners. It is possible that the opposite behaviors are due to differences in kinetic parameters; PIP5K has a strong, high-order positive feedback, while SOS has a much weaker feedback(*103*). However, SOS exhibits extreme processivity at the membrane that PIP5K lacks(*34*). Previous examples have shown that stochastic reactions with positive feedback will be disfavored in small-scale reactions compared to larger-scale reactions(*103*). Independently, stochastic reactions with high processivity can activate and overcome the opposing reaction much more readily in small-scale reactions than in bigger reactions (Chapter 3). We thus speculate that the direction of stochastic polarizations may be controlled by the relative strength of the positive feedback and the processivity of the enzymes.

It is well-known that polarized reactions often lead to asymmetric changes in cellular geometry. It has been shown that cellular geometry could potentially influence polarization reactions, achieving mutual regulation, but detailed mechanistic understanding is lacking. The unique features of stochastic polarization mechanisms are that polarization only emerges with the presence of two-dimensional geometrical confinements, and the localization of the signaling molecules strictly follows the geometrical feature in a near-deterministic manner, demonstrating a stark contrast to the behavior of Turing patterns. The influence of two-dimensional geometry in the Turing pattern is limited to aligning the pattern rather than precise localization. The potential of stochastic polarization to enable cells to polarize in a highly consistent manner with respect to cellular geometries could present benefits over Turing patterning does not in a scenario where directionality is important.

Stochastic polarization is not the only mechanism that could respond to cellular geometries. Previously, the difference in the surface-to-volume ratio has been proposed to direct cyclic adenosine monophosphate (cAMP) signaling(*53*). Reaction-diffusion systems such as the Min system also respond to their surrounding geometry, although in an oscillatory manner(*155*). However, what is unique about stochastic polarization

lies in the simplicity of its requirements. It does not require any three-dimensional geometrical features or complex mechanisms, such as the molecular timing of nucleotide exchange programmed in the Min system. The major requirements —asymmetric membrane binding kinetics in the opposing enzymes, two-dimensional membrane geometry with differential confinement, and stochasticity— are easily satisfied in the native reaction environment inside a cell. This is supported by the ability of hybrid cell lysates to exhibit characteristics of stochastic polarization.

Our experiments have shown that stochastic polarization can be readily achieved in two types of ubiquitous membrane reaction: PIP phosphorylation-dephosphorylation and small GTPase activation-deactivation. Within these two types of membrane reactions, many are known to polarize. For example, PTEN and PI3k competition reaction can lead to PI(3,4,5)P3 polarization in motile cells(*165*), Cdc42 is well-known to polarize(*166*), competition between the GEF and GAP of Rab5 can polarize Rab5-GTP(*31*), PI(3,4)P2 has also been shown to polarize in apical-basal polarization(*167*). In addition, signaling reactions such as tyrosine phosphorylation-dephosphorylation also exhibit the basic requirement for stochastic polarization to emerge and are thus likely subjected to stochastic polarizations in cells(*4*). Although the strength of stochastic polarization effects inside a living cell is yet to be discovered, the accessibility of the pre-requisites suggests that the stochastic polarization mechanism could play a significant role in polarization reactions in cells.

Chapter 5
FINAL REMARKS

In this dissertation, I presented two types of stochastic effects that can deviate membrane reactions from the description of classical chemical kinetics. I first showed that the apparent speed of a reaction with positive feedback can be slower when reacting in small membrane areas, and I have demonstrated that this is due to the discrete nature of individual reactions (Chapter 2). The second effect presented (Chapter 3) is that the outcome of a competition reaction can be bistable only when reacting in a small membrane area. This is because of the fluctuations in the reaction generated by the strong out of equilibrium activity from a low copy number of enzymes. In Chapter 4, I have showed that in two-dimensional membranes mimicking the contours of various cell types, these stochastic effects can emerge into polarization of signaling molecules on the membrane. This demonstrated a broader consequence of the two stochastic effects introduced in Chapter 2 and 3. Although this dissertation only explored very simple competition reactions, such effects can potentially lead to cell level, or even system and organism level physiological consequences, as local dynamics can be propagated and amplified through signal transduction.

While the stochastic effects described in this dissertation appear exotic since they cannot be explained by classical chemical kinetics, I would argue that such phenomena are likely commonplace in cellular signaling reactions. An interesting article by Peter J. Hailing in 1989 nicely explained why this might be the case(*128*). Fundamentally, chemical reactions are comprised of the random and discrete nature of individual molecular interactions. Thus, a stochastic model is intrinsically a more accurate description of molecular reaction systems. From statistical mechanics, we were able to derive the classical chemical kinetics with a set of limiting approximations. We are very accustomed to relying on classical chemical kinetics formalism (reaction rate equations or mass action kinetics) to describe signaling reactions in the cells. There is an important point to remember, however: classical chemical kinetic models are only approximations; they don't accurately capture the random and discrete nature of the individual molecular reactions. Biochemical reactions in cells are inherently in a microscopic regime, where the small size of cellular structures make the reaction highly stochastic. Under such circumstances, the approximations of classical chemical kinetics often do not hold, and stochastic effects can emerge.

In this dissertation, I have highlighted a few cases where a reaction can deviate substantially from the predictions of classical kinetics. The mechanisms are very simple and easily understood, sometimes thought of as trivial, but the consequences are undeniably surprising. I believe that this shows that we have only revealed the tip of the iceberg. Many more complex mechanisms that can lead to stochastic effects are yet to be discovered. However, I hope that this dissertation can serve as a reminder that all reactions in cells are fundamentally stochastic. To ensure that kinetic analyses or molecular models are faithfully capturing the dynamics of cellular reactions, it is important to not assume the reaction conforms to deterministic rules. One must either study the reaction in a scale that is reminiscent of the type found in cells or else rigorously confirm that there are no appreciable stochastic effects. I believe that this mindset will greatly propel our understanding of the complex biological reactions in cells.

REFERENCES

1. H. F. Lodish, A. Berk, C. Kaiser, M. Krieger, A. Bretscher, H. L. Ploegh, K. C. Martin, M. B. Yaffe, A. Amon, *Molecular cell biology* (ed. 9, 2021).

2. J. T. Groves, J. Kuriyan, Molecular mechanisms in signal transduction at the membrane. *Nature Structural & Molecular Biology 2010 17:6*. **17**, 659–665 (2010).

3. J. L. Bos, H. Rehmann, A. Wittinghofer, GEFs and GAPs: Critical Elements in the Control of Small G Proteins. *Cell*. **129**, 865–877 (2007).

4. R. Avraham, Y. Yarden, Feedback regulation of EGFR signalling: decision making by early and delayed loops. *Nature Reviews Molecular Cell Biology* **12**, 104–117 (2011).

5. G. Di Paolo, P. De Camilli, Phosphoinositides in cell regulation and membrane dynamics. *Nature*. **443**, 651–657 (2006).

6. S. D. Hansen, W. Y. C. Huang, Y. K. Lee, P. Bieling, S. M. Christensen, J. T. Groves, Stochastic geometry sensing and polarization in a lipid kinase–phosphatase competitive reaction. *Proc Natl Acad Sci U S A*. **116**, 15013–15022 (2019).

7. Q. Hu, L. Milenkovic, H. Jin, M. P. Scott, M. V Nachury, E. T. Spiliotis, W. J. Nelson, A septin diffusion barrier at the base of the primary cilium maintains ciliary membrane protein distribution. *Science*. **329**, 436–439 (2010).

8. M. Simunovic, J. B. Manneville, H. F. Renard, E. Evergren, K. Raghunathan, D. Bhatia, A. K. Kenworthy, G. A. Voth, J. Prost, H. T. McMahon, L. Johannes, P. Bassereau, A. Callan-Jones, Friction Mediates Scission of Tubular Membranes Scaffolded by BAR Proteins. *Cell*. **170**, 172-184.e11 (2017).

9. A. Kusumi, T. K. Fujiwara, R. Chadda, M. Xie, T. A. Tsunoyama, Z. Kalay, R. S. Kasai, K. G. N. Suzuki, Dynamic Organizing Principles of the Plasma Membrane that Regulate Signal Transduction: Commemorating the Fortieth Anniversary of Singer and Nicolson's Fluid-Mosaic Model. *Annu. Rev. Cell Dev. Biol*. **28**, 215–250 (2012).

10. M. Samoilov, S. Plyasunov, A. P. Arkin, Stochastic amplification and signaling in enzymatic futile cycles through noise-induced bistability with oscillations. *Proc Natl Acad Sci U S A*. **102**, 2310–2315 (2005).

11. L. M. Bishop, H. Qian, Stochastic Bistability and Bifurcation in a Mesoscopic Signaling System with Autocatalytic Kinase. *Biophysical Journal*. **98**, 1–11 (2010).

12. T. L. To, N. Maheshri, Noise can induce bimodality in positive transcriptional feedback loops without bistability. *Science*. **327**, 1142–1145 (2010).

13. A. M. Turing, The Chemical Basis of Morphogenesis. *Philosophical Transactions of the Royal Society B: Biological Sciences*. **237**, 37–72 (1952).

14. T. Wilhelm, The smallest chemical reaction system with bistability. *BMC Systems Biology*. **3**, 90 (2009).

15. I. R. Epstein, K. Showalter, Nonlinear chemical dynamics: Oscillations, patterns, and chaos. *Journal of Physical Chemistry*. **100**, 13132–13147 (1996).

16. S. Kondo, T. Miura, Reaction-diffusion model as a framework for understanding biological pattern formation. *Science*. **329**, 1616–1620 (2010).

17. M. Merchant, J. Moffat, G. Schaefer, J. Chan, X. Wang, C. Orr, J. Cheng, T. Hunsaker, L. Shao, S. J. Wang, M.-C. Wagle, E. Lin, P. M. Haverty, S. Shahidi-Latham, H. Ngu, M. Solon, J. Eastham-Anderson, H. Koeppen, S.-M. A. Huang, J. Schwarz, M. Belvin, D. Kirouac, M. R. Junttila, Combined MEK and ERK inhibition overcomes therapy-mediated pathway reactivation in RAS mutant tumors. *PLOS ONE*. **12**, e0185862 (2017).

18. M. Halasz, B. N. Kholodenko, W. Kolch, T. Santra, Integrating network reconstruction with mechanistic modeling to predict cancer therapies. *Science Signaling*. **9**, ra114 (2016).

19. J. Meyers, J. Craig, D. J. Odde, Potential for Control of Signaling Pathways via Cell Size and Shape. *Current Biology*. **16**, 1685–1693 (2006).

20. J. B. Moseley, A. Mayeux, A. Paoletti, P. Nurse, A spatial gradient coordinates cell size and mitotic entry in fission yeast. *Nature*. **459**, 857–860 (2009).

21. Y. H. M. Chan, W. F. Marshall, How cells know the size of their organelles. *Science*. **337**, 1186–1189 (2012).

22. K. D. Mossman, G. Campi, J. T. Groves, M. L. Dustin, Altered TCR signaling from geometrically repatterned immunological synapses. *Science*. **310**, 1191–1193 (2005).

23. J. J. Y. Lin, S. T. Low-Nam, K. N. Alfieri, D. B. McAffee, N. C. Fay, J. T. Groves, Mapping the stochastic sequence of individual ligand-receptor binding events to cellular activation: T cells act on the rare events. *Science Signaling*. **12**, eaat8715 (2019).

24. J. Paulsson, O. G. Berg, M. Ehrenberg, Stochastic focusing: Fluctuation-enhanced sensitivity of intracellular regulation. *Proc Natl Acad Sci U S A*. **97**, 7148–7153 (2000).

25. E. Korobkova, T. Emonet, J. M. G. Vilar, T. S. Shimizu, P. Cluzel, From molecular noise to behavioural variability in a single bacterium. *Nature*. **428**, 574–578 (2004).

26. M. Samoilov, S. Plyasunov, A. P. Arkin, Stochastic amplification and signaling in enzymatic futile cycles through noise-induced bistability with oscillations. *Proc Natl Acad Sci U S A*. **102**, 2310–2315 (2005).

27. B. G. Neel, H. Gu, L. Pao, The 'Shp'ing news: SH2 domain-containing tyrosine phosphatases in cell signaling. *Trends in Biochemical Sciences*. **28**, 284–293 (2003).

28. M. Pirruccello, P. De Camilli, Inositol 5-phosphatases: Insights from the Lowe syndrome protein OCRL. *Trends in Biochemical Sciences*. **37**, 134–143 (2012).

29. I. van den Bout, N. Divecha, PIP5K-driven PtdIns(4,5)P2 synthesis: Regulation and cellular functions. *Journal of Cell Science*. **122**, 3837–3850 (2009).

30. G. M. Carman, R. A. Deems, E. A. Dennis, Lipid signaling enzymes and surface dilution kinetics. *J Biol Chem*. **270**, 18711–18714 (1995).

31. U. Bezeljak, H. Loya, B. Kaczmarek, T. E. Saunders, M. Loose, Stochastic activation and bistability in a Rab GTPase regulatory network. *Proceedings of the National Academy of Sciences*. **117**, 6540–6549 (2020).

32. A. Cezanne, J. Lauer, A. Solomatina, I. F. Sbalzarini, M. Zerial, A non-linear system patterns rab5 gtpase on the membrane. *Elife*. **9**, 1–22 (2020).

33. M. Schmick, P. I. H. Bastiaens, The interdependence of membrane shape and cellular signal processing. *Cell*. **156** (2014), pp. 1132–1138.

34. L. Iversen, S. Mathiasen, J. B. Larsen, D. Stamou, Membrane curvature bends the laws of physics and chemistry. *Nature Chemical Biology*. **11**, 822–825 (2015).

35. B. D. Hopkins, C. Hodakoski, D. Barrows, S. M. Mense, R. E. Parsons, PTEN function: The long and the short of it. *Trends in Biochemical Sciences*. **39**, 183–190 (2014).

36. C. Liu, S. Deb, V. S. Ferreira, E. Xu, T. Baumgart, Kinetics of PTEN-mediated PI(3,4,5)P3 hydrolysis on solid supported membranes. *PLOS ONE*. **13**, e0192667 (2018).

37. R. Verger, G. H. De Haas, Interfacial Enzyme Kinetics of Lipolysis. *Annual Review of Biophysics and Bioengineering*. **5**, 77–117 (1976).

38. M. K. Jain, O. G. Berg, The kinetics of interfacial catalysis by phospholipase A2 and regulation of interfacial activation: hopping versus scooting. *Biochimica et Biophysica Acta (BBA) - Lipids and Lipid Metabolism*. **1002**, 127–156 (1989).

39. L. Iversen, H.-L. Tu, W.-C. Lin, S. M. Christensen, S. M. Abel, J. Iwig, H.-J. Wu, J. Gureasko, C. Rhodes, R. S. Petit, S. D. Hansen, P. Thill, C.-H. Yu, D. Stamou, A. K. Chakraborty, J. Kuriyan, J. T. Groves, Ras activation by SOS: Allosteric regulation by altered fluctuation dynamics. *Science*. **345**, 50–54 (2014).

40. F. Olson, C. A. Hunt, F. C. Szoka, W. J. Vail, D. Papahadjopoulos, Preparation of liposomes of defined size distribution by extrusion through polycarbonate membranes. *Biochimica et Biophysica Acta (BBA) - Biomembranes*. **557**, 9–23 (1979).

41. M. Brune, J. L. Hunter, J. E. T. Corrie, M. R. Webb, Direct, Real-Time Measurement of Rapid Inorganic Phosphate Release Using a Novel Fluorescent Probe and Its Application to Actomyosin Subfragment 1 ATPase. *Biochemistry*. **33**, 8262–8271 (1994).

42. M. M. Baksh, M. Jaros, J. T. Groves, Detection of molecular interactions at membrane surfaces through colloid phase transitions. *Nature*. **427**, 139–141 (2004).

43. J. T. Groves, N. Ulman, S. G. Boxer, Micropatterning fluid lipid bilayers on solid supports. *Science*. **275**, 651–653 (1997).

44. W. Y. C. Huang, S. Alvarez, Y. Kondo, Y. Kwang Lee, J. K. Chung, H. Y. Monatrice Lam, K. H. Biswas, J. Kuriyan, J. T. Groves, A molecular assembly phase transition and kinetic proofreading modulate Ras activation by SOS. *Science*. **363**, 1098–1103 (2019).

45. R. B. Campbell, F. Liu, A. H. Ross, Allosteric Activation of PTEN Phosphatase by Phosphatidylinositol 4,5-Bisphosphate. *Journal of Biological Chemistry*. **278**, 33617–33620 (2003).

46. G. McConnachie, I. Pass, S. M. Walker, C. P. Downes, Interfacial kinetic analysis of the tumour suppressor phosphatase, PTEN: evidence for activation by anionic phospholipids. *Biochemical Journal*. **371**, 947–955 (2003).

47. S. Schoebel, W. Blankenfeldt, R. S. Goody, A. Itzen, High-affinity binding of phosphatidylinositol 4-phosphate by Legionella pneumophila DrrA. *EMBO Rep*. **11**, 598–604 (2010).

48. S. M. Margarit, H. Sondermann, B. E. Hall, B. Nagar, A. Hoelz, M. Pirruccello, D. Bar-Sagi, J. Kuriyan, Structural Evidence for Feedback Activation by Ras·GTP of the Ras-Specific Nucleotide Exchange Factor SOS. *Cell*. **112**, 685–695 (2003).

49. S. M. Christensen, H.-L. Tu, J. E. Jun, S. Alvarez, M. G. Triplet, J. S. Iwig, K. K. Yadav, D. Bar-Sagi, J. P. Roose, J. T. Groves, One-way membrane trafficking of SOS in receptor-triggered Ras activation. *Nature Structural & Molecular Biology*. **23**, 838–846 (2016).

50. Y. K. Lee, S. T. Low-Nam, J. K. Chung, S. D. Hansen, H. Y. M. Lam, S. Alvarez, J. T. Groves, Mechanism of SOS PR-domain autoinhibition revealed by single-molecule assays on native protein from lysate. *Nature Communications*. **8**, 15061 (2017).

51. M. Y. Hein, N. C. Hubner, I. Poser, J. Cox, N. Nagaraj, Y. Toyoda, I. A. Gak, I. Weisswange, J. Mansfeld, F. Buchholz, A. A. Hyman, M. Mann, A Human Interactome in Three Quantitative Dimensions Organized by Stoichiometries and Abundances. *Cell*. **163**, 712–723 (2015).

52. D. T. Gillespie, Stochastic Simulation of Chemical Kinetics. *Annual Review of Physical Chemistry*. **58**, 35–55 (2007).

53. S. R. Neves, P. Tsokas, A. Sarkar, E. A. Grace, P. Rangamani, S. M. Taubenfeld, C. M. Alberini, J. C. Schaff, R. D. Blitzer, I. I. Moraru, R. Iyengar, Cell Shape and Negative Links in Regulatory Motifs Together Control Spatial Information Flow in Signaling Networks. *Cell*. **133**, 666–680 (2008).

54. P. Rangamani, A. Lipshtat, E. U. Azeloglu, R. C. Calizo, M. Hu, S. Ghassemi, J. Hone, S. Scarlata, S. R. Neves, R. Iyengar, Decoding Information in Cell Shape. *Cell*. **154**, 1356 (2013).

55. M. Schmick, P. I. H. Bastiaens, The interdependence of membrane shape and cellular signal processing. *Cell*. **156**, 1132–1138 (2014).

56. V. Varga, J. Helenius, K. Tanaka, A. A. Hyman, T. U. Tanaka, J. Howard, Yeast kinesin-8 depolymerizes microtubules in a length-dependent manner. *Nature Cell Biology* **8**, 957–962 (2006).

57. L. Mohapatra, B. L. Goode, J. Kondev, Antenna Mechanism of Length Control of Actin Cables. *PLOS Computational Biology*. **11**, e1004160 (2015).

58. J. Schweizer, M. Loose, M. Bonny, K. Kruse, I. Moŋch, P. Schwille, Geometry sensing by self-organized protein patterns. *Proc Natl Acad Sci U S A*. **109**, 15283–15288 (2012).

59. H. P. Wacklin, F. Tiberg, G. Fragneto, R. K. Thomas, Distribution of reaction products in phospholipase A2 hydrolysis. *Biochimica et Biophysica Acta (BBA) - Biomembranes*. **1768**, 1036–1049 (2007).

60. A. C. Butty, N. Perrinjaquet, A. Petit, M. Jaquenoud, J. E. Segall, K. Hofmann, C. Zwahlen, M. Peter, A positive feedback loop stabilizes the guanine-nucleotide exchange factor Cdc24 at sites of polarization. *EMBO Journal*. **21**, 1565–1576 (2002).

61. Q. Lin, W. Yang, D. Baird, Q. Feng, R. A. Cerione, Identification of a DOCK180-related guanine nucleotide exchange factor that is capable of mediating a positive feedback activation of Cdc42. *Journal of Biological Chemistry*. **281**, 35253–35262 (2006).

62. F. Medina, A. M. Carter, O. Dada, S. Gutowski, J. Hadas, Z. Chen, P. C. Sternweis, Activated RhoA is a positive feedback regulator of the Lbc family of Rho guanine nucleotide exchange factor proteins. *Journal of Biological Chemistry*. **288**, 11325–11333 (2013).

63. R. Lippé, M. Miaczynska, V. Rybin, A. Runge, M. Zerial, Functional synergy between Rab5 effector Rabaptin-5 and exchange factor Rabex-5 when physically associated in a complex. *Molecular Biology of the Cell*. **12**, 2219–2228 (2001).

64. D. Stalder, H. Barelli, R. Gautier, E. Macia, C. L. Jackson, B. Antonny, Kinetic studies of the arf activator arno on model membranes in the presence of arf effectors suggest control by a positive feedback loop. *Journal of Biological Chemistry*. **286**, 3873–3883 (2011).

65. K. He, R. Marsland III, S. Upadhyayula, E. Song, S. Dang, B. R. Capraro, W. Wang, W. Skillern, R. Gaudin, M. Ma, T. Kirchhausen, Dynamics of phosphoinositide conversion in clathrin-mediated endocytic traffic. *Nature*. **552**, 410–414 (2017).

66. P. K. Mattila, P. Lappalainen, Filopodia: molecular architecture and cellular functions. *Nature Reviews Molecular Cell Biology*. **9**, 446–454 (2008).

67. L. B. Case, J. A. Ditlev, M. K. Rosen, Regulation of Transmembrane Signaling by Phase Separation. *Annual Review of Biophysics*. **48**, 465–494 (2019).

68. M. V. Milburn, L. Tong, A. M. DeVos, A. Brünger, Z. Yamaizumi, S. Nishimura, S. H. Kim, Molecular Switch for Signal Transduction: Structural Differences Between Active and Inactive Forms of Protooncogenic ras Proteins. *Science*. **247**, 939–945 (1990).

69. S. L. Campbell, R. Khosravi-Far, K. L. Rossman, G. J. Clark, C. J. Der, Increasing complexity of Ras signaling. *Oncogene*. **17**, 1395–1413 (1998).

70. A. E. Karnoub, R. A. Weinberg, Ras oncogenes: split personalities. *Nature Reviews Molecular Cell Biology*. **9**, 517–531 (2008).

71. M. S. Boguski, F. McCormick, Proteins regulating Ras and its relatives. *Nature.* **366**, 643–654 (1993).

72. P. Bandaru, Y. Kondo, J. Kuriyan, The interdependent activation of son-of-sevenless and ras. *Cold Spring Harbor Perspectives in Medicine*. **9** (2019), doi:10.1101/cshperspect.a031534.

73. P. A. Boriack-Sjodin, S. M. Margarit, D. Bar-Sagi, J. Kuriyan, The structural basis of the activation of Ras by Sos. *Nature*. **394**, 337–343 (1998).

74. K. Scheffzek, M. R. Ahmadian, W. Kabsch, L. Wiesmüller, A. Lautwein, F. Schmitz, A. Wittinghofer, The Ras-RasGAP Complex: Structural Basis for GTPase Activation and Its Loss in Oncogenic Ras Mutants. *Science*. **277**, 333–339 (1997).

75. S. Schubbert, K. Shannon, G. Bollag, Hyperactive Ras in developmental disorders and cancer. *Nature Reviews Cancer*. **7**, 295–308 (2007).

76. A. R. Moore, S. C. Rosenberg, F. McCormick, S. Malek, RAS-targeted therapies: is the undruggable drugged? *Nature Reviews Drug Discovery*. **19**, 533–552 (2020).

77. J. A. Parker, C. Mattos, The K-Ras, N-Ras, and H-Ras Isoforms: Unique Conformational Preferences and Implications for Targeting Oncogenic Mutants. *Cold Spring Harbor Perspectives in Medicine*. **8**, a031427 (2018).

78. S. Lu, H. Jang, S. Muratcioglu, A. Gursoy, O. Keskin, R. Nussinov, J. Zhang, Ras Conformational Ensembles, Allostery, and Signaling. *Chemical Reviews*. **116**, 6607–6665 (2016).

79. I. A. Prior, C. Muncke, R. G. Parton, J. F. Hancock, Direct visualization of Ras proteins in spatially distinct cell surface microdomains. *Journal of Cell Biology*. **160**, 165–170 (2003).

80. T. Tian, A. Harding, K. Inder, S. Plowman, R. G. Parton, J. F. Hancock, Plasma membrane nanoswitches generate high-fidelity Ras signal transduction. *Nature Cell Biology*. **9**, 905–914 (2007).

81. Y. Zhou, P. Prakash, A. A. Gorfe, J. F. Hancock, Ras and the Plasma Membrane: A Complicated Relationship. *Cold Spring Harbor Perspectives in Medicine*. **8**, a031831 (2018).

82. J. K. Chung, Y. K. Lee, J. P. Denson, W. K. Gillette, S. Alvarez, A. G. Stephen, J. T. Groves, K-Ras4B Remains Monomeric on Membranes over a Wide Range of Surface Densities and Lipid Compositions. *Biophysical Journal*. **114**, 137–145 (2018).

83. M. R. Packer, J. A. Parker, J. K. Chung, Z. Li, Y. K. Lee, T. Cookis, H. Guterres, S. Alvarez, M. A. Hossain, D. P. Donnelly, J. N. Agar, L. Makowski, M. Buck, J. T. Groves, C. Mattos, Raf promotes dimerization of the Ras G-domain with increased allosteric connections. *Proc Natl Acad Sci U S A*. **118**, e2015648118 (2021).

84. J. K. Chung, Y. K. Lee, H. Y. M. Lam, J. T. Groves, Covalent Ras Dimerization on Membrane Surfaces through Photosensitized Oxidation. *J Am Chem Soc*. **138**, 1800–1803 (2016).

85. D. K. Simanshu, D. V. Nissley, F. McCormick, RAS Proteins and Their Regulators in Human Disease. *Cell*. **170**, 17–33 (2017).

86. A. D. Cox, S. W. Fesik, A. C. Kimmelman, J. Luo, C. J. Der, Drugging the undruggable RAS: Mission Possible? *Nature Reviews Drug Discovery*. **13**, 828–851 (2014).

87. J. E. Ferrell, E. M. Machleder, The biochemical basis of an all-or-none cell fate switch in xenopus oocytes. *Science*. **280**, 895–898 (1998).

88. G. Altan-Bonnet, R. N. Germain, Modeling T Cell Antigen Discrimination Based on Feedback Control of Digital ERK Responses. *PLOS Biology*. **3**, e356 (2005).

89. J. Das, M. Ho, J. Zikherman, C. Govern, M. Yang, A. Weiss, A. K. Chakraborty, J. P. Roose, Digital Signaling and Hysteresis Characterize Ras Activation in Lymphoid Cells. *Cell*. **136**, 337–351 (2009).

90. J. E. Jun, M. Yang, H. Chen, A. K. Chakraborty, J. P. Roose, Activation of Extracellular Signal-Regulated Kinase but Not of p38 Mitogen-Activated Protein Kinase Pathways in Lymphocytes Requires Allosteric Activation of SOS. *Molecular and Cellular Biology*. **33**, 2470–2484 (2013).

91. J. D. McLaurin, O. D. Weiner, Multiple sources of signal amplification within the B-cell Ras/MAPK pathway. *Molecular Biology of the Cell*. **30**, 1610–1620 (2019).

92. Y. Ogura, F.-L. Wen, M. M. Sami, T. Shibata, S. Hayashi, A Switch-like Activation Relay of EGFR-ERK Signaling Regulates a Wave of Cellular Contractility for Epithelial Invagination. *Developmental Cell*. **46**, 162–172 (2018).

93. Y. Shindo, K. Iwamoto, K. Mouri, K. Hibino, M. Tomita, H. Kosako, Y. Sako, K. Takahashi, Conversion of graded phosphorylation into switch-like nuclear translocation via autoregulatory mechanisms in ERK signalling. *Nature Communications*. **7**, 1–10 (2016).

94. X. K. Lun, V. R. T. Zanotelli, J. D. Wade, D. Schapiro, M. Tognetti, N. Dobberstein, B. Bodenmiller, Influence of node abundance on signaling network state and dynamics analyzed by mass cytometry. *Nature Biotechnology*. **35**, 164–172 (2017).

95. J. E. Ferrell, W. Xiong, Bistability in cell signaling: How to make continuous processes discontinuous, and reversible processes irreversible. *Chaos*. **11**, 227 (2001).

96. U. S. Bhalla, R. Iyengar, Emergent properties of networks of biological signaling pathways. *Science*. **283**, 381–387 (1999).

97. M. Laurent, N. Kellershohn, Multistability: a major means of differentiation and evolution in biological systems. *Trends in Biochemical Sciences*. **24**, 418–422 (1999).

98. S. M. Abel, J. P. Roose, J. T. Groves, A. Weiss, A. K. Chakraborty, The membrane environment can promote or suppress bistability in cell signaling networks. *Journal of Physical Chemistry B*. **116**, 3630–3640 (2012).

99. A. Prasad, J. Zikherman, J. Das, J. P. Roose, A. Weiss, A. K. Chakraborty, Origin of the sharp boundary that discriminates positive and negative selection of thymocytes. *Proc Natl Acad Sci U S A*. **106**, 528–533 (2009).

100. S. M. Coyle, W. A. Lim, Mapping the functional versatility and fragility of Ras GTPase signaling circuits through in vitro network reconstitution. *Elife*. **5** (2016), doi:10.7554/ELIFE.12435.001.

101. L. K. Nguyen, B. N. Kholodenko, Feedback regulation in cell signalling: Lessons for cancer therapeutics. *Seminars in Cell & Developmental Biology*. **50**, 85–94 (2016).

102. B. N. Kholodenko, N. Rauch, W. Kolch, O. S. Rukhlenko, A systematic analysis of signaling reactivation and drug resistance. *Cell Reports*. **35**, 109157 (2021).

103. A. A. Lee, W. Y. C. Huang, S. D. Hansen, N. H. Kim, S. Alvarez, J. T. Groves, J. T. G. Designed, S. A. Performed, Stochasticity and positive feedback enable enzyme kinetics at the membrane to sense reaction size. *Proceedings of the National Academy of Sciences*. **118**, e2103626118 (2021).

104. H. Sondermann, S. M. Soisson, S. Boykevisch, S. S. Yang, D. Bar-Sagi, J. Kuriyan, Structural Analysis of Autoinhibition in the Ras Activator Son of Sevenless. *Cell*. **119**, 393–405 (2004).

105. L. A. Chylek, L. A. Harris, C. S. Tung, J. R. Faeder, C. F. Lopez, W. S. Hlavacek, Rule-based modeling: a computational approach for studying biomolecular site dynamics in cell signaling systems. *Wiley Interdisciplinary Reviews: Systems Biology and Medicine*. **6**, 13–36 (2014).

106. M. Kochańczyk, P. Kocieniewski, E. Kozłowska, J. Jaruszewicz-Błońska, B. Sparta, M. Pargett, J. G. Albeck, W. S. Hlavacek, T. Lipniacki, Relaxation oscillations and hierarchy of feedbacks in MAPK signaling. *Scientific Reports*. **7**, 1–15 (2017).

107. H. Qian, Cooperativity in Cellular Biochemical Processes: Noise-Enhanced Sensitivity, Fluctuating Enzyme, Bistability with Nonlinear Feedback, and Other Mechanisms for Sigmoidal Responses. *Annual Review of Biophysics*. **41**, 179–204 (2012).

108. C.-W. Lin, L. M. Nocka, B. L. Stinger, J. B. DeGrandchamp, L. J. N. Lew, S. Alvarez, H. T. Phan, Y. Kondo, J. Kuriyan, J. T. Groves, A two-component protein condensate of the EGFR cytoplasmic tail and Grb2 regulates Ras activation by SOS at the membrane. *Proceedings of the National Academy of Sciences*. **119**, e2122531119 (2022).

109. M. H. Hofmann, M. Gmachl, J. Ramharter, F. Savarese, D. Gerlach, J. R. Marszalek, M. P. Sanderson, D. Kessler, F. Trapani, H. Arnhof, K. Rumpel, D. A. Botesteanu, P. Ettmayer, T. Gerstberger, C. Kofink, T. Wunberg, A. Zoephel, S. C. Fu, J. L. Teh, J. Böttcher, N. Pototschnig, F. Schachinger, K. Schipany, S. Lieb, C. P. Vellano, J. C. O'connell, R. L. Mendes, J. Moll, M. Petronczki, T. P. Heffernan, M. Pearson, D. B. McConnell, N. Kraut, Bi-3406, a potent and

selective sos1–kras interaction inhibitor, is effective in kras-driven cancers through combined mek inhibition. *Cancer Discovery*. **11**, 142–157 (2021).

110. T. Maurer, L. S. Garrenton, A. Oh, K. Pitts, D. J. Anderson, N. J. Skelton, B. P. Fauber, B. Pan, S. Malek, D. Stokoe, M. J. C. Ludlam, K. K. Bowman, J. Wu, A. M. Giannetti, M. A. Starovasnik, I. Mellman, P. K. Jackson, J. Rudolph, W. Wang, G. Fang, Small-molecule ligands bind to a distinct pocket in Ras and inhibit SOS-mediated nucleotide exchange activity. *Proceedings of the National Academy of Sciences*. **109**, 5299–5304 (2012).

111. R. C. Hillig, B. Sautier, J. Schroeder, D. Moosmayer, A. Hilpmann, C. M. Stegmann, N. D. Werbeck, H. Briem, U. Boemer, J. Weiske, V. Badock, J. Mastouri, K. Petersen, G. Siemeister, J. D. Kahmann, D. Wegener, N. Böhnke, K. Eis, K. Graham, L. Wortmann, F. Von Nussbaum, B. Bader, Discovery of potent SOS1 inhibitors that block RAS activation via disruption of the RAS–SOS1 interaction. *Proceedings of the National Academy of Sciences*. **116**, 2551–2560 (2019).

112. D. Kessler, D. Gerlach, N. Kraut, D. B. McConnell, Targeting Son of Sevenless 1: The pacemaker of KRAS. *Current Opinion in Chemical Biology*. **62**, 109–118 (2021).

113. J. L. Bos, H. Rehmann, A. Wittinghofer, GEFs and GAPs: Critical Elements in the Control of Small G Proteins. *Cell*. **129**, 865–877 (2007).

114. J. Gureasko, O. Kuchment, D. L. Makino, H. Sondermann, D. Bar-Sagi, J. Kuriyan, Role of the histone domain in the autoinhibition and activation of the Ras activator Son of Sevenless. *Proceedings of the National Academy of Sciences*. **107**, 3430–3435 (2010).

115. J. Gureasko, W. J. Galush, S. Boykevisch, H. Sondermann, D. Bar-Sagi, J. T. Groves, J. Kuriyan, Membrane-dependent signal integration by the Ras activator Son of sevenless. *Nature Structural and Molecular Biology*. **15**, 452–461 (2008).

116. S. M. Christensen, M. G. Triplet, C. Rhodes, J. S. Iwig, H. L. Tu, D. Stamou, J. T. Groves, Monitoring the Waiting Time Sequence of Single Ras GTPase Activation Events Using Liposome Functionalized Zero-Mode Waveguides. *Nano Letters*. **16**, 2890–2895 (2016).

117. W. C. Lin, L. Iversen, H. L. Tu, C. Rhodes, S. M. Christensen, J. S. Iwig, S. D. Hansen, W. Y. C. Huang, J. T. Groves, H-Ras forms dimers on membrane surfaces via a protein - Protein interface. *Proceedings of the National Academy of Sciences*. **111**, 2996–3001 (2014).

118. J. A. Nye, J. T. Groves, Kinetic control of histidine-tagged protein surface density on supported lipid bilayers. *Langmuir*. **24**, 4145–4149 (2008).

119. W. Y. C. Huang, Q. Yan, W. C. Lin, J. K. Chung, S. D. Hansen, S. M. Christensen, H. L. Tu, J. Kuriyan, J. T. Groves, Phosphotyrosine-mediated LAT assembly on membranes drives kinetic bifurcation in recruitment dynamics of the Ras activator SOS. *Proc Natl Acad Sci U S A*. **113**, 8218–8223 (2016).

120. W. Y. C. Huang, J. A. Ditlev, H. K. Chiang, M. K. Rosen, J. T. Groves, Allosteric Modulation of Grb2 Recruitment to the Intrinsically Disordered Scaffold Protein, LAT, by Remote Site Phosphorylation. *Journal of the American Chemical Society*. **139**, 18009–18015 (2017).

121. N. H. Shah, Q. Wang, Q. Yan, D. Karandur, T. A. Kadlecek, I. R. Fallahee, W. P. Russ, R. Ranganathan, A. Weiss, J. Kuriyan, An electrostatic selection mechanism controls sequential kinase signaling downstream of the T cell receptor. *Elife*. **5** (2016), doi:10.7554/ELIFE.20105.

122. S. J. Plowman, C. Muncke, R. G. Parton, J. F. Hancock, H-ras, K-ras, and inner plasma membrane raft proteins operate in nanoclusters with differential dependence on the actin cytoskeleton. *Proceedings of the National Academy of Sciences*. **102**, 15500–15505 (2005).

123. T. Gurry, O. Kahramanoğullari, R. G. Endres, Biophysical Mechanism for Ras-Nanocluster Formation and Signaling in Plasma Membrane. *PLOS ONE*. **4**, e6148 (2009).

124. D. J. Williamson, D. M. Owen, J. Rossy, A. Magenau, M. Wehrmann, J. J. Gooding, K. Gaus, Pre-existing clusters of the adaptor Lat do not participate in early T cell signaling events. *Nature Immunology 2011 12:7*. **12**, 655–662 (2011).

125. T. Shi, M. Niepel, J. E. McDermott, Y. Gao, C. D. Nicora, W. B. Chrisler, L. M. Markillie, V. A. Petyuk, R. D. Smith, K. D. Rodland, P. K. Sorger, W. J. Qian, H. S. Wiley, Conservation of protein abundance patterns reveals the regulatory architecture of the EGFR-MAPK pathway. *Science Signaling*. **9** (2016).

126. D. B. McAffee, M. K. O'Dair, J. J. Lin, S. T. Low-Nam, K. B. Wilhelm, S. Kim, S. Morita, J. T. Groves, *bioRxiv*, in press, doi:10.1101/2021.12.16.472676.

127. M. L. Dustin, J. T. Groves, Receptor signaling clusters in the immune synapse. *Annual review of biophysics*. **41**, 543–556 (2012).

128. P. J. Halling, Do the laws of chemistry apply to living cells? *Trends in Biochemical Sciences*. **14**, 317–318 (1989).

129. J. T. Groves, S. G. Boxer, Micropattern Formation in Supported Lipid Membranes. *Accounts of Chemical Research*. **35**, 149–157 (2002).

130. F. Reif, *Fundamentals of statistical and thermal physics* (McGraw-Hill, New York, 1965).

131. W. Y. C. Huang, S. Alvarez, Y. Kondo, J. Kuriyan, J. T. Groves, Relating cellular signaling timescales to single-molecule kinetics: A first-passage time analysis of Ras activation by SOS. *Proceedings of the National Academy of Sciences*. **118**, e2103598118 (2021).

132. T. L. To, N. Maheshri, Noise can induce bimodality in positive transcriptional feedback loops without bistability. *Science*. **327**, 1142–1145 (2010).

133. X. Su, J. A. Ditlev, E. Hui, W. Xing, S. Banjade, J. Okrut, D. S. King, J. Taunton, M. K. Rosen, R. D. Vale, Phase separation of signaling molecules promotes T cell receptor signal transduction. *Science*. **352**, 595–599 (2016).

134. M. N. Artyomov, J. Das, M. Kardar, A. K. Chakraborty, Purely stochastic binary decisions in cell signaling models without underlying deterministic bistabilities. *Proceedings of the National Academy of Sciences*. **104**, 18958–18963 (2007).

135. M. Y. Sheinin, M. D. Wang, P. Chem, I. Kaliman, B. Grigorenko, M. Shadrina, A. Nemukhin, D. R. Jackson, J. E. Baker, P. Chem Chem, R. Kumar Das, A. B. Kolomeisky, A. Zemel, A. Mogilner, P. Chem Chem Phys, M. E. Arsenault, Y. Sun, H. H. Bau, Y. E. Goldman, A. W. R Serohijos, D. Tsygankov, S. Liu, T. C. Elston, N. V Dokholyan, F. Posta, M. R. D Orsogna, T. Chou, H. Qian, P.-Z. Shi, J. Xing, S. Walcott, S. X. Sun, A. R. Rogers, J. W. Driver, P. E. Constantinou, D. Kenneth Jamison, M. R. Diehl, A. G. Larson, E. C. Landahl, S. E. Rice, C. Hyeon, S. Klumpp, J. N. Onuchic, Stochastic bifurcation, slow fluctuations, and bistability as an origin of biochemical complexity. *Physical Chemistry Chemical Physics*. **11**, 4861–4870 (2009).

136. S. J. Altschuler, S. B. Angenent, Y. Wang, L. F. Wu, On the spontaneous emergence of cell polarity. *Nature*. **454**, 886–889 (2008).

137. N. Hajicek, N. C. Keith, E. Siraliev-Perez, B. R. S. Temple, W. Huang, Q. Zhang, T. K. Harden, J. Sondek, Structural basis for the activation of plc-γ isozymes by phosphorylation and cancer-associated mutations. *Elife*. **8** (2019), doi:10.7554/ELIFE.51700.

138. O. Vadas, J. E. Burke, X. Zhang, A. Berndt, R. L. Williams, Structural biology structural basis for activation and inhibition of class I phosphoinositide 3-kinases. *Science Signaling*. **4** (2011).

139. S. B. Padrick, M. K. Rosen, Physical Mechanisms of Signal Integration by WASP Family Proteins. *Annual review of biochemistry*. **79**, 707 (2010).

140. M. Turner, D. D. Billadeau, VAV proteins as signal integrators for multi-subunit immune-recognition receptors. *Nature Reviews Immunology*. **2**, 476–486 (2002).

141. H. R. Bourne, O. Weiner, Cell polarity: A chemical compass. *Nature*. **419**, 21–21 (2002).

142. A. J. Ridley, M. A. Schwartz, K. Burridge, R. A. Firtel, M. H. Ginsberg, G. Borisy, J. T. Parsons, A. R. Horwitz, Cell Migration: Integrating Signals from Front to Back. *Science*. **302**, 1704–1709 (2003).

143. P. Friedl, K. Wolf, Tumour-cell invasion and migration: diversity and escape mechanisms. *Nature Reviews Cancer*. **3**, 362–374 (2003).

144. B. Sunchu, C. Cabernard, Principles and mechanisms of asymmetric cell division. *Development (Cambridge)*. **147** (2020), doi:10.1242/DEV.167650/224234.

145. M. N. Rasband, The axon initial segment and the maintenance of neuronal polarity. *Nature Reviews Neuroscience*. **11**, 552–562 (2010).

146. D. Torralba, N. B. Martín-Cófreces, F. Sanchez-Madrid, Mechanisms of polarized cell-cell communication of T lymphocytes. *Immunology Letters*. **209**, 11–20 (2019).

147. A. Nakamasu, G. Takahashi, A. Kanbe, S. Kondo, Interactions between zebrafish pigment cells responsible for the generation of Turing patterns. *Proc Natl Acad Sci U S A*. **106**, 8429–8434 (2009).

148. H. S. Jung, P. H. Francis-West, R. B. Widelitz, T. X. Jiang, S. Ting-Berreth, C. Tickle, L. Wolpert, C. M. Chuong, Local Inhibitory Action of BMPs and Their Relationships with Activators in Feather Formation: Implications for Periodic Patterning. *Developmental Biology*. **196**, 11–23 (1998).

149. S. Sick, S. Reinker, J. Timmer, T. Schlake, WNT and DKK determine hair follicle spacing through a reaction-diffusion mechanism. *Science*. **314**, 1447–1450 (2006).

150. J. Raspopovic, L. Marcon, L. Russo, J. Sharpe, Digit patterning is controlled by a Bmp-Sox9-Wnt Turing network modulated by morphogen gradients. *Science*. **345**, 566–570 (2014).

151. R. Sheth, L. Marcon, M. F. Bastida, M. Junco, L. Quintana, R. Dahn, M. Kmita, J. Sharpe, M. A. Ros, Hox genes regulate digit patterning by controlling the wavelength of a turing-type mechanism. *Science*. **338**, 1476–1480 (2012).

152. V. Castets, E. Dulos, J. Boissonade, P. De Kepper, Experimental evidence of a sustained standing Turing-type nonequilibrium chemical pattern. *Physical Review Letters*. **64**, 2953 (1990).

153. Q. Ouyang, H. L. Swinney, Transition from a uniform state to hexagonal and striped Turing patterns. *Nature*. **352**, 610–612 (1991).

154. J. Horváth, I. Szalai, P. De Kepper, An experimental design method leading to chemical turing patterns. *Science*. **324**, 772–775 (2009).

155. M. Loose, E. Fischer-Friedrich, J. Ries, K. Kruse, P. Schwille, Spatial regulators for bacterial cell division self-organize into surface waves in vitro. *Science*. **320**, 789–92 (2008).

156. Y. Liu, W. C. Lo, Deterministic and stochastic analysis for different types of regulations in the spontaneous emergence of cell polarity. *Chaos, Solitons & Fractals*. **144**, 110620 (2021).

157. A. Jilkine, S. B. Angenent, L. F. Wu, S. J. Altschuler, A Density-Dependent Switch Drives Stochastic Clustering and Polarization of Signaling Molecules. *PLOS Computational Biology*. **7**, e1002271 (2011).

158. D. Karig, K. Michael Martini, T. Lu, N. A. DeLateur, N. Goldenfeld, R. Weiss, Stochastic Turing patterns in a synthetic bacterial population. *Proc Natl Acad Sci U S A*. **115**, 6572–6577 (2018).

159. T. Butler, N. Goldenfeld, Fluctuation-driven Turing patterns. *Physical Review E - Statistical, Nonlinear, and Soft Matter Physics*. **84**, 011112 (2011).

160. M. Pablo, S. A. Ramirez, T. C. Elston, Particle-based simulations of polarity establishment reveal stochastic promotion of Turing pattern formation. *PLOS Computational Biology*. **14**, e1006016 (2018).

161. M. J. Lawson, B. Drawert, M. Khammash, L. Petzold, T. M. Yi, Spatial Stochastic Dynamics Enable Robust Cell Polarization. *PLOS Computational Biology*. **9**, e1003139 (2013).

162. S. J. Altschuler, S. B. Angenent, Y. Wang, L. F. Wu, On the spontaneous emergence of cell polarity. *Nature*. **454**, 886–889 (2008).

163. R. J. Petrie, K. M. Yamada, At the leading edge of three-dimensional cell migration. *Journal of Cell Science*. **125**, 5917–5926 (2012).

164. J. Gureasko, W. J. Galush, S. Boykevisch, H. Sondermann, D. Bar-Sagi, J. T. Groves, J. Kuriyan, Membrane-dependent signal integration by the Ras activator Son of sevenless. *Nature Structural & Molecular Biology*. **15**, 452–461 (2008).

165. Y. Arai, T. Shibata, S. Matsuoka, M. J. Sato, T. Yanagida, M. Ueda, Self-organization of the phosphatidylinositol lipids signaling system for random cell migration. *Proc Natl Acad Sci U S A*. **107**, 12399–404 (2010).

166. M. Ziman, D. Preuss, J. Mulholland, J. M. O'Brien, D. Botstein, D. I. Johnson, Subcellular localization of Cdc42p, a Saccharomyces cerevisiae GTP-binding protein involved in the control of cell polarity. *Molecular Biology of the Cell*. **4**, 1307–1316 (1993).

167. Á. Román-Fernández, J. Roignot, E. Sandilands, M. Nacke, M. A. Mansour, L. McGarry, E. Shanks, K. E. Mostov, D. M. Bryant, The phospholipid PI(3,4)P2 is an apical identity determinant. *Nature Communication*. **9**, 1–17 (2018).

168. R. E. Redfern, D. Redfern, M. L. M. Furgason, M. Munson, A. H. Ross, A. Gericke, PTEN phosphatase selectively binds phosphoinositides and undergoes structural changes. *Biochemistry*. **47**, 2162–2171 (2008).

169. A. Edelstein, N. Amodaj, K. Hoover, R. Vale, N. Stuurman, *Current Protocols in Molecular Biology*, in press, doi:10.1002/0471142727.MB1420S92.

170. M. Akkouchi, ON THE CONVOLUTION OF EXPONENTIAL DISTRIBUTIONS. *Journal of the Chungcheong Mathematical Society*. **21**, 501–510 (2008).

171. Q. Yan, T. Barros, P. R. Visperas, S. Deindl, T. A. Kadlecek, A. Weiss, J. Kuriyan, Structural Basis for Activation of ZAP-70 by Phosphorylation of the SH2-Kinase Linker. *Molecular and Cellular Biology*. **33**, 2188–2201 (2013).

172. M. A. Seeliger, M. Young, M. N. Henderson, P. Pellicena, D. S. King, A. M. Falick, J. Kuriyan, High yield bacterial expression of active c-Abl and c-Src tyrosine kinases. *Protein Science*. **14**, 3135–3139 (2005).

173. M. Tormen, E. Sovernigo, A. Pozzato, M. Pianigiani, M. Tormen, Sub-100 μs nanoimprint lithography at wafer scale. *Microelectronic Engineering*. **141**, 21–26 (2015).

174. A. D. Edelstein, M. A. Tsuchida, N. Amodaj, H. Pinkard, R. D. Vale, N. Stuurman, Advanced methods of microscope control using μManager software. *Journal of Biological Methods*. **1**, e10 (2014).

175. J. Wu, A. Pipathsouk, A. Keizer-Gunnink, F. Fusetti, W. Alkema, S. Liu, S. Altschuler, L. Wu, A. Kortholt, O. D. Weiner, Homer3 regulates the establishment of neutrophil polarity. *Molecular Biology of the Cell*. **26**, 1629–1639 (2015).

APPENDIX A

Material and Methods for Chapter 2

Protein purification

PTEN

PTEN was cloned from PET30B-PTEN (PET30B-PTEN was a gift from Alonzo Ross (Addgene plasmid # 20741)(*168*). PTEN in-frame with a N-terminal his6-MBP-(Asn)10-TEV-GGGGG was transformed into BL21(DE3) expression cells, and these cells were grown overnight at 37ºC in TB medium supplemented with kanamycin (50µg/mL). The overnight culture was then diluted 1:100 (v/v) into fresh TB medium supplemented with kanamycin (50µg/mL), and was allowed to grow to OD600 of 0.6~0.8. Protein expression was induced with 0.1mM isopropyl β-D-1-thiogalactopyranoside (IPTG) and incubated at 18ºC 200rpm overnight. Bacterial cells were collected by centrifugation at 3000 rpm, resuspended in Lysis buffer (50 mM Na_2HPO_4 (pH 8.0), 300 mM NaCl, 0.4 mM BME, 1 mM PMSF, 100 µg/mL DNase) and homogenized using a microfluidizer. Cell debris was removed by centrifugation at 16,000 rpm at 4°C for 60 minutes, and the supernatant was incubated with Ni-nitrilotriacetate resin (Thermo Scientific HisPur Ni-NTA Resin) at 4°C for 1 hour. The resin was subsequently loaded into a gravity column, washed with Wash buffer (50 mM Na_2HPO_4 (pH 8.0), 300 mM NaCl, 1 mM BME, 20 mM imidazole), and eluted with Elution buffer (50 mM Na_2HPO_4 (pH 8.0), 300 mM NaCl, 1 mM BME, 500 mM imidazole). Peak fractions were pooled, combined with 200 µg/mL his6-TEV(S291V) protease, and dialyzed against 4 liters Dialysis buffer (20 mM Tris (pH 7.4), 200 mM NaCl, 1 mM BME) for 16-18 hours at 4°C. Precipitation was removed by centrifugation and 0.22 µm syringe filtration. The dialysate was then bound to a MonoQ anion exchange column (GE Healthcare) equilibrated in 20 mM Tris (pH 7.4), 100 mM NaCl, 1 mM BME. Proteins were resolved over a 10-100% linear gradient (0.1-1 M NaCl, 45 CV, 45 mL total, 1 mL/min flow rate). The elution fractions containing the recombinant protein were combined and concentrated in a 5 kDa MWCO Vivaspin 20 centrifuge tube (GE Healthcare). The concentration of protein was determined by measuring OD280 (ext. coefficient 45270.00 $M^{-1}cm^{-1}$) using nanodrop, and the protein solution was flash-frozen in liquid nitrogen and stored at -80ºC.

$PTEN_{\Delta PBD}$

PTEN(16-403) in-frame with an N-terminal his6-MBP-(Asn)10-TEV-GGGGG was transformed into BL21(DE3) expression cells, and these cells were grown overnight at 37ºC in TB medium supplemented with kanamycin (50µg/mL). The overnight culture was then diluted 1:100 (v/v) into fresh TB medium supplemented with kanamycin (50µg/mL), and was allowed to grow to OD600 of 0.6~0.8. Protein expression was induced with 0.1mM isopropyl β-D-1-thiogalactopyranoside (IPTG) and incubated at 18ºC 200rpm overnight. Bacterial cells were collected by centrifugation at 3000 rpm, resuspended in Lysis buffer (50 mM Na_2HPO_4 (pH 8.0), 300 mM NaCl, 0.4 mM BME, 1 mM PMSF, 100 µg/mL DNase) and homogenized using a microfluidizer. Cell debris was removed by centrifugation at 16,000 rpm at 4°C for 60 minutes, and the supernatant was incubated with Ni-nitrilotriacetate resin (Thermo Scientific HisPur Ni-NTA Resin) at 4°C for 1 hour. The resin was subsequently loaded into a gravity column, washed with Wash buffer (50 mM Na_2HPO_4 (pH 8.0), 300 mM NaCl, 1 mM BME, 20 mM imidazole), and eluted with Elution buffer (50 mM Na_2HPO_4 (pH 8.0), 300 mM NaCl, 1 mM BME, 500 mM imidazole). Peak fractions were pooled, combined with 200 µg/mL his6-TEV(S291V) protease, and dialyzed against 4 liters Dialysis buffer (20 mM Tris (pH 7.4), 200 mM NaCl, 1 mM BME) for 16-18 hours at 4°C. Precipitation was removed by centrifugation and 0.22 µm syringe filtration. The dialysate was then bound to a MonoQ anion exchange column (GE Healthcare) equilibrated in 20 mM Tris (pH 7.4), 100 mM NaCl, 1 mM BME. Proteins were

resolved over a 10-100% linear gradient (0.1-1 M NaCl, 45 CV, 45 mL total, 1 mL/min flow rate). The elution fractions containing the recombinant protein were combined and concentrated in a 5 kDa MWCO Vivaspin 20 centrifuge tube (GE Healthcare), and subsequently pass through a 24 mL Superdex 200 10/300 GL (GE Healthcare) size exclusion column equilibrated in 20 mM Tris [pH 8.0], 200 mM NaCl, 10% glycerol, 1 mM TCEP. Peak fractions were pooled and concentrated. The concentration of protein was determined by measuring OD280 (ext. coefficient 45270.00 $M^{-1}cm^{-1}$) using nanodrop, and the protein solution was flash-frozen in liquid nitrogen and stored at -80ºC.

PTEN-DrrA

his6-MBP-(Asn)10-TEV-GGGGG-PTEN in frame with a C-terminal $(GGS)_3GG$-DrrA(544-647) was transformed into BL21(DE3) expression cells, and these cells were grown overnight at 37ºC in TB medium supplemented with kanamycin (50µg/mL). The overnight culture was then diluted 1:100 (v/v) into fresh TB medium supplemented with kanamycin (50µg/mL), and was allowed to grow to OD600 of 0.6~0.8. Protein expression was induced with 0.1mM isopropyl β-D-1-thiogalactopyranoside (IPTG) and incubated at 18ºC 200rpm overnight. Bacterial cells were collected by centrifugation at 3000 rpm, resuspended in Lysis buffer (50 mM Na_2HPO_4 (pH 8.0), 300 mM NaCl, 0.4 mM BME, 1 mM PMSF, 100 µg/mL DNase) and homogenized using a microfluidizer. Cell debris was removed by centrifugation at 16,000 rpm at 4°C for 60 minutes, and the supernatant was incubated with Ni-nitrilotriacetate resin (Thermo Scientific HisPur Ni-NTA Resin) at 4°C for 1 hour. The resin was subsequently loaded into a gravity column, washed with Wash buffer (50 mM Na_2HPO_4 (pH 8.0), 300 mM NaCl, 1 mM BME, 20 mM imidazole), and eluted with Elution buffer (50 mM Na_2HPO_4 (pH 8.0), 300 mM NaCl, 1 mM BME, 500 mM imidazole). Peak fractions were pooled, combined with 200 µg/mL his6-TEV(S291V) protease, and dialyzed against 4 liters Dialysis buffer (20 mM Tris (pH 7.4), 200 mM NaCl, 1 mM BME) for 16-18 hours at 4°C. Precipitation was removed by centrifugation and 0.22 µm syringe filtration. The dialysate was then bound to a MonoQ anion exchange column (GE Healthcare) equilibrated in 20 mM Tris (pH 7.4), 100 mM NaCl, 1 mM BME. Proteins were resolved over a 10-100% linear gradient (0.1-1 M NaCl, 45 CV, 45 mL total, 1 mL/min flow rate). The elution fractions containing the recombinant protein were combined and concentrated in a 5 kDa MWCO Vivaspin 20 centrifuge tube (GE Healthcare), and subsequently pass through a 24 mL Superdex 200 10/300 GL (GE Healthcare) size exclusion column equilibrated in 20 mM Tris [pH 8.0], 200 mM NaCl, 10% glycerol, 1 mM TCEP. Peak fractions were pooled and concentrated. The concentration of protein was determined by measuring OD280 (ext. coefficient 45270.00 $M^{-1}cm^{-1}$) using nanodrop, and the protein solution was flash-frozen in liquid nitrogen and stored at -80ºC.

$OCRL_{PD}$ & DrrA-$OCRL_{PD}$

$OCRL_{PD}$ (234-539aa) & DrrA-OCRLPD was purified as previously described(*6*).

Alexa488-$PLC\delta_{PH}$ & Cy3-DrrA

PLCδ PH domain (11-140) and DrrA(544-647) were purified as previously described. Sortase mediated protein labeling was performed with either NHS-Alexa488 labeled LEPTGG peptide and NHS-Cy3 labeled LEPTGG as previously described(*6*).

$PIP5K_{KD}$

$PIP5K_{KD}$ (PIP5K1B 1-421aa) was purified as previously described(*6*).

Ras, SOS_{cat}, SOS_{HDPC} and p120GAP

H-Ras (1-181, C118S) (human H-Ras protein with residues 1-181 and a point mutation to serine at residue C118), SOS_{cat} (566-1049), SOS_{HDPC} (1-1049), and the GAP domain of p120GAP (714-1047), were expressed and purified based on the protocols described in previous work(*74*, *115*).

Alexa647-RBD(K65E)

RBD (56-131; K65E) derived from the Raf-1 human gene was purified and labeled with Alexa647-maleimide using previously reported methods(*44*).

Preparation of liposome

Lipids used: 1,2-dioleoyl-sn-glycero-3-phosphocholine (DOPC), L-α-phosphatidylinositol-4-phosphate (Brain PI(4)P), L-α-phosphatidylinositol-4,5-bisphosphate (Brain $PI(4,5)P_2$), 1,2-dioleoyl-sn-glycero-3-phosphoethanolamine-N-[4-(pmaleimidomethyl)cyclohexanecarboxamide] (MCC-PE), 1,2-dioleoyl-sn-glycero-3-phospho-L-serine (DOPS), 1,2-dioleoyl-sn-glycero-3-phosphoethanolamine-N-(cap biotinyl) (Biotin-DOPE) were purchased from Avanti Polar Lipids. D-myo-Phosphatidylinositol 3,4,5-trisphosphate ($PI(3,4,5)P_3$), D-myo-Phosphatidylinositol 3,4-bisphosphate ($PI(3,4)P_2$) were purchased from Echelon Biosciences Inc.. Texas Red 1,2-dihexadecanoylsnglycero-3-phosphoethanolamine (TR-DHPE) was purchased from Invitrogen.

Lipids were mixed in a glass round bottom flask cleaned by piranha etching at the desired molar fraction. The solution was then evaporated using a rotary evaporator for 10 min at 35°C or until dried to a thin film. Dried lipid films were further blow-dried with N_2 for at least 30 min. Lipids were resuspended in Milli-Q H_2O by shaking and gently pipetting to form a solution with a final concentration of 1 mM total lipids. For liposome assays, the lipid solution was first freeze-thawed three times in liquid nitrogen. To generate small unilamellar vesicles (SUV) with the desired size, the solution was extruded through a polycarbonate membrane (Avanti Polar Lipids) with the desired pore size 11 times. The size distribution was checked by dynamic light scattering. SUV for the formation of supported lipid bilayer was prepared by sonication for 100 sec (20 sec on, 30sec off for 5 times) in an ice-water bath.

Phosphatase assay

Phosphate Sensor (Thermo Fisher Scientific PV4406) was diluted to 2μM in TBS. 50 μL of liposomes were mixed with 25 μL of 2μM Phosphate Sensor in a 96-well plate. The background fluorescence of liposome mixed with phosphate sensor was taken as baseline. 25 μL of 40 nM PTEN was added into the 96-well plate to initiate the reaction. The fluorescent was detected in a microplate reader (BioTek) at excitation 485 (10) nm and emission 530 (10) nm with 30 seconds intervals, including 5 seconds of shaking before reading. A calibration curve for phosphate concentration was established using a phosphate standard from 10 pM to 100 nM and fitted to a binding curve. Initial velocity was obtained by fitting the initial linear region of the reaction trace. Initial velocity was plotted against SUV concentration, and fitted to Michaelis-Menten kinetics using $v = \frac{kcat[E][S]}{K_M+[S]}$ in Graphpad Prism. Apparent catalytic efficiency is obtained by calculating k_{cat}/K_M.

Microscope hardware and imaging acquisition

Fluorescence confocal microscopy was performed on Nikon Eclipse Ti inverted microscope with Yokogawa CSU-X spinning disk module. The light sources were diode lasers at 488, 561, and 640 nm (Coherent, Santa Clara, CA), and imaged by EMCCD (Andor Technology Ltd., UK) using a 100x Nikon objective (1.49 NA) oil immersion TIRF objective. TIRF imaging experiments were performed on an inverted Nikon Eclipse Ti microscope using either a 100x Nikon objective (1.49 NA) oil immersion TIRF objective or a 60x Apo TIRF oil immersion objective (1.45 NA). The light sources were either a 488 nm, 561 nm, or 637 nm diode laser (OBIS laser diode, Coherent, Santa Clara, CA) controlled with a custom built Solemere (Salt Lake City, Utah) laser driver with analog and digital modulation (0-5 volts). Images were acquired on an EMCCD camera (Andor Technology Ltd., UK). All microscope hardware was controlled using Micro-Manager v4.0(*169*). Samples were excited with 0.3~0.8 mW laser power at the objective. The exposure time is typically 100~200 ms. The imaging frame rate is typically 0.1 Hz.

Membrane coated beads experiments

200 uL of 10% slurry of Silica beads (Bangs Laboratories) were transferred to a glass vial. The beads were etched with piranha solution for 20 mins. The solution was diluted with water slowly on ice, then the beads were spun down by centrifugation in a swing bucket rotor at 1000 rcf for 5 min. The supernatant was removed by a glass pipette. The remaining beads were washed three times by water, then transferred to an Eppendorf tube. The beads were washed three times again in PBS. Finally, the beads were suspended in 200 uL of TBS. 20 uL of beads were mixed with 200 uL of PBS and 200 uL of 1 mM SUV solution (containing 96.5% DOPC, 2% PI(3,4,5)P_3, 1% Biotin-DOPE, 0.5% TR-DHPE) and incubated for 30 min with constant rotation. Then the beads were washed with PBS three times. Supported lipid bilayer coated beads were used for experiments immediately.

25x75 mm glass coverslips (Ibidi 10812) were etched with piranha solution for 5 minutes and rinsed with water extensively. The coverslip were dried with blowing nitrogen gas and stick to a flow chamber (Ibidi µ-Slide 80608). 100 uL of 1 mg/ml Biotin-BSA was introduced into the flow channel. After 30 min, the remaining Biotin-BSA was washed out with 1 mL of PBS. Blocking was performed with 0.05 mg/ml neutravidin was subsequently added. After 30 min, the remaining Biotin-BSA was washed out with 1 mL of PBS. Membrane coated beads were added into the flow chamber and allowed to settle and bind to the neutravidin on the glass surface to achieve the desired density. Excessive beads were gently washed out using 1 mL PBS before imaging using a spinning disk confocal. Reaction was performed in a buffer containing 20 mM Tris (pH 7.4), 150 mM NaCl, 100 µg/mL beta casein, 5 mM BME, 2 mM UV-treated Trolox ((±)-6-Hydroxy-2,5,7,8-tetramethylchromane-2-carboxylic acid), 320 µg/mL glucose oxidase, 50 µg/mL catalase, and 20 mM glucose.

Microfabrication

25x75 mm glass coverslips (Ibidi 10812) were cleaned in acetone by sonication, then washed with MilliQ water extensively. The coverslips were dried with nitrogen gas then baked on 120°C hot plate for 5 minutes. S1805 positive photoresist (Dow Chemical)) was spin-coated on the coverslips by spinning for 2 seconds at 500 rpm (acceleration 440 rpm/s) then for 30 seconds at 4111 rpm (acceleration 3900 rpm/s). The photoresist on the edge of the coverslips was removed by cotton swab soaked with acetone, then baked on 120°C hot plate for 1 minute. Mask with the desired pattern was mounted on an OAI Series 200 Aligner. The photoresist coated coverslip was exposed for 0.6 sec with UV power around 30 mW/cm^2, then developed with MicroPosit MF-321 Liquid Developr (Dow Chemical) for 40 sec with mild shaking. The

developed coverslips were rinsed with water and dried with nitrogen gas. ~9 nm thick chromium was subsequently deposited on the coverslips using an electron beam evaporator at $1x10^{-6}$ torr. The photoresist is lifted from chromium patterned glass substrates by bath sonication in MicroPosit Remover 1165 (Dow Chemical) for 10 minutes for 2 times then washed with abundant water.

Supported lipid bilayer experiments

Glass coverslips with chromium patterns were etched with piranha solution for 5 minutes and then rinsed with water extensively. The coverslip was rapidly dried with nitrogen gas and stick to a flow chamber (Ibidi µ-Slide 80608). SLBs were formed on a glass substrate by flowing around 150 µL of 0.25 mM SUVs diluted in PBS (pH 7.2) into the chamber and incubated for at least 30 min. After incubation, the chambers were washed with 1 mL of PBS and then blocked with 1 mg/mL β-casein (Thermo Fisher Scientific 37528) for 10 min. The chambers were then rinsed with 1 mL PBS buffer. PTEN reactions were performed in a buffer containing 20 mM Tris (pH 7.4), 150 mM NaCl, 100 µg/mL beta casein, 5 mM BME, 2 mM UV-treated Trolox, 320 µg/mL glucose oxidase, 50 µg/mL catalase, and 20 mM glucose, with the addition of 20 nM of either Alexa488-PLCδ_{PH} or Cy3-DrrA to monitor the reaction. Fitting to Hill equation is performed in GraphPad Prism with the equation form: $Y = A \times \frac{X^H}{B^H + X^H}$.

For PIP5K and OCRL reactions, SUV containing either 96% DOPC, 2% PI(4,5)P_2, 2% PI(4)P, or 96% DOPC, 4% PI(4)P was used. Reactions were performed in a buffer containing 20 mM HEPES (pH 7.0), 150 mM NaCl, 1 mM ATP, 5 mM $MgCl_2$, 0.5 mM EGTA, 200 µg/mL beta casein, 20 mM BME, and 20 mM glucose, with the addition of 20 nM Alexa488-PLCδPH and 20 nM Cy3-DrrA to monitor the reaction.

For Ras reactions, SUV containing 96% DOPC, 2% PI(4,5)P_2, 2% MCC-DOPE were used to form supported lipid bilayer. H-Ras was incubated at 1 mg/mL for 2 hr 30 min in PBS buffer at room temperature. After washing with 1 mL PBS, 5 mM BME was then added to quench the reaction. After 10 min, the flow channel was washed with 1 mL of PBS, and buffer exchanged into 40 mM HEPES (pH 7.4), 100 mM NaCl, 5 mM $MgCl_2$, 100 µM GDP. GDP was washed away with 40 mM HEPES (pH 7.4), 100 mM NaCl, 5 mM $MgCl_2$, 10 mM BME immediately before reaction. Ras reactions were performed in a buffer containing 40 mM HEPES (pH 7.4), 100 mM NaCl, 5 mM $MgCl_2$, 10 mM BME, 100 µM GTP, 2 mM UV-treated Trolox, 320 µg/mL glucose oxidase, 50 µg/mL catalase, and 20 mM glucose, with the addition of 10 nM Alexa647-RBD(K65E) to monitor the reaction.

Stochastic simulations

The time evolution of all species in the reaction was simulated stochastically using the Gillespie algorithm. Within the reaction space, the membrane composition was approximated to be spatially homogeneous. The simulation was performed in MATLAB according to the kinetic scheme in Figure 5A. We approximated the solution concentration of E_0, ρ_{E0}, be constant since in the experiment there is a large solution reservoir. Each molecular species is expressed as the exact number of molecules. The rate for each transition is calculated as:

$E_0 \rightarrow E_1$; $\quad r_1 = k_{on} \cdot \rho_{E0} \cdot \sigma_P \cdot A.$

$E_1 \rightarrow E_0$; $\quad r_2 = k_{off} \cdot \sigma_{E1} \cdot A.$

$E_1 + S \rightarrow E_1S$; $\quad r_3 = k_f \cdot \sigma_{E1} \cdot \sigma_S \cdot A$

$E_1S \rightarrow E_1 + S\,; \quad r_4 = k_r \cdot \sigma_{E1S} \cdot A$

$E_1S \rightarrow E_1 + P\,; \quad r_5 = k_{cat} \cdot \sigma_{E1S} \cdot A$

A is the area of the membrane in μm^2, and the surface density of each membrane associated species, σ_x, is expressed as discrete molecular copy number per unit area. We used the following rate parameters:

$k_{on} \cdot \rho_{E0} = 0.0001\ t^{-1}$ (ρ_{E0} taken as constant for infinite solution reservoir.)

$k_{off} = 0.1\ t^{-1}$

$k_f = 0.005\ \mu m^2 t^{-1}$

$k_r = 1\ t^{-1}$

$k_{cat} = 50\ t^{-1}$

The kinetic parameters used are within similar ranges with reported kinetic rate constants for PTEN (26). All simulations begin with 26600/μm^2 substrate and 1400/ μm^2 product (corresponding to 1.9% molar fraction of substrate and 0.1% molar fraction of product on the membrane) unless otherwise stated. This initial condition is used since in our simple model enzyme recruitment to the membrane is strictly through binding to product. For any enzyme to be recruited to the membrane, some product is required to "seed" the reaction in the simulation. This is to mimic the initial enzyme catalysis from the solution that starts the reaction, without introducing unnecessary complexity to the model. Simulations of 1 μm^2 and 0.25 μm^2 were used to mimic large- and small-scale membrane reactions, respectively. We note that a larger area difference amplifies any scale dependence in the simulations, though larger reactions require significantly more computation time. Statistics were collected from 1000 simulations.

For the reaction case that has no positive feedback, the $E_0 \rightarrow E_1$ rate is modified to be independent of σ_P:

$E_0 \rightarrow E_1; \qquad r_1 = k_{on} \cdot \rho_{E0} \cdot A.$

The rate parameters used are:

$k_{on} \cdot \rho_{E0} = 1.4\ t^{-1}$

$k_{off} = 0.1\ t^{-1}$

$k_f = 0.005\ \mu m^2 t^{-1}$

$k_r = 1\ t^{-1}$

$k_{cat} = 50\ t^{-1}$

For the reaction case that is fixed at steady state, the kinetic parameters used are:

$k_{on} \cdot \rho_{E0} = 0.0001\ t^{-1}$

$k_{off} = 0.1\ t^{-1}$

$k_f = 0.005\ \mu m^2 t^{-1}$

$k_r = 1\ t^{-1}$

$k_{cat} = 50\ t^{-1}$

Simulations begin with 14000/μm^2 substrate and 14000/ μm^2 product (corresponding to 1% molar fraction of substrate and 1% molar fraction of product on the membrane) and the densities are fixed. The formed product from the reaction is recorded separately to calculate the reaction velocity. The simulation was performed until the numbers reach a steady state. Then the reaction was allowed to run for an extended time and recorded.

For the reaction case with near-equilibrium enzyme binding, either the k_{on} and k_{off} are changed to:

$k_{on} \cdot \rho_{E0} = 0.01\ t^{-1}$

$k_{off} = 10\ t^{-1}$

Or k_f and k_{cat} are changed to:

$k_f = 0.0001\ \mu m^2 t^{-1}$

$k_{cat} = 1\ t^{-1}$

For the reaction case with near-equilibrium enzyme binding at low substrate density, simulations begin with 76/μm^2 substrate and 4/μm^2 product. Either the k_{on} and k_{off} are changed to:

$k_{on} \cdot \rho_{E0} = 0.01\ t^{-1}$

$k_{off} = 10\ t^{-1}$

Or k_{on}, k_f and k_{cat} are changed to:

$k_{on} \cdot \rho_{E0} = 0.02\ t^{-1}$

$k_f = 0.0001\ \mu m^2 t^{-1}$

$k_{cat} = 1\ t^{-1}$

For the reaction case with the incorporation of catalysis from solution by random collision of the enzyme with the membrane, we have included additional reactions:

$E_0 + S \rightarrow E_0S; \quad r_6 = k_{f2} \cdot \rho_{E0} \cdot \sigma_s \cdot A$

$E_0S \rightarrow E_0 + S; \quad r_7 = k_r \cdot \sigma_{E0S} \cdot A$

$E_0S \rightarrow E_0 + P; \quad r_8 = k_{cat} \cdot \sigma_{E0S} \cdot A$

$k_{f2} \cdot \rho_{E0} = 0.003\ t^{-1}$ (ρ_{E0} taken as constant for infinite solution reservoir.).

Simulations begin with 28000/μm^2 substrate and 0/μm^2 product.

Deterministic simulations

Deterministic simulations were done by numerically solving coupled kinetic equations in MATLAB. Densities are evaluated as number of molecules per μm^2 and the solution enzyme concentration, ρ_{E0}, is constant. The rate equations are:

$$\frac{d\sigma_{E1}}{dt} = k_{on} \cdot \rho_{E0} \cdot \sigma_P - k_{off} \cdot \sigma_{E1} - k_f \cdot \sigma_{E1} \cdot \sigma_S + k_r \cdot \sigma_{E1S} + k_{cat} \cdot \sigma_{E1S}$$

$$\frac{d\sigma_{E1S}}{dt} = k_f \cdot \sigma_{E1} \cdot \sigma_S - k_r \cdot \sigma_{E1S} - k_{cat} \cdot \sigma_{E1S}$$

$$\frac{d\sigma_P}{dt} = k_{cat} \cdot \sigma_{E1S} - k_{on} \cdot \rho_{E0} \cdot \sigma_P + k_{off} \cdot \sigma_{E1}$$

$$\frac{d\sigma_S}{dt} = -k_f \cdot \sigma_{E1} \cdot \sigma_S + k_r \cdot \sigma_{E1S}$$

The rate constants are:

$k_{on} \cdot \rho_{E0} = 0.0001\ t^{-1}$

$k_{off} = 0.1\ t^{-1}$

$k_f = 0.005\ \mu m^2 t^{-1}$

$k_r = 1\ t^{-1}$

$k_{cat} = 50\ t^{-1}$

Simulations begin with 26600/μm^2 substrate and 1440/μm^2 product (corresponding to 1.9% molar fraction of substrate and 0.1% molar fraction of product on the membrane).

Analytical model for surface adsorption

In terms of a continuum description with deterministic chemical kinetic rate equations, the surface density of adsorbed molecules, σ, from an infinite solution reservoir follows the rate equation:

$$\frac{d\sigma}{dt} = k\sigma^m$$

where *k* is a constant and *m* represents the order of positive feedback (e.g. *m* = 0 for no feedback, *m* = 1 for linear feedback, etc.). In this continuum description, the time for density doubling from σ_0 to $2\sigma_0$ (τ_D) can be obtained by integrating the rate equation:

$$\tau_D = \frac{1}{k}\int_{\sigma_0}^{2\sigma_0} \frac{1}{\sigma^m} d\sigma$$

Taking a stochastic approach, the process of density doubling consists of a Markov chain of *n* molecular adsorption events (copy number *n* molecules goes to 2*n*), each with defined transition rates. We consider

systems with different initial copy numbers of molecules, n, and correspondingly different areas, A_n, at equivalent initial surface density to examine system size specific effects. For a system starting with n molecules the i^{th} transition has rate $k\sigma^m A_n$, where $\sigma = (n + i - 1)/A_n$ is the momentary density of adsorbed molecules while waiting for the i^{th} transition event. The waiting time distribution at each step is given by $p_i(\tau_i) = \beta_i e^{-\beta_i \tau_i}$ where $\beta_i \equiv k\sigma^m A_n$ and $\langle \tau_i \rangle = \int_0^\infty \tau_i p_i(\tau_i) d\tau_i = 1/\beta_i$ The full probability distribution for τ_D, resulting from successive convolution of the individual transition time probability distributions can be expressed in closed form as(*170*):

$$p(\tau_D) = \sum_{i=1}^{n} \frac{\beta_1 \cdots \beta_n}{\prod_{\substack{j=1 \\ j \neq i}}^{n} (\beta_j - \beta_i)} e^{-\beta_i \tau_D}$$

Since the delay time probability distributions for each of the transitions are independent, the mean doubling time, equivalent to MFPT for this one-way process, can be calculated directly from the individual mean delay times, $\langle \tau_D \rangle = \sum_{i=1}^{n} \langle \tau_i \rangle$, without need for the full distribution.

APPENDIX B

Material and Methods for Chapter 3

Materials and Methods

Protein purification

SOS and SOS^{CatPR} (533–1333) were purified based on protocols described in previous work(*44*). H-Ras (1-181, C118S) (human H-Ras protein with residues 1-181 and a point mutation to serine at residue C118), SOS^{Cat} (566-1049), SOS^{HDPC} (1-1049) were purified based on previous reports(*115*). The GAP domain of p120GAP (714-1047), were expressed and purified based on the protocols described in previous work(*74*). RBD (56-131; K65E) derived from the Raf-1 human gene was purified and labeled with Alexa647-maleimide using previously reported methods(*44*). LAT (30-233) and Grb2 were purified and labeled following previously described protocols(*44*, *171*). Hck were purified based on published protocols(*172*).

Preparation of liposome

Lipids used: 1,2-dioleoyl-sn-glycero-3-phosphocholine (DOPC), L-α-phosphatidylinositol-4,5-bisphosphate (Brain $PI(4,5)P_2$), 1,2-dioleoyl-sn-glycero-3-[(N-(5-amino-1-carboxypentyl)iminodiacetic acid)succinyl] (nickel salt) (Ni-DGS), 1,2-dioleoyl-sn-glycero-3-phosphoethanolamine-N-[4-(pmaleimidomethyl)cyclohexanecarboxamide] (MCC-PE) were purchased from Avanti Polar Lipids. Lipids were mixed in a glass round bottom flask cleaned by piranha etching at the desired molar fraction. The solution was then evaporated using a rotary evaporator for 10 min at 35°C or until dried to a thin film. Dried lipid films were further blow-dried with N_2 for at least 10 min. Lipids were resuspended in Milli-Q H_2O by shaking and gently pipetting to form a solution with a final concentration of 1 mM total lipids. Small unilamellar vesicles (SUV) for the formation of supported lipid bilayer was prepared by sonication for 100 sec (20 sec on, 30sec off for 5 times) in an ice-water bath.

Microfabrication

Chromium patterns (100 nm thick and 5 nm high) were fabricated onto 25x75 mm glass coverslips by the Pulsed Nanoimprint Lithography method (Pulsed NIL) (ThunderNIL Srl, Italy) (*173*). Briefly, a stamp with desired patterns was fabricated by electron beam lithography, and was treated with hydrophobic trichlorosilanes to make it non-adhesive. Pulsed NIL was performed on glass substrates, which were previously spin coated with 120 nm thick mr-l 7010 resist, using the stamp. Residual resist film on the glass substrate was etched off using oxygen plasma before the chromium lift-off process.

Supported lipid bilayer experiments

Glass coverslips with chromium patterns were etched with piranha solution for 5 minutes and then rinsed with water extensively. The coverslip was blow dried with nitrogen gas and immediately stick to a flow chamber (Ibidi µ-Slide 80608). SLBs were formed on a glass substrate by flowing around 150 µL of 0.25 mM SUVs diluted in PBS (pH 7.2) into the chamber and incubated for at least 30 min. After incubation,

the chambers were washed with 1 mL of PBS and then blocked with 1 mg/mL β-casein (Thermo Fisher Scientific 37528) for 10 min. The chambers were then rinsed with 1 mL PBS buffer. H-Ras was incubated at 0.1~1 mg/mL for 2 hr 30 min in PBS buffer at room temperature. The chambers were then washed with 1 mL PBS, and 5 mM BME was subsequently added to quench the reaction. After 10 min, the flow channel was washed with 1 mL of PBS, and buffer exchanged into reaction buffer (40 mM HEPES (pH 7.4), 100 mM NaCl, 5 mM $MgCl_2$) plus 100 μM GDP. 10~200 nM LAT and 12.5 nM Hck are introduced into the flow channel and incubated for 40 min. After washing with 1 mL reaction buffer, the flow channels were incubated with 1 mM ATP and 100 μM GDP to phosphorylate LAT and ensure nucleotide loading in Ras. ATP and GDP was washed away with reaction buffer plus 10 mM BME and used immediately for reaction. All Ras reactions were performed in a buffer containing 40 mM HEPES (pH 7.4), 100 mM NaCl, 5 mM $MgCl_2$, 10 mM BME, 100 μM GTP, 2 mM UV-treated Trolox, with the addition of 20 nM Alexa647-RBD(K65E) to monitor the reaction. For SOS and SOS^{CatPR} reactions, 20nM Grb2 were included as well. In competition reaction with p120GAP, 200 nM p120GAP was used.

Microscope hardware and imaging acquisition

TIRF imaging experiments were performed on an inverted Nikon Eclipse Ti microscope using either a 100x Nikon objective (1.49 NA) oil immersion TIRF objective or a 60x Apo TIRF oil immersion objective (1.45 NA). The light sources were either a 488 nm, 561 nm, or 637 nm diode laser (OBIS laser diode, Coherent, Santa Clara, CA) controlled with a custom built Solemere (Salt Lake City, Utah) laser driver with analog and digital modulation (0-5 volts). Images were acquired on an EMCCD camera (Andor Technology Ltd., UK). All microscope hardware was controlled using Micro-Manager v4.0(*174*). Samples were excited with 0.3~0.8 mW laser power at the objective. The exposure time is typically 100~300 ms. In end point assays, imaging starts after 2hrs of incubation to avoid photobleaching.

Surface Density Measurements

Surface density of Ras and LAT were measured using fluorescence correlation spectroscopy (FCS) on a homebuilt setup based on a Nikon Eclipse TE2000-E inverted microscope. A pulsed white light laser source (SuperK Extreme EXW-12, NKT Photonics) was filtered by bandpass filters for desired excitation wavelengths and combined through a single-mode optical fiber. The excitation pulses enter the microscope via a multicolour dichroic cube (Di01-R405/488/561/635-25x36, Semrock). The fluorescence signal is collected by a ×100 high-numerical aperture oil-immersion objective, recorded by avalanche photodiode detectors (Hamamatsu), and directly converted into autocorrelation signal by a hardware correlator (Correlator.com). The resulting autocorrelation G(t) was fit to the two-dimensional Gaussian diffusion model to calculate surface density. Surface density calibration was achieved by fitting the FCS surface density measurement to TIRF intensity plot to a linear regression. LAT densities were measured by directly labeling LAT with Alexa-555 dye. Ras densities were measured by loading Ras with Atto-488-GDP (Jena Biosceince) using SOS^{Cat}.

Stochastic Simulation

The time evolution of all species in the reaction was simulated stochastically using the Gillespie algorithm in MATLAB, following the kinetic scheme in Figure 5A. Two assumptions were made: 1) The membrane compositions are spatially homogeneous within reaction space due diffusion. 2) the solution concentration

of SOS_{sol}, $\rho_{SOS_{sol}}$,is constant since there is a large solution reservoir in the experiment. Each molecular species is expressed as the exact number of molecules. The rate for each transition is calculated as:

$SOS_{sol} \rightarrow SOS{:}RasGDP; \quad r_1 = k_{on}^{(1)} \cdot \rho_{SOS_{sol}} \cdot \sigma_{RasGDP} \cdot A.$

$SOS_{sol} \rightarrow SOS{:}RasGTP; \quad r_2 = k_{on}^{(2)} \cdot \rho_{SOS_{sol}} \cdot \sigma_{RasGTP} \cdot A.$

$SOS{:}RasGDP \rightarrow SOS_{sol}; \quad r_3 = k_{off}^{(1)} \cdot \sigma_{SOS:RasGDP} \cdot A.$

$SOS{:}RasGTP \rightarrow SOS_{sol}; \quad r_4 = k_{off}^{(2)} \cdot \sigma_{SOS:RasGTP} \cdot A.$

$RasGDP \rightarrow RasGTP \; ; \quad r_5 = k_{cat}^{(1)} \cdot (\sigma_{SOS:RasGDP} + \sigma_{SOS:RasGTP}) \cdot \sigma_{RasGDP} \cdot A.$

$RasGTP \rightarrow RasGDP \; ; \quad r_6 = k_{cat}^{(2)} \cdot \sigma_{RasGTP} \cdot A.$

A is the area of the membrane in μm^2, and the surface density of each membrane associated species, σ_x, is expressed as discrete molecular copy number per unit area. We used the following rate parameters:

$k_{on}^{(1)} \cdot \rho_{SOS_{sol}} = 0.0000007\ t^{-1}$ (ρ_{E0} taken as constant for infinite solution reservoir.)

$k_{on}^{(2)} \cdot \rho_{SOS_{sol}} = 1 \times k_{on}^{(1)} \cdot \rho_{SOS_{sol}}$ (ρ_{E0} taken as constant for infinite solution reservoir.)

$k_{off}^{(1)} = 0.005\ t^{-1}$

$k_{off}^{(2)} = 0.001\ t^{-1}$

$k_{cat}^{(1)} = 0.01\ \mu m^2 t^{-1}$

$k_{cat}^{(2)} = 0.005\ t^{-1}$

The kinetic parameters used reflect reported kinetic rate constants(*39*, *49*, *115*). All simulations begin with 1000/μm^2 RasGDP. Statistics were collected from 500 simulations. In concentration titration simulations, $k_{on}^{(1)} \cdot \rho_{SOS_{sol}}$ varies from $0.0000003 \sim 0.00003\ t^{-1}$.

For simulations with non-processive SOS, we used the following rate parameters:

$k_{on}^{(1)} \cdot \rho_{SOS_{sol}} = 0.00003 \sim 0.0003\ t^{-1}$

$k_{on}^{(2)} \cdot \rho_{SOS_{sol}} = 1 \times k_{on}^{(1)} \cdot \rho_{SOS_{sol}}$

$k_{off}^{(1)} = 0.5\ t^{-1}$

$k_{off}^{(2)} = 0.1\ t^{-1}$

$k_{cat}^{(1)} = 0.01\ \mu m^2 t^{-1}$

$k_{cat}^{(2)} = 0.005\ t^{-1}$

For the simulations of Fig 5E and 5F, we modified the simulation parameters to facilitate comparison. Specifically, we used an adjusted $k_{on}^{(1)} \cdot \rho_{SOS_{sol}}$ that leads to 0.5 RasGTP/Ras steady state response in deterministic kinetics. We also make the positive feedback strictly from the difference in $k_{on}^{(1)}$ and $k_{on}^{(2)}$, and leaving $k_{off}^{(1)}$ and $k_{off}^{(2)}$ the same to eliminate the dependence of processivity on changes in feedback strength.

For Fig 5E, rates used are:

$k_{on}^{(1)} \cdot \rho_{SOS_{sol}} = 9.91100916786229 \times 10^{-7}\ t^{-1}$

$k_{on}^{(2)} \cdot \rho_{SOS_{sol}} = 1 \times k_{on}^{(1)} \cdot \rho_{SOS_{sol}}$

$k_{off}^{(1)} = 0.1\ t^{-1}$

$k_{off}^{(2)} = 0.1\ t^{-1}$

$k_{cat}^{(1)} = 0.01\ \mu m^2 t^{-1}$

$k_{cat}^{(2)} = 0.005\ t^{-1}$

For Fig 5F, rates used are:

$k_{on}^{(1)} \cdot \rho_{SOS_{sol}} = 4.69366456778945\text{e} - 05\ t^{-1}$

$k_{on}^{(2)} \cdot \rho_{SOS_{sol}} = 1 \times k_{on}^{(1)} \cdot \rho_{SOS_{sol}}$

$k_{off}^{(1)} = 0.125\ t^{-1}$

$k_{off}^{(2)} = 0.125\ t^{-1}$

$k_{cat}^{(1)} = 1\ \mu m^2 t^{-1}$

$k_{cat}^{(2)} = 0.25\ t^{-1}$

For the simulation in Figure S4A with no inhibitor, we used the following rate parameters:

$k_{on}^{(1)} \cdot \rho_{SOS_{sol}} = 2.51927828981377 \times 10^{-6}\ t^{-1}$

$k_{on}^{(2)} \cdot \rho_{SOS_{sol}} = 100 \times k_{on}^{(1)} \cdot \rho_{SOS_{sol}}$

$k_{off}^{(1)} = 0.1\ t^{-1}$

$k_{off}^{(2)} = 0.1\ t^{-1}$

$k_{cat}^{(1)} = 0.01\ \mu m^2 t^{-1}$

$k_{cat}^{(2)} = 0.005\ t^{-1}$

For the simulation in Figure S4B with no inhibitor, we used the following rate parameters:

$k_{on}^{(1)} \cdot \rho_{SOS_{sol}} = 2.02450061053583 \times 10^{-6}\ t^{-1}$

$k_{on}^{(2)} \cdot \rho_{SOS_{sol}} = 1 \times k_{on}^{(1)} \cdot \rho_{SOS_{sol}}$

$k_{off}^{(1)} = 0.001\ t^{-1}$

$k_{off}^{(2)} = 0.001\ t^{-1}$

$k_{cat}^{(1)} = 0.01\ \mu m^2 t^{-1}$

$k_{cat}^{(2)} = 0.005\ t^{-1}$

For simulation of Ras activation-deactivation reaction with SOS inhibitor, the following transitions are simulated:

$SOS_{sol} \rightarrow SOS{:}RasGDP; \quad r_1 = k_{on}^{(1)} \cdot \rho_{SOS_{sol}} \cdot \sigma_{RasGDP} \cdot A.$

$SOS_{sol} \rightarrow SOS{:}RasGTP; \quad r_2 = k_{on}^{(2)} \cdot \rho_{SOS_{sol}} \cdot \sigma_{RasGTP} \cdot A.$

$SOS_{sol}^{i} \rightarrow SOS^{i}{:}RasGDP; \quad r_3 = k_{on}^{(1)} \cdot \rho_{SOS_{sol}^{i}} \cdot \sigma_{RasGDP} \cdot A.$

$SOS_{sol}^{i} \rightarrow SOS^{i}{:}RasGTP; \quad r_4 = k_{on}^{(2)} \cdot \rho_{SOS_{sol}^{i}} \cdot \sigma_{RasGTP} \cdot A.$

$SOS{:}RasGDP \rightarrow SOS_{sol}; \quad r_5 = k_{off}^{(1)} \cdot \sigma_{SOS:RasGDP} \cdot A.$

$SOS{:}RasGTP \rightarrow SOS_{sol}; \quad r_6 = k_{off}^{(2)} \cdot \sigma_{SOS:RasGTP} \cdot A.$

$SOS^{i}{:}RasGDP \rightarrow SOS_{sol}^{i}; \quad r_7 = k_{off}^{(1)} \cdot \sigma_{SOS^{i}:RasGDP} \cdot A.$

$SOS^{i}{:}RasGTP \rightarrow SOS_{sol}^{i}; \quad r_8 = k_{off}^{(2)} \cdot \sigma_{SOS^{i}:RasGTP} \cdot A.$

$SOS{:}RasGDP \rightarrow SOS^{i}{:}RasGDP; \quad r_9 = k_{on}^{i} \cdot \rho_{inhibitor} \cdot \sigma_{SOS:RasGDP} \cdot A.$

$SOS{:}RasGTP \rightarrow SOS^{i}{:}RasGTP; \quad r_{10} = k_{on}^{i} \cdot \rho_{inhibitor} \cdot \sigma_{SOS:RasGTP} \cdot A.$

$SOS^i : RasGDP \rightarrow SOS{:}RasGDP; \quad r_{11} = k_{off}^i \cdot \sigma_{SOS^i :RasGDP} \cdot A.$

$SOS^i : RasGTP \rightarrow SOS{:}RasGTP; \quad r_{12} = k_{off}^i \cdot \sigma_{SOS^i :RasGTP} \cdot A.$

$RasGDP \rightarrow RasGTP \;\; ; \quad r_{13} = k_{cat}^{(1)} \cdot (\sigma_{SOS:RasGDP} + \sigma_{SOS:RasGTP}) \cdot \sigma_{RasGDP} \cdot A.$

$RasGTP \rightarrow RasGDP \;\; ; \quad r_{14} = k_{cat}^{(2)} \cdot \sigma_{RasGTP} \cdot A.$

SOS species with superscript "i" are bound to the inhibitor and are catalytically inactive. The solution concentration of the inhibitor, $\rho_{inhibitor}$, and the solution concentration of SOS_{sol}^i, $\rho_{SOS_{sol}^i}$, are constant. This is assuming the inhibitor binding has reached equilibrium in the large solution reservoir. For the simulation in Figure S4A with no inhibitor, we used the following parameters:

$k_{on}^i \cdot \rho_{inhibitor} = 0.0001 \sim 0.0009\ t^{-1}$

$k_{off}^i = 0.0001\ t^{-1}$

$k_{on}^{(1)} \cdot \rho_{SOS_{sol}} = \frac{k_{off}^i}{k_{on}^i \cdot \rho_{inhibitor} + k_{off}^i} \cdot 2.51927828981377 \times 10^{-6}\ t^{-1}$

$k_{on}^{(2)} \cdot \rho_{SOS_{sol}} = 100 \times k_{on}^{(1)} \cdot \rho_{SOS_{sol}}$

$k_{on}^{(1)} \cdot \rho_{SOS_{sol}^i} = \frac{k_{on}^i \cdot \rho_{inhibitor}}{k_{on}^i \cdot \rho_{inhibitor} + k_{off}^i} \cdot 2.51927828981377 \times 10^{-6}\ t^{-1}$

$k_{on}^{(2)} \cdot \rho_{SOS_{sol}^i} = 100 \times k_{on}^{(1)} \cdot \rho_{SOS_{sol}^i}$

$k_{off}^{(1)} = 0.1\ t^{-1}$

$k_{off}^{(2)} = 0.1\ t^{-1}$

$k_{cat}^{(1)} = 0.01\ \mu m^2 t^{-1}$

$k_{cat}^{(2)} = 0.005\ t^{-1}$

Deterministic Steady State Solution

The deterministic steady state solution is obtained by solving the following equations using MATLAB.

$$\frac{dSOS{:}RasGDP}{dt} = k_{on}^{(1)} \cdot \rho_{\rho_{SOS_{sol}}} \cdot \sigma_{RasGDP} - k_{off}^{(1)} \cdot \sigma_{SOS:RasGDP} = 0$$

$$\frac{dSOS{:}RasGTP}{dt} = k_{on}^{(2)} \cdot \rho_{\rho_{SOS_{sol}}} \cdot \sigma_{RasGTP} - k_{off}^{(1)} \cdot \sigma_{SOS:RasGTP} = 0$$

$$\frac{dRasGDP}{dt} = k_{cat}^{(2)} \cdot \sigma_{RasGTP} - k_{cat}^{(1)} \cdot (\sigma_{SOS:RasGDP} + \sigma_{SOS:RasGTP}) \cdot \sigma_{RasGDP} - k_{on}^{(1)} \cdot \rho_{\rho_{SOS_{sol}}} \cdot \sigma_{RasGDP} + k_{off}^{(1)} \cdot \sigma_{SOS:RasGDP} = 0$$

$$\frac{dRasGTP}{dt} = k_{cat}^{(1)} \cdot (\sigma_{SOS:RasGDP} + \sigma_{SOS:RasGTP}) \cdot \sigma_{RasGDP} - k_{cat}^{(2)} \cdot \sigma_{RasGTP} - k_{on}^{(2)} \cdot \rho_{SOS_{sol}} \cdot \sigma_{RasGTP} + k_{off}^{(2)} \cdot \sigma_{SOS:RasGTP} = 0$$

$$RasGDP + RasGTP + SOS:RasGDP + SOS:RasGTP = total\ Ras = 1000$$

For figure S3-5, the equations are modified to:

$$\frac{dSOS:RasGDP}{dt} = k_{on}^{(1)} \cdot \rho_{\rho_{SOS_{sol}}} \cdot \sigma_{RasGDP} - k_{off}^{(1)} \cdot \sigma_{SOS:RasGDP} = 0$$

$$\frac{dSOS:RasGTP}{dt} = k_{on}^{(2)} \cdot \rho_{\rho_{SOS_{sol}}} \cdot \sigma_{RasGTP} - k_{off}^{(1)} \cdot \sigma_{SOS:RasGTP} = 0$$

$$\frac{dRasGDP}{dt} = \frac{k_{cat}^{(2)} \cdot \sigma_{RasGTP}}{K_M GAP + \sigma_{RasGTP}} - \frac{k_{cat}^{(1)} \cdot (\sigma_{SOS:RasGDP} + \sigma_{SOS:RasGTP}) \cdot \sigma_{RasGDP}}{K_M SOS + \sigma_{RasGDP}} - k_{on}^{(1)} \cdot \rho_{\rho_{SOS_{sol}}} \cdot \sigma_{RasGDP} + k_{off}^{(1)} \cdot \sigma_{SOS:RasGDP} = 0$$

$$\frac{dRasGTP}{dt} = \frac{k_{cat}^{(1)} \cdot (\sigma_{SOS:RasGDP} + \sigma_{SOS:RasGTP}) \cdot \sigma_{RasGDP}}{K_M SOS + \sigma_{RasGDP}} - \frac{k_{cat}^{(2)} \cdot \sigma_{RasGTP}}{K_M GAP + \sigma_{RasGTP}} - k_{on}^{(2)} \cdot \rho_{SOS_{sol}} \cdot \sigma_{RasGTP} + k_{off}^{(2)} \cdot \sigma_{SOS:RasGTP} = 0$$

$$RasGDP + RasGTP + SOS:RasGDP + SOS:RasGTP = total\ Ras = 1000$$

$$k_{on}^{(1)} \cdot \rho_{SOS_{sol}} = 0.00015 \sim 0.015\ t^{-1}$$

$$k_{on}^{(2)} \cdot \rho_{SOS_{sol}} = 1 \times k_{on}^{(1)} \cdot \rho_{SOS_{sol}}$$

$$k_{off}^{(1)} = 3\ t^{-1}$$

$$k_{off}^{(2)} = 0.4\ t^{-1}$$

$$k_{cat}^{(1)} = 0.03\ t^{-1}$$

$$K_M SOS = \frac{k_{cat}^{(1)} + 1}{0.05}\ \mu m^{-2}$$

$$k_{cat}^{(2)} = 0.1\ t^{-1}$$

$$K_M GAP = \frac{k_{cat}^{(2)} + 0.2}{1.74}\ \mu m^{-2}$$

APPENDIX C

Material and Methods for Chapter 4

Protein Purification

OCRL, DrrA-OCRL, and PIP5K

OCRL (residues 234-539), DrrA-OCRL and PIP5K (residues 1-421) were purified as previously described(*6*).

Alexa488-PLCδ_{PH} and Cy3-DrrA

PLCδ PH domain (11-140aa) and DrrA (residues 544-647) were purified and labeled with fluorophores as previously described(*6*).

Alexa555-LAT and Grb2

Wildtype human LAT (cytosolic domain, residues 30-233) and Grb2 (full length) were purified following previously described protocols(*171*), using N-terminal 10- and 6- His tag for the LAT and Grb2, respectively. LAT was labeled by reacting with Alexa555-maleimide (Invitrogen) at 1:10 molar ratio at room temperature for 2 hours and subsequently quenched by adding 10 mM 2-mercaptoethanol. The labeled LAT was then purified by size exclusion chromatography (Superdex S75 10/300 GL, Cytiva). The His-tag attached to Grb2 was removed by Tobacco Etch Virus (TEV) protease.

SOS

Full-length SOS protein was purified as previously described(*44*).

Ras and p120GAP

H-Ras (residues 1-181, C118S) and the GAP domain of p120GAP (714-1047) was purified following a previously described protocol(*74*, *164*), using the N-terminal 6-His tag. Then the His-tag was removed by TEV protease.

Alexa647-RBD

The Ras-binding domain (RBD, residues 56-131, K65E) of Raf1 was purified and labeled with Alexa Fluor 647 maleimide dye as previously described(*44*).

Pig leukocyte lysate

The pig leukocyte lysate was prepared as described previously(*175*). The lysate was snap-frozen using liquid nitrogen and kept at -80℃ for storage. To increase the strength of the reaction, the lysate was 4x concentrated by spinning it down through a centrifugal filter (Amicon Ultra-4, 3 kDa MWCO, Merck Millipore) at 5,000 g using for 2 hours before the experiment.

Microfabrication of chromium patterns on glass coverslips

A quartz/chromium photomask was designed using AutoCAD (Autodesk) and ordered through Front Range PhotoMask (Lake Havasu City, AZ). Photolithography was performed in the Biomolecular Nanotechnology Center at the University of California at Berkeley (QB3, California Institute of Quantitative Biosciences). Coverslips were first sonicated in acetone and rinsed extensively with Milli-Q water. The coverslips were then placed on hot plates at 120℃ for 5 minutes to vaporize any residual solvent. After coverslips were cooled down, the following procedure was applied for each coverslip: a coverslip was mounted on a spin coater (Laurell Tech. Co.), and the coverslip was covered with S1805 positive photoresist (MicroChem, 10018321) and spun at 500 rpm for 5 seconds (accelerated by 100 rpm/s for 5 seconds), and 4000 rpm for 30.7 seconds (accelerated by 12000 rpm/s for about 0.3 seconds). Then the accumulated photoresist at the edge of the coverslip (edge bead) was removed by an acetone-applied cotton swab (this step enhances the contact with the photomask later). Then the coverslip was baked at 115℃ for 1 minute (soft bake). After cool-down, the ordered photomask was mounted on an OAI 200 Aligner and brought the coverslip to hard contact, photoresist-side up to expose the coverslip with 30 mW/cm^2 UV light for 0.6 seconds through the mask. The minimum amount of exposure time required for correct development was used to achieve high spatial resolution. Next, the coverslip was developed in MicroPosit MF-319 Liquid Developer (MicroChem, 10018042) with mild shaking, such that the UV-exposed part dissolved away, resulting in a patterned photoresist. Then the coverslip was rinsed with water and dried with N_2 gas. Next, using 10^{-6} torr e-beam evaporation, 9 nm of chromium was deposited on the top of the patterned photoresist. Then the photoresist was lifted by sonicating coverslip in MicroPosit Remover 1165 for 10 minutes. The resulting coverslips had chromium left where there was no photoresist underneath. Finally, the coverslips were rinsed extensively with water and placed in a dust-free slide box until usage.

Small Unilamellar Vesicles (SUV) Preparation

Two different lipid compositions were used. For the PIP polarization experiments, 1,2-dioleoyl-sn-glycero-3-phosphocholine (18:1 DOPC, Avanti 850375), L-α-phosphatidylinositol-4-phosphate (brain PI(4)P, Avanti 840045), and L-α-phosphatidylinositol-4,5-bisphosphate (brain PI(4,5)P_2, Avanti 840046) in chloroform were used. The lipids were dispensed into a 35 mL round bottom glass flask in a 96:2:2 molar percent ratio, such that the resulting lipid concentration became 2 μmol.

For the Ras polarization experiments, DOPC (Avanti 850375), 1,2-dioleoyl-sn-glycero-3-[(N-(5-amino-1-carboxypentyl)iminodiacetic acid)succinyl] (nickel salt) (18:1 DGS-NTA(Ni), Avanti 790404), 1,2-dioleoyl-sn-glycero-3-phosphoethanolamine-N-[4-(p-maleimidomethyl)cyclohexane-carboxamide] (sodium salt) (18:1 PE MCC, Avanti 780201), and PI(4,5)P2 (Avanti 840046) in chloroform were used. The lipids were dispensed into a 35 mL round bottom glass flask in 92:4:2:2 molar percent ratio, such that the resulting lipid concentration became 2 μmol.

The mixed lipids were dried using a rotary evaporator to a thin film at 37 °C for 2 minutes, then at room temperature for 13 minutes. The dried film was further blown with nitrogen gas for 15 minutes and then resuspended in 2 mL Milli-Q water by pipetting to make 1 mM lipid in water. For making SUVs, the mixture was sonicated using a tip sonicator (Analis Scientific Instruments) for 4 minutes 20 seconds, repeating 20 seconds sonication and 20 seconds rest, while the lipid-containing tube was immersed in ice water to prevent heating up. The lipid water mixture became clear. The resulting SUV was used within two days and was kept at 4℃ until use.

Supported Lipid Bilayer (SLB) Preparation

SLBs were formed on glass coverslips (25mm x 75mm, Ibidi 10812, micropatterned with chromium or not). The coverslips were sonicated for 10 minutes, rinsed in Milli-Q water, and then etched in piranha solution (hydrogen peroxide and sulfuric acid mixed with 1:3 ratio) for 5 minutes. After etching, the coverslips were immersed in Milli-Q water to preserve the hydrophilicity and used within two days. The flow chambers were made by first drying the coverslips with nitrogen gas and then attaching them to the sticky-side of six-well flow chamber covers (Ibidi 80608). For SLB formation, 1 mM SUVs were diluted to 0.25 mM using PBS (pH 7.2) and dispensed 125 μL into each channel in the chamber. The SUV was introduced quickly enough following the chamber assembly to minimize the decay of hydrophilicity of the glass surface. After 30 minutes, each channel was washed with 3 mL of PBS and blocked with 1 mg/mL β-casein (Thermo Fisher Scientific 37528, 0.22 μm syringe filtered) for 10 minutes. Then the channels were washed with 1 mL of PBS. For PIP polarization experiments, this marked the end of preparation.

For Ras polarization experiments, the following steps were further taken: 0.5 mg/mL H-Ras in PBS was incubated for 2 hours and 30 minutes for its attachment to the PE-MCC via maleimide reaction. Then the channels were incubated with 5 mM 2-Mercaptoethanol (BME) for 10 minutes to quench the reaction. Next, 40 nM LAT and 12.5 nM Hck were incubated for 40 minutes to attach to DGS-NTA(Ni). Then, 1 mM ATP and 100 μM GDP were added in Ras reaction buffer for 40 minutes for LAT phosphorylation by Hck, GDP loading of Ras, and desorption of unstably bound proteins from the membrane. Then, 100 μM GDP in Ras reaction buffer was added and kept in the channels, in which GDP was washed away only immediately before the reaction using Ras reaction buffer. Between all incubation steps, the channels were washed with 1 mL PBS.

Microscopy

For TIRF imaging, an inverted Nikon Eclipse Ti-E microscope with Plan Apo TIRF 60x 1.45 N.A. oil immersion objective (Nikon) was used. 488 nm and 561 nm diode laser (OBIS laser diode, Coherent, Santa Clara, CA) were used as excitation light sources, driven by a custom-built Solemere laser driver (Salt Lake City, Utah). The laser powers were 0.2 - 1.0 mW at the objective. Exposure times were typically 50 ms to 200 ms. We used ZT405/488/561/647rpc dichroic filter cubes (Chroma Technology Corp, Bellows Falls, VT) to filter excitation light and ET525/50M, ET600/50M emission filters (Semrock) to filter emission light. An EMCCD camera (iXon Ultra, Andor Technology Ltd., UK) was used for image acquisition. The stage was controlled with a motorized stage and joystick (ASI MS-2000, Eugene, OR), and the Nikon Perfect Focus System (PFS) was used. Micro-Manager v4.0(*169*) was used to control all hardware. Images were taken every 5 seconds, with 50 – 200 ms exposure.

Reaction imaging

For the PIP polarization experiment using purified phosphatase and kinase, the following reaction buffer was used: 20 mM HEPES (pH 7), 150 nM NaCl, 1 mM ATP, 5 mM $MgCl_2$, 0.5 mM EGTA, 200 μg/mL β-casein, 20 mM BME, 20 mM glucose, 20 nM Cy3-DrrA (PI4P sensor), and 20 nM Alexa488-PLCδPH ($PI(4,5)P_2$ sensor).

For the cell lysate experiment the buffer consisted of 10 mM HEPES (pH 7), 75 nM NaCl, 1 mM ATP, 2.5 mM $MgCl_2$, 0.25 mM EGTA, 100 μg/mL β-casein, 10 mM BME, 10 mM glucose, 20 nM Cy3-DrrA (PI4P sensor), and 20 nM Alexa488-PLCδPH ($PI(4,5)P_2$ sensor).

For the Ras polarization experiment the buffer consisted of 40 mM HEPES (pH 7.4), 100 mM NaCl, 5 mM $MgCl_2$, 10 mM 2-Mercaptoethanol (BME), 20 μg/mL β-casein, 2 mM UV-trated Trolox, 20 nM Grb2, 20 nM Alexa647-RBD, and 100 μM GTP.

Simulations

NetLogo (Wilensky, U. 1999. NetLogo.) was used to simulate two-dimensional reaction-diffusion kinetics. For the PIP reactions, the reaction space was subdivided into small patches (0.36 μm^2, unless stated otherwise), and within each patch, the lipid composition was approximated as homogeneous. Accordingly, a single reaction coordinate value, x, was assigned to each patch. Because the number of PIP lipids per unit area is substantial (~56000 per μm^2) in the experiment, lipid conversions and lipid dispersion were adequately modeled as deterministic processes. In contrast, because the number of enzymes binding to the membrane is 3 to 4 orders of magnitude lower (initially, 1 – 10 per μm^2)(*6*), enzyme binding, unbinding, and diffusion (random walk) on the membrane were modeled as stochastic processes. The solution above the membrane was modeled as a homogeneous reservoir of enzymes because the solution had 3 to 4 orders of magnitude more enzymes than the membrane and did not transmit a correlation or anti-correlation between membrane parts. Thus, phosphatase without membrane binding (i.e., solution phosphatase) was modeled as constant lipid converting pressure over the entire membrane following Michaelis-Menten kinetics. In contrast, membrane-binding enzymes were modeled with constant enzyme-binding rates per enzyme-recruiting lipid.

More specifically, the conversion of PIP lipids per patch by solution phosphatase was modeled as

$$\frac{dx}{dt} = -k^-_{cat,sol} \cdot \frac{x}{\widehat{K^-_M}+x},$$

and the conversion by membrane-bound kinase and phosphatase was modeled as

$$\frac{dx}{dt} = k^+_{cat} \cdot \sigma_K \cdot \frac{1-x}{\widehat{K^+_M}+1-x}, \text{ and } \frac{dx}{dt} = -k^-_{cat,mem} \cdot \sigma_P \cdot \frac{x}{\widehat{K^-_M}+x},$$

where $k^-_{cat,sol}$, k^+_{cat}, and $k^-_{cat,mem}$ are the catalytic rate of solution phosphatase, membrane-binding kinase, and membrane-binding phosphatase. $\widehat{K^-_M}$ and $\widehat{K^+_M}$ are the Michaelis constants of the phosphatase and kinase (normalized to the reaction coordinate x), whereas σ_K is the surface density of the membrane-bound kinase and σ_P is the surface density of the membrane-bound phosphatase. x is the reaction coordinate, defined as $\sigma_{PI4P} / (\sigma_{PI4P} + \sigma_{PI(4,5)P_2})$. At t_0, all simulations had $x = 0.5$ and no enzyme on the membrane as the initial condition.

We used the following parameters for the simulation:

$\widehat{k^+_{on}} = 0.1,$

$k^+_{off} = 0.7,$

$k^+_{cat} = 10,$

$\widehat{K_M^+} = 2$,

$\widehat{k_{on}^-} = 0.02$,

$k_{off}^- = 0.1$,

$k_{cat,sol}^- = 0.15$,

$k_{cat,mem}^- = 15$, and

$\widehat{K_M^-} = 0.5$.

Note, $\widehat{k_{on}^{\pm}}$, and $\widehat{K_M^{\pm}}$ have units that are normalized to the reaction coordinate x and thus are different from the usual definition of the kinetic on-rate and the Michaelis constant.

The diffusion coefficients of enzymes and PIP lipids were set as

$D_{enz} = 0.2\ \mu m^2/s$, and

$D_{pip} = 2\ \mu m^2/s$.

For the PIP lipid dispersion, x value of each patch was updated after each timestep as follows:

$$x_{t+\Delta t} = \left(1 - \left(4\alpha\frac{n}{4}\right)\right)x_t + \alpha\sum_{neighboring\ patches} x_t,$$

where $\alpha = \frac{D_{pip}\Delta t}{\Delta L^2}$ and n is the number of neighboring patches (max 4).

For modeling each enzyme diffusion on the membrane, a random walk on a two-dimensional lattice was simulated. Because only the tracking of which patch an enzyme is on was needed, the hopping distance was set identical to the patch length (ΔL). Then, to model the enzyme diffusion on the membrane, an enzyme either hopped to a neighboring patch or stayed in the present patch, following the probabilities:

$$P_{hop} = \frac{n}{4}\cdot\frac{4D_{enz}}{\Delta L^2}\Delta t,$$

$$P_{stay} = 1 - P_{hop}.$$

The time step was set as 0.01s unless stated otherwise. Von Neumann stability analysis ($\Delta t \leq \frac{\Delta L^2}{4D_{pip}}$) was always performed before the simulation to ensure the numerical stability of the forward time centered space (FTCS) scheme.